Ph.D. DISSERTATION

Manipulating Spatiotemporal Degrees of Freedom for Photonic Switching Devices:
Theoretical and Machine-learning Approaches

광스위칭 소자 설계를 위한 시공간 자유도의 조작

BY

JUNGMIN KIM

FEBRUARY 2023

DEPARTMENT OF ELECTRICAL AND COMPUTER
ENGINEERING
COLLEGE OF ENGINEERING
SEOUL NATIONAL UNIVERSITY

Ph.D. DISSERTATION

Manipulating Spatiotemporal Degrees of Freedom for Photonic Switching Devices:
Theoretical and Machine-learning Approaches

광스위칭 소자 설계를 위한 시공간 자유도의 조작

BY

JUNGMIN KIM

FEBRUARY 2023

DEPARTMENT OF ELECTRICAL AND COMPUTER
ENGINEERING
COLLEGE OF ENGINEERING
SEOUL NATIONAL UNIVERSITY

Manipulating Spatiotemporal Degrees of Freedom for Photonic Switching Devices:
Theoretical and Machine-learning Approaches

광스위칭 소자 설계를 위한 시공간 자유도의 조작

지도교수 박 남 규

이 논문을 공학박사 학위논문으로 제출함

2023년 2월

서울대학교 대학원

전기·정보공학부

김 정 민

김정민의 공학박사 학위 논문을 인준함

2023년 2월

위 원 장:	정 윤 찬	(인)
부위원장:	박 남 규	(인)
위 원:	김 기 홍	(인)
위 원:	민 범 기	(인)
위 원:	유 선 규	(인)

Abstract

Photonic switching devices are the most basic and essential unit for implementing optical memory and processor, which provide tunable optical responses according to external modulations in analogy with electronic transistors operated by the modulation of gate voltage. When designing such elements, both the spatial and temporal complexities are involved in the operation of photonic switching. For example, one should consider spatial characteristics of light, such as spin and orbital angular momenta and wave vector, as well as time-domain ones such as operating frequency, bandwidth, and the conservation of energy, in terms of the corresponding material and structural properties. In this point of view, the inherent large amount of degrees of freedom arising from the functional multiplicity in photonic active switching devices should be fully considered, while access to them is often blocked by the physical symmetries residing in the structure of devices. Despite the tradeoff between the number of degrees of freedom and the difficulties in terms of theoretical and computational cost, therefore, the necessity of symmetry breaking has been on the rise in recent studies, resolving the complexity with efficient theoretical and data-driven treatments.

Here, I introduce several related topics on numerical, theoretical, and data-driven methods in omnibus format for resolving spatiotemporal complexities in photonic switching or active devices, in terms of C_{4v}-symmetry in photonic crystals and spatiotemporal translational symmetries in photonic disorders. These approaches will pave the way to the photonic design with extremely high complexities and be toolkits for optical computers.

keywords: Photonics, Switching devices, Disorder, Symmetry, Inverse design, Deep learning

student number: 2017-28066

Contents

List of Tables

List of Figures

Chapter 1

Introduction

1.1 Motivation

While light itself is one of the most important objects in physical science, both as an electromagnetic wave and an elementary particle, its new role as an information and energy carrier has drawn a lot of attention with the emergence of optical computing in the fields of optical engineering and photonics [10, 11]. Compared to conventional modern computers that utilize electrons as counterpart carriers, photons are bosonic particles, which in principle do not interact with each other. Also well-known with light speed c, these fundamental characteristics give rise to great advantages of optical computing over electronic computing, in terms of low power consumption due to the zero crosstalk and ultrafast computing speed.

Similar to transistors being the basic element of computers, which is an electronic on/off switch operated by the modulation of gate voltage, optical computing also requires such basic elements that provide different optical responses according to the external modulations. In this regard, the design of efficient optical switching devices in terms of energy and functionality holds great importance, which will significantly determine the overall performance of the optical computer. However, those requirements for high functionalities and active tunability, at the same time, become a huge
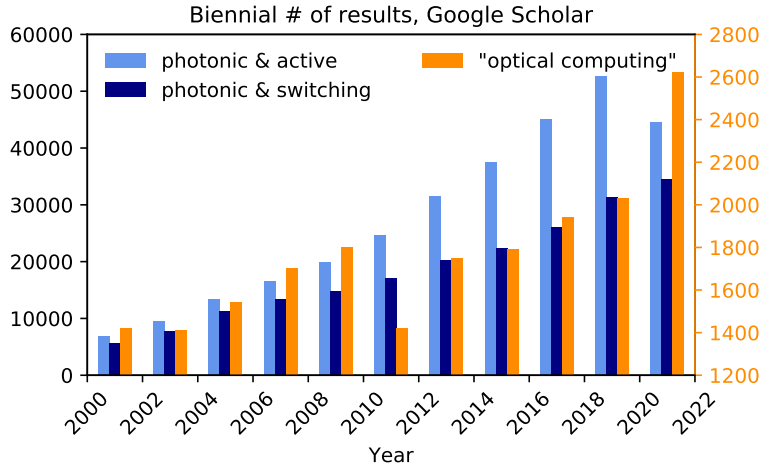
Figure 1.1: The two-year numbers of search results (Google Scholar) for keywords: photonic AND active (light blue), photonic AND switching (navy), and "optical computing" (orange, right y-axis)

obstacle in the design process. That is, the functionality is usually in relation to the spatial distribution of optical energy flows or distributions, such as focusing, scattering, and mode coupling, while the active tunability is described by time-varying energy exchange between a system and its environment. Considering the vast amount of degree of freedom in multiple axes is the main problem in designing optical structures, especially active and high-functionality devices. As shown in Fig. 1.1, the design problem concerning photonic active switching devices is one of the fast-growing topics towards the implementation of ideal optical computers in recent physics and engineering communities.

The main approach to resolving such multi-degree-of-freedom issues is to exploit symmetry breaking: such as spatial parity, mirror, and translational symmetries; and time reversal and translational symmetries. Symmetry makes the world easy and simple, and is also connected to fundamental conservation laws of related physical quantities; when it comes to engineering or design, however, symmetries often become a constraint

that reduces the possible output of a system.

As a very rough example, an all-optical memory device can be implemented on the platform of nonlinear coupled resonators [12] with a certain symmetry breaking. Utilizing its oscillation quenching states as memory on/off states, it is essential to secure two quite conflicting standards: being robust against error and sensitive to modulation signal simultaneously. In this case, a serial coupling of three resonators with saturable gain, neutral, and absorption, in which both the parity ($\mathcal{P}$) and the time-reversal ($\mathcal{T}$) symmetries are broken, becomes the origin of topological properties: $\mathcal{PT}$-broken and -unbroken phases, enabling the topological protection against error, but allowing for state transition by incoherent (i.e., global phase-independent) modulation signals at the same time.

As P. W. Anderson, known for the prediction of wave localization in disordered media [13] (i.e. broken translational symmetry), wrote in his essay [14], it is noted that "more is different." In this Dissertation, I deal with several topics regarding the common goal of designing photonic switching or functional devices, in terms of those symmetry breakings.

1.2   Outline of the Dissertation

In this Dissertation, I introduce several topics related to the inverse design of photonic devices, especially in terms of tunability, activeness, and multiple axes, based on the proper breaking of corresponding physical symmetries.

In Chapter 3, at first, I introduce the inverse design method of asymmetric photonic band structures: the three different types of tilted Dirac cones [15]. While the unique conical shape of optical dispersion relations in certain photonic crystal structures becomes the origin of impedance-matched zero-index materials with the application to optical cloaking and metalens devices, they have been in general developed upon the conservation of mirror and rotational symmetries, only providing isotropic optical

behaviors. In this chapter, I suggest and demonstrate a new inverse design method of all types of I, II, and III photonic tilted Dirac cones, according to the criterion with group velocity, with C_{4v}-symmetry-breaking perturbation. Furthermore, I also study the way of opening the gap in such tilted Dirac cones with associated mirror symmetry breaking, which will pave the way for on/off switching within anisotropic light flows.

In Chapter 4, I introduce a data-driven inverse design method of active multilayer films [16]. As machine-learning approaches have been widely adopted in many engineering problems, the application of deep learning to photonic design also has enabled the precise mapping between photonic structures and their corresponding optical responses, which plays a role in both ways: numerical simulator (forward, structures to responses) and generator (backward, responses to structures). In this study, I investigate the relationship between active multilayer-film structures including thermal phase change material and their tunable optical responses, in terms of on/off switching property, material randomness (i.e., the spatial disorder with broken discrete translational symmetry), and optical average transmittance. I also demonstrate the generation of the family of disordered structures with identical optical responses in view of the engineered disorder, as well as the straightforward design of photonic functional devices: angle-switching and broadband switching devices.

In Chapter 5, I study photonic time disorders with broken time-translational symmetry [17]. While the governing equation describing the temporal electromagnetic scattering is in the same form as that of one-dimensional spatial scattering, both expressed by Helmholtz equation, their Green's functions are different: outgoing and causal form for 1D spatial and temporal domains, respectively. Considering such facts, I reformulate the temporal scattering with the newly defined temporal structure factor $S(\omega)$ in the frequency domain, which enables the target separate control of temporal scatterings in both forward and backward directions. I also demonstrate spectral shaping through the order-to-disorder transition, showing the advantage of utilizing the temporal disorder, with practical application: spatial pattern-free color filters with

4

temporal modulation.

Before and after the series of three different topics regarding symmetry breaking for the design of photonic switching devices, I provide detailed theoretical overview (Chapter 2); and supporting information (Appendices A-C) for each topic as well as numerical methods (D).

Chapter 2

Theoretical Background

In this chapter, theoretical backgrounds for the main part of the dissertation are revisited. Starting from the quantum mechanical description of crystals, the mathematical description of photonic crystals is covered with an approximation method for band structures near the Γ-point, as well as the application to photonic zero-index materials. Next, a brief introduction to photonic disorders on the opposite side of photonic crystals is provided, which are described by the structure factors and their connection to scattering phenomena. I also deal with an additional topic regarding time-varying photonics, which extends the spatial-restricted design degrees of freedom into temporal domain.

2.1 Photonic crystals

As a first step, I revisit the quantum mechanical description of crystals; Bloch's theorem [18] states that the electron in a periodically distributed potential $V(\mathbf{r}) = V(\mathbf{r} + \mathbf{R})$ for lattice vectors $\mathbf{R} = n_1\mathbf{a}_1 + n_2\mathbf{a}_2 + n_3\mathbf{a}_3$ ($n_i \in \mathbb{Z}$) has a certain form of the wave function

$$|\psi\rangle = e^{i\mathbf{k}\cdot\mathbf{r}}|u_\mathbf{k}\rangle \tag{2.1}$$

such that $\langle \mathbf{r}|u_\mathbf{k}\rangle = \langle \mathbf{r}+\mathbf{R}|u_\mathbf{k}\rangle$ with the same periodicity $\mathbf{R}$, where $\mathbf{k}$ is a crystal momentum and the Schrödinger equation is given as

$$\mathcal{H}\,|\psi\rangle = \left[\frac{p^2}{2m}+V\right]|\psi\rangle = E\,|\psi\rangle . \tag{2.2}$$

Combining the two Eqs. (2.1) and (2.2), the $\mathbf{k}$-space expression is derived as:

$$\mathcal{H}(\mathbf{k})\,|u_\mathbf{k}\rangle \equiv \left[e^{-i\mathbf{k}\cdot\mathbf{r}}He^{i\mathbf{k}\cdot\mathbf{r}}\right]|u_\mathbf{k}\rangle = E(\mathbf{k})\,|u_\mathbf{k}\rangle . \tag{2.3}$$

The above relation $E(\mathbf{k})$ (or, multiple branches $E_n(\mathbf{k})$ with band index n) between the crystal momentum $\mathbf{k}$ and the energy $E(\mathbf{k})$ is called the dispersion relation or the electronic band structure.

As shown above, Bloch's theorem is one of the most fundamental theorems in solid state physics, especially in crystallography, and it can be proven with discrete translation operator $T_\mathbf{R}$ defined in such a way that $T_\mathbf{R}\,|\mathbf{r}\rangle = |\mathbf{r}+\mathbf{R}\rangle$, which leads to the following properties: successive translations $T_\mathbf{R}T_{\mathbf{R}'} = T_{\mathbf{R}'}T_\mathbf{R} = T_{\mathbf{R}+\mathbf{R}'}$, inverse relation $T_\mathbf{R}^{-1} = T_{-\mathbf{R}}$, and unitarity $T_\mathbf{R}^\dagger = T_\mathbf{R}^{-1}$. Since the Hamiltonian H is periodic, it is trivial that $T_\mathbf{R}$ and H commute to each other, $T_\mathbf{R}H = HT_\mathbf{R}$, and thereby both operators have a simultaneous eigen ket as follows:

$$\mathcal{H}\,|\psi\rangle = E\,|\psi\rangle \tag{2.4}$$

$$T_\mathbf{R}\,|\psi\rangle = c(\mathbf{R})\,|\psi\rangle . \tag{2.5}$$

Due to the mentioned properties of the translation operator $T_\mathbf{R}$, the eigenvalues should satisfy $c(\mathbf{R})c(\mathbf{R}') = c(\mathbf{R}+\mathbf{R}')$ and therefore it can be expressed as an exponential form:

$$c(\mathbf{R}) = [c(\mathbf{a}_1)]^{n_1}[c(\mathbf{a}_2)]^{n_2}[c(\mathbf{a}_3)]^{n_3}, \tag{2.6}$$
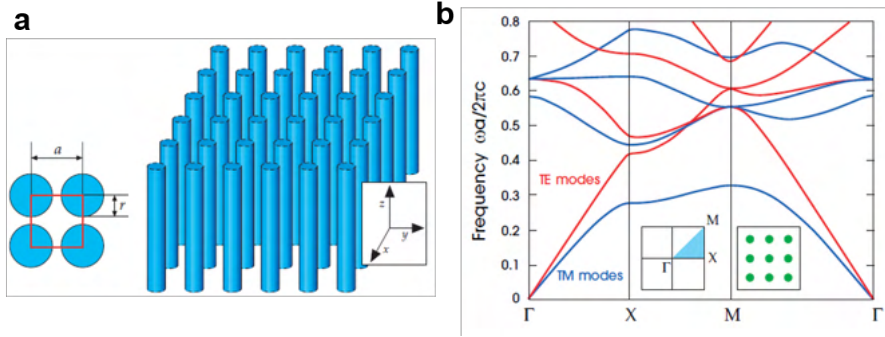
Figure 2.1: Photonic crystal example. (a) Dielectric rods on a square lattice and (b) the corresponding photonic band structure. Adapted from Ref. [1].

---

or, with an arbitrary vector $\mathbf{k}$,

$$c(\mathbf{R}) = e^{-i\mathbf{k}\cdot\mathbf{R}}. \tag{2.7}$$

This eigenvalue equation is expressed in the position space as $\psi(\mathbf{r}-\mathbf{R}) = e^{-i\mathbf{k}\cdot\mathbf{R}}\psi(\mathbf{r})$, which corresponds to the result of Eq. (2.1).

The same approach can be applied in photonics [1]. For simplicity, let's consider an isotropic, nonmagnetic, and source-free optical system with spatially varying permittivity profiles $\epsilon_0\epsilon(\mathbf{r})$. From Maxwell's equations:

$$\boldsymbol{\nabla} \times \mathbf{E} = -\frac{\partial \mathbf{B}}{\partial t} = i\omega\mu_0\mathbf{H} \tag{2.8}$$

$$\boldsymbol{\nabla} \times \mathbf{H} = \frac{\partial \mathbf{D}}{\partial t} = -i\omega\epsilon_0\epsilon(\mathbf{r})\mathbf{E} \tag{2.9}$$

with a harmonic time evolution $\exp(-i\omega t)$, the governing equation for wave propagation is written as

$$\boldsymbol{\nabla} \times \left[\frac{1}{\epsilon(\mathbf{r})}\boldsymbol{\nabla} \times \mathbf{H}\right] = \left(\frac{\omega}{c}\right)^2\mathbf{H}, \tag{2.10}$$

i.e., the eigen problem for a system defined by $\epsilon(\mathbf{r})$, where $c = (\epsilon_0\mu_0)^{-1/2}$ is speed of light. Notably, when the system is periodic with $\epsilon(\mathbf{r}) = \epsilon(\mathbf{r} + \mathbf{R})$, the magnetic field

profile $\mathbf{H}(\mathbf{r})$ is in the vectorial Bloch's form, Eq. (2.1), as

$$\mathbf{H_k}(\mathbf{r}) = e^{i\mathbf{k}\cdot\mathbf{r}}\mathbf{u_k}(\mathbf{r}) \tag{2.11}$$

with a wave vector-dependent frequency (dispersion relation) $\omega(\mathbf{k})$. The periodic struc-ture of optical potential $\epsilon(\mathbf{r})$ or $\mu(\mathbf{r})$ is called the photonic crystal (PC), and its repre-sentative example is illustrated in Fig. 2.1. It is also noted that, the magnetic field $\mathbf{H}$ is a vector quantity, which results in the polarization-dependent band structures for TE and TM modes, as shown by red and blue lines in Fig. 2.1b.

2.1.1 $k \cdot p$ theory for effective Hamiltonian description

Combining Eqs. (2.10) and (2.11), the eigen equation for the Bloch state $\mathbf{u_k}$ can be written as

$$\mathcal{H}(\mathbf{k})\,|\mathbf{u}_{n,\mathbf{k}}\rangle = \lambda_{n,\mathbf{k}}\,|\mathbf{u}_{n,\mathbf{k}}\rangle \tag{2.12}$$

where $\lambda_{n,\mathbf{k}} = [\omega_n(\mathbf{k})/c]^2$, and the $\mathbf{k}$-dependent Hamiltonian

$$
\begin{aligned}
\mathcal{H}(\mathbf{k}) &\equiv e^{-i\mathbf{k}\cdot\mathbf{r}}\left[\boldsymbol{\nabla}\times\frac{1}{\epsilon(\mathbf{r})}\boldsymbol{\nabla}\times\right]e^{i\mathbf{k}\cdot\mathbf{r}} = (\boldsymbol{\nabla}+i\mathbf{k})\times\left[\frac{1}{\epsilon(\mathbf{r})}(\boldsymbol{\nabla}+i\mathbf{k})\times\right]\\
&= \mathcal{H}(0) + \Delta\mathcal{H}(\mathbf{k}) \approx \mathcal{H}(0) + \Delta\mathcal{H}^{(1)}(\mathbf{k}) + \Delta\mathcal{H}^{(2)}(\mathbf{k})
\end{aligned}\tag{2.13}
$$

is regarded as the perturbation to the $\mathcal{H}(0)$ in the vicinity of Γ-point ($\mathbf{k} = 0$) [19]. Especially, the first-order perturbations of momentum vector $\mathbf{k}$ are given as

$$\Delta\mathcal{H}^{(1)} = i\mathbf{k}\times\left[\frac{1}{\epsilon(\mathbf{r})}\boldsymbol{\nabla}\times\right], \quad \Delta\mathcal{H}^{(2)} = \boldsymbol{\nabla}\times\left[\frac{1}{\epsilon(\mathbf{r})}i\mathbf{k}\times\right]. \tag{2.14}$$

Assuming that a few eigenstates $|\mathbf{u}_{n,\Gamma}\rangle$ at the Γ-point are nearly degenerate, the aim here is to obtain an expression for the effective matrix describing the photonic band structure near the Γ-point, based on the first-order degenerate perturbation theory: i.e., the calculation of matrix elemeents $C_{ij}(\mathbf{k}) = \langle\mathbf{u}_{i,\Gamma}|\Delta\mathcal{H}(\mathbf{k})|\mathbf{u}_{j,\Gamma}\rangle$. From the

straightforward vector calculaus,

$$\langle \mathbf{u}_{i,\Gamma}|\Delta\mathcal{H}^{(1)}(\mathbf{k})|\mathbf{u}_{j,\Gamma}\rangle = \frac{1}{V_0}\int d^3r\mathbf{u}^*_{i,\Gamma}(\mathbf{r})\cdot i\mathbf{k}\times\left[\frac{1}{\epsilon(\mathbf{r})}\boldsymbol{\nabla}\times\mathbf{u}_{j,\Gamma}(\mathbf{r})\right] \qquad (2.15)$$

$$= -\frac{i\mathbf{k}}{V_0}\cdot\int d^3r\mathbf{u}^*_{i,\Gamma}(\mathbf{r})\times\left[\frac{1}{\epsilon(\mathbf{r})}\boldsymbol{\nabla}\times\mathbf{u}_{j,\Gamma}(\mathbf{r})\right] = -i\mathbf{k}\cdot\mathbf{P}_{ij},$$

where V_0 is the volume of a unit cell, and the momentum component is defined and denoted by

$$\mathbf{P}_{ij}\equiv\langle\mathbf{u}_{i,\Gamma}|\Delta\mathcal{H}|\mathbf{u}_{j,\Gamma}\rangle_0 = \frac{1}{V_0}\int d^3r\mathbf{u}^*_{i,\Gamma}(\mathbf{r})\times\left[\frac{1}{\epsilon(\mathbf{r})}\boldsymbol{\nabla}\times\mathbf{u}_{j,\Gamma}(\mathbf{r})\right]. \qquad (2.16)$$

Similarly the other term $\langle\mathbf{u}_{i,\Gamma}|\Delta\mathcal{H}^{(2)}(\mathbf{k})|\mathbf{u}_{j,\Gamma}\rangle = i\mathbf{k}\cdot\mathbf{P}^*_{ji}$ is obtained, which result in that

$$C_{ij}(\mathbf{k}) = i\mathbf{k}\cdot(-\mathbf{P}_{ij}+\mathbf{P}^*_{ji}). \qquad (2.17)$$

Next, let's consider a spatial symmetry operation $\mathscr{R}$ and the corresponding matrix representation by orthogonal matrix $R = (R^T)^{-1}$ with $\det(R) = \pm1$, defined as

$$\langle\mathbf{r}|\mathscr{R}\mathbf{u}\rangle = \langle\mathbf{r}|\mathscr{R}|\mathbf{u}\rangle = [\mathscr{R}\mathbf{u}](\mathbf{r}) \equiv R\mathbf{u}(R^{-1}\mathbf{r}). \qquad (2.18)$$

Using the properties $(R\mathbf{u})\cdot(R\mathbf{v}) = \mathbf{u}\cdot\mathbf{v}$, $(R\mathbf{u})\times(R\mathbf{v}) = (\det R)\mathbf{u}\times\mathbf{v}$ and $\mathscr{R}(\boldsymbol{\nabla}\times)\mathscr{R} = (\det R)\boldsymbol{\nabla}\times$, it is derived for the symmetric potential $\mathscr{R}\epsilon^{-1}\mathscr{R}^{-1} = \epsilon^{-1}$ that

$$\mathbf{k}\cdot\mathbf{P}_{ij} = \frac{\mathbf{k}}{V_0}\cdot\int d^3r\,\langle\mathbf{u}_{i,\Gamma}|\mathbf{r}\rangle\times\langle\mathbf{r}|\frac{1}{\epsilon}\boldsymbol{\nabla}\times|\mathbf{u}_{j,\Gamma}\rangle$$

$$= (\det R)\frac{R\mathbf{k}}{V_0}\cdot\int Rd^3rR\,\langle\mathbf{u}_{i,\Gamma}|R^{-1}R\mathbf{r}\rangle\times R\,\langle R^{-1}R\mathbf{r}|\frac{1}{\epsilon}\boldsymbol{\nabla}\times|\mathbf{u}_{j,\Gamma}\rangle$$

$$= (\det R)\frac{R\mathbf{k}}{V_0}\cdot\int d^3r'R\,\langle\mathbf{u}_{i,\Gamma}|R^{-1}\mathbf{r}'\rangle\times R\,\langle R^{-1}\mathbf{r}'|\frac{1}{\epsilon}\boldsymbol{\nabla}\times|\mathbf{u}_{j,\Gamma}\rangle \quad (2.19)$$

where $\mathbf{r}' = R\mathbf{r}$, and by definition in Eq. (2.18),

$$
\begin{aligned}
\mathbf{k} \cdot \mathbf{P}_{ij} &= (\det R) \frac{R\mathbf{k}}{V_0} \cdot \int \mathrm{d}^3\mathbf{r}' \, \langle \mathscr{R}\mathbf{u}_{i,\Gamma} | \mathbf{r}' \rangle \times \langle \mathbf{r}' | \mathscr{R} \frac{1}{\epsilon} \boldsymbol{\nabla} \times | \mathbf{u}_{j,\Gamma} \rangle \\
&= (\det R) \frac{R\mathbf{k}}{V_0} \cdot \int \mathrm{d}^3\mathbf{r}' \, \langle \mathscr{R}\mathbf{u}_{i,\Gamma} | \mathbf{r}' \rangle \times \langle \mathbf{r}' | \mathscr{R} \frac{1}{\epsilon} \mathscr{R}^{-1} \mathscr{R} \boldsymbol{\nabla} \times \mathscr{R}^{-1} | \mathscr{R}\mathbf{u}_{j,\Gamma} \rangle \\
&= \frac{R\mathbf{k}}{V_0} \cdot \int \mathrm{d}^3\mathbf{r}' \, \langle \mathscr{R}\mathbf{u}_{i,\Gamma} | \mathbf{r}' \rangle \times \langle \mathbf{r}' | \frac{1}{\epsilon} \boldsymbol{\nabla} \times | \mathscr{R}\mathbf{u}_{j,\Gamma} \rangle \\
&= R\mathbf{k} \cdot \langle \mathscr{R}\mathbf{u}_{i,\Gamma} | \Delta\mathcal{H} | \mathscr{R}\mathbf{u}_{j,\Gamma} \rangle_0 .
\end{aligned}
\tag{2.20}
$$

This implies that the first-order correction between two eigenmodes in a certain direction may vanish due to the symmetry. For example, for the two-dimensional C_{4v}-symmetric square-lattice photonic crystals, the effective Hamiltonian should be written as

$$
\mathcal{H}(\mathbf{k}) = \lambda_0 I + \Delta\mathcal{H}(\mathbf{k}) = \begin{pmatrix} \lambda_0 & bk_x & bk_y \\ b^* k_x & \lambda_0 & 0 \\ b^* k_y & 0 & \lambda_0 \end{pmatrix}
\tag{2.21}
$$

for the degenerate eigenmodes of diagonalized operator $\mathcal{H}(0) = \lambda_0 I$: monopole-like mode $[1, 0, 0]^T$ and dipole-like modes $[0, 1, 0]^T$ and $[0, 0, 1]^T$ in x- and y-directions, respectively, considering the related mirror and rotational symmetries [19]. Then, the corresponding eigenfrequencies $\omega = c\sqrt{\lambda}$ are obtained as

$$
\omega(\mathbf{k}) = \begin{cases} c\sqrt{\lambda_0} & = \omega_0 \\ c\sqrt{\lambda_0 \pm |b|k} & \approx \omega_0 \pm vk \end{cases},
\tag{2.22}
$$

where $k = |\mathbf{k}|$, $\lambda_0 \equiv (\omega_0/c)^2$ is the degenerate eigenvalue at Γ-point and $v = c^2 |b| / 2\omega_0$ is the group velocity of the conical band structure as known as Dirac cone.

2.1.2 Zero-refractive-index materials

As described previously, the permittivity $\epsilon_0 \epsilon(\mathbf{r})$ and permeability $\mu_0 \mu(\mathbf{r})$ act as an EM potential for light propagation; in detail, the refractive index $n(\mathbf{r}) = \sqrt{\epsilon(\mathbf{r})\mu(\mathbf{r})}$
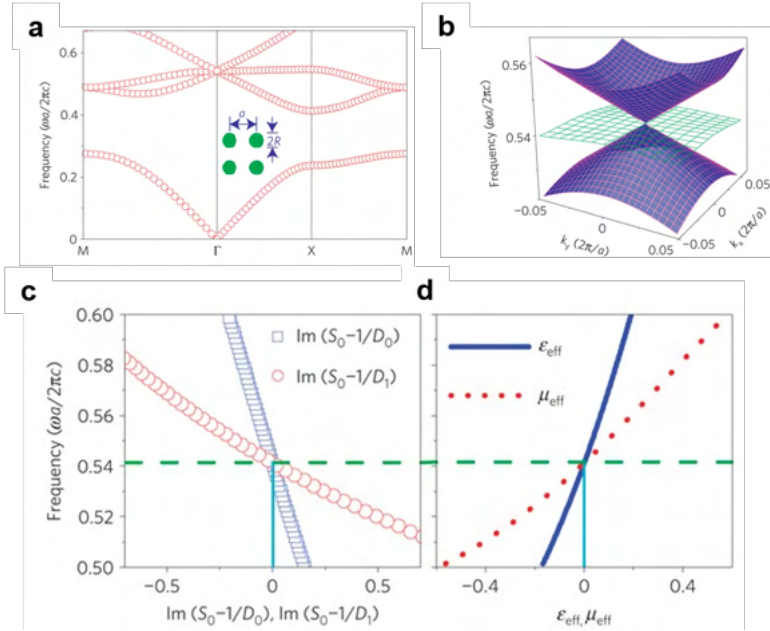
Figure 2.2: Accidentally induced photonic Dirac cones with effective zero refractive index. (a,b) Band structures of dielectric rod structure (inset). (c,d) Multiple scattering theory-related parameters as a function of frequency (c) and the corresponding Wave parameter retrieval (d). Adapted from Ref. [2].

determines the intra-medium optical phase evolution, while the change of relative wave impedance $Z(\mathbf{r}) = \sqrt{\mu(\mathbf{r})/\epsilon(\mathbf{r})}$ at the interface or in the inhomogeneous media governs the scattering phenomena.

For example, consider a infinitesimal $\epsilon(\mathbf{r}) = \mu(\mathbf{r}) = \delta \to 0$ inside a certain region $\mathbf{r} \in X$. In this condition, the refractive index trivially vanishes $n \to 0$, while the wave impedance $Z = 1$ keeps unity. This means that waves propagate without phase evolution inside the region X, but they never feel the existence of boundary X when crossing, from outside to inside of the region, or vice versa. This intriguing phenomenon provides many promising applications, such as optical cloaking or high-efficiency meta-lens.

The importance of a photonic crystal platform is in the possibility of implementing such impedance-matched zero-refractive-index material. When waves are incident to
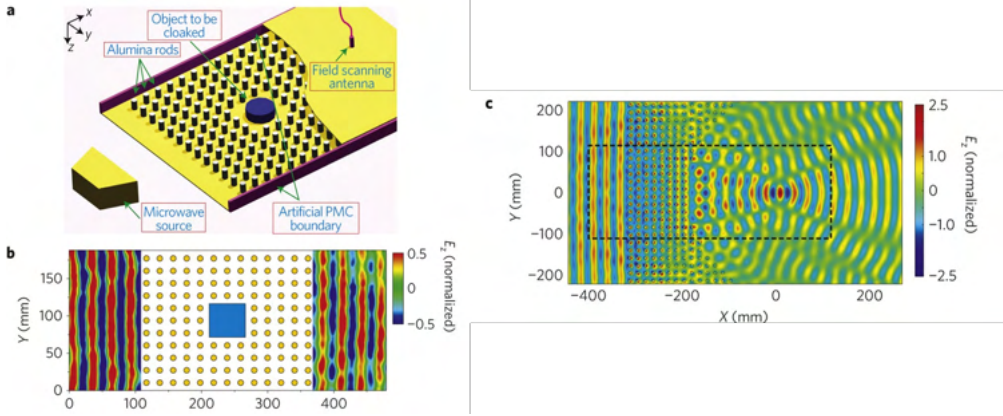
Figure 2.3: Applications of zero-refractive index material. (a) Schematic of the optical cloaking and (b) experimental result of the field distribution. (c) Simulation result of the field distribution for lens focusing application. Adapted from Ref. [2].

the region of photonic crystal, they propagate upon the corresponding Bloch states of the periodically repeated resonance mode profiles on the lattice. Depending on the shape of a mode, it effectively modulates the electric and/or magnetic resonances. For example, a rod-centered monopole-like mode with $\mathbf{k} = 0$ operates in a similar way to the effective electric dipole along z-direction, which cancels the intrinsic dipole moment and thereby makes the propagating wave feels effective zero permittivity $\epsilon_{\mathrm{eff}} = 0$. Similarly, x- or y-directional dipole-like modes form effective current loops in y- and x-directions, respectively, which provide an effective zero permeability $\mu_{\mathrm{eff}} = 0$ in each direction. Therefore, when the resonance frequencies for three (one monopole and two dipoles) different modes accidentally coincide, the photonic crystal structure can support an effective zero-refractive index with finite impedance. This is called the accidental degeneracy and illustrated in Fig. 2.2.

The key feature of zero index comes from Snell's law at the interface, for example, if $n_1 = 0$,

$$n_1 \sin \theta_1 = 0 = n_2 \sin \theta_2, \tag{2.23}$$

which implies that regardless of the internal propagation and the index outside (n_2),

waves are ejected with zero angle $\theta_2 = 0$. This can be applied to two novel optical devices: optical cloaking and meta-lens. As shown in Fig. 2.3, the wave can pass through the object inside the zero index medium. In addition, according to Snell's law, designing the circularly curved interface results in the wave focusing at a distanced focal point.

2.2 Photonic disorders

In contrast to the fact that the discrete translational symmetry in photonic crystals restricts the degrees of freedom for light-matter interaction into a finite region so-called the first Brillouin zone, the absence of such symmetry not only results in the randomized appearance in the real space but also diversifies the corresponding wave responses for different momenta or frequencies in the unbounded reciprocal space.

In this sense, it is necessary to address how to quantify disordered structures and how they are connected to the light-matter interactions (i.e. light scattering), by which one can consider a path in the continuum of order and disorder. Then, the engineering of disorder (Fig. 2.4) corresponds to seeking the optimal path for the combined target wave-material properties, by utilizing full degrees of freedom in relation to the translational symmetry.

2.2.1 Green's function and Born's approximation

Consider a two-dimensional EM potential $\epsilon(\mathbf{r})$ and $\mu(\mathbf{r})$ as an inhomogeneous scatterer in background potential ϵ_{b} and μ_{b}:

$$\epsilon(\mathbf{r}) = \epsilon_{\mathrm{b}}[1 + \Delta\epsilon(x, y)], \quad \frac{1}{\mu(\mathbf{r})} = \frac{1}{\mu_{\mathrm{b}}}[1 + \Delta\beta(x, y)]. \tag{2.24}$$
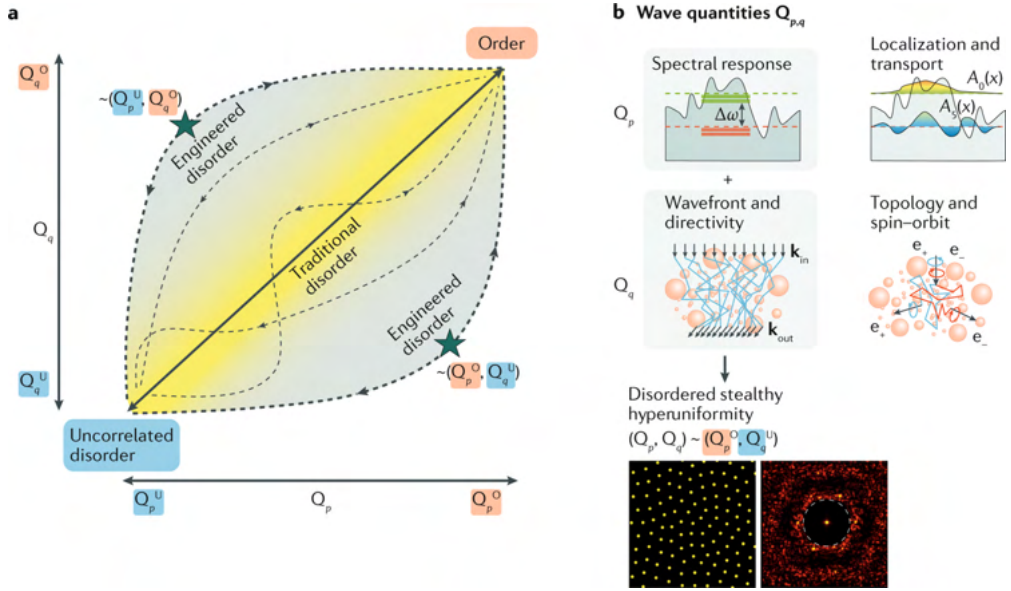
Figure 2.4: A concept of engineered disorder in photonics. (a) A path between complete order and perfectly uncorrelated disorder can be highly diversified: from the traditional direct path in wave parameter space to unconventional bypasses. (b) Examples of wave quantities. Adapted from Ref. [3].

Then, from Maxwell's equation, a time-harmonic z-polarized electric field $\mathbf{E}(\mathbf{r}, t) = \hat{\mathbf{z}}\psi(x, y)e^{-i\omega t}$ is governed by

$$\boldsymbol{\nabla} \times \frac{1}{\mu(\mathbf{r})} \boldsymbol{\nabla} \times \mathbf{E} = \frac{\omega^2}{c^2}\epsilon(\mathbf{r})\mathbf{E}$$

$$\therefore \left[\frac{\partial}{\partial x}\frac{1}{\mu}\frac{\partial}{\partial x} + \frac{\partial}{\partial y}\frac{1}{\mu}\frac{\partial}{\partial y} + k_0^2\epsilon\right]\psi = 0, \tag{2.25}$$

where $k_0 = \omega/c$ is the free-space wave number. Considering the perturbation in Eq. (2.24), the above equation leads to

$$\left(\frac{1}{\mu_{\rm b}}\nabla^2 + k_0^2\epsilon_{\rm b}\right)\psi = -\left[\boldsymbol{\nabla}\frac{\Delta\beta}{\mu_{\rm b}} \cdot \boldsymbol{\nabla}\psi + \frac{\Delta\beta}{\mu_{\rm b}}\nabla^2\psi + k_0^2\epsilon_{\rm b}\Delta\epsilon\psi\right]$$

$$\therefore (\nabla^2 + k_{\rm b}^2)\psi = -(\boldsymbol{\nabla}\Delta\beta \cdot \boldsymbol{\nabla}\psi + \Delta\beta\nabla^2\psi + k_{\rm b}^2\Delta\epsilon\psi) \tag{2.26}$$

where $n_{\rm b} = \sqrt{\mu_{\rm b}\epsilon_{\rm b}}$ is the ambient refractive index and $k_{\rm b} = n_{\rm b}k_0$ is the wave number in background.

Before solving the entire part of Eq. (2.26), Green's function $G(\mathbf{r}, \mathbf{r}')$ is introduced as a point response to the δ-scatterer:

$$\left[\nabla^2 + k_{\rm b}^2\right] G(\mathbf{r}, \mathbf{r}') = \delta(\mathbf{r} - \mathbf{r}'), \tag{2.27}$$

solution of which is well known to be expressed as Hankel function:

$$G^{\rm (2D)}(\mathbf{r}, \mathbf{r}') = -\frac{i}{4} H_0^{(1)}(k_{\rm b}|\mathbf{r} - \mathbf{r}'|). \tag{2.28}$$

When considering the RHS of Eq. (2.26) as $-F(\mathbf{r})$, then the total field is expressed in a convolutional form:

$$\psi_{\rm tot}(\mathbf{r}) = \psi_{\rm inc}(\mathbf{r}) - \int \mathrm{d}^2\mathbf{r}' F(\mathbf{r}')G(\mathbf{r}, \mathbf{r}'), \tag{2.29}$$

where $\psi_{\rm inc} = e^{i\mathbf{k}_{\rm b}\cdot\mathbf{r}}$ is the incident wave propagating in $\mathbf{k}_{\rm b} = k_{\rm b}\hat{\mathbf{k}}$ direction, which is a homogeneous solution, and the last term becomes the scattered wave. Despite the fact that the above equation is in interative form, which includes $\psi_{\rm tot}$-dependent expression within $F(\mathbf{r}')$ in the RHS, it can be approximated only with the first-order term,

$$
\begin{aligned}
F(\mathbf{r}') &= \boldsymbol{\nabla}\Delta\beta(\mathbf{r}') \cdot \boldsymbol{\nabla}\psi_{\rm tot}(\mathbf{r}') + \Delta\beta(\mathbf{r}')\nabla^2\psi_{\rm tot}(\mathbf{r}') + k_{\rm b}^2\Delta\epsilon(\mathbf{r}')\psi_{\rm tot}(\mathbf{r}') \\
&\approx \boldsymbol{\nabla}\Delta\beta(\mathbf{r}') \cdot \boldsymbol{\nabla}\psi_{\rm inc}(\mathbf{r}') + \Delta\beta(\mathbf{r}')\nabla^2\psi_{\rm inc}(\mathbf{r}') + k_{\rm b}^2\Delta\epsilon(\mathbf{r}')\psi_{\rm inc}(\mathbf{r}') \\
&= \left[i\mathbf{k}_{\rm b} \cdot \boldsymbol{\nabla}\Delta\beta + k_{\rm b}^2(\Delta\epsilon - \Delta\beta)\right]e^{i\mathbf{k}_{\rm b}\cdot\mathbf{r}'}.
\end{aligned} \tag{2.30}
$$

This is called the first-order Born approximation, which also corresponds to the same concept for Lippmann-Schwinger equation [20] in quantum scattering theory. Notably, if $\Delta\beta$ is slowly-varying along the direction of incident wave, i.e. $\left|\hat{\mathbf{k}} \cdot \boldsymbol{\nabla}\Delta\beta\right| \ll k_{\rm b}\Delta\beta$, the effective scatterer is reduced to the last two terms: $k_{\rm b}^2(\Delta\epsilon - \Delta\beta)$, and further it can

be cancelled if $\Delta\beta = \Delta\epsilon$.

In general, it is assumed that a medium is non-magnetic: $\mu_{\text{b}} = 1$ and $\Delta\beta = 0$. Then, the total field can be simplified to

$$\psi_{\text{tot}}^{(2\text{D})}(\mathbf{r}) = e^{i\mathbf{k}_{\text{b}}\cdot\mathbf{r}} + \frac{ik_{\text{b}}^2}{4}\int \text{d}^2\mathbf{r}'\Delta\epsilon(\mathbf{r}')e^{i\mathbf{k}_{\text{b}}\cdot\mathbf{r}'}H_0^{(1)}(k_{\text{b}}|\mathbf{r}-\mathbf{r}'|). \tag{2.31}$$

In 3D space, Green's function is agian written as outgoing spherical wave:

$$G^{(3\text{D})}(\mathbf{r}) = -\frac{e^{ik_{\text{b}}|\mathbf{r}-\mathbf{r}'|}}{4\pi|\mathbf{r}-\mathbf{r}'|}. \tag{2.32}$$

Further simplifying with scalar wave approximation in 3D,

$$\psi_{\text{tot}}^{(3\text{D})}(\mathbf{r}) = e^{i\mathbf{k}_{\text{b}}\cdot\mathbf{r}} + \frac{k_{\text{b}}^2}{4\pi}\int \text{d}^3\mathbf{r}'\Delta\epsilon(\mathbf{r}')e^{i\mathbf{k}_{\text{b}}\cdot\mathbf{r}'}\frac{e^{ik_{\text{b}}|\mathbf{r}-\mathbf{r}'|}}{|\mathbf{r}-\mathbf{r}'|}. \tag{2.33}$$

Under the far-field approximation: $|\mathbf{r}| \gg |\mathbf{r}'|$,

$$\left|\mathbf{r}-\mathbf{r}'\right| = \sqrt{r^2 + r'^2 - 2rr'\cos\theta} \approx r - r'\cos\theta \tag{2.34}$$

where θ is the angle between observation point ($\mathbf{r}$)-origin-scattering point ($\mathbf{r}'$) with $\cos\theta = \hat{\mathbf{r}}\cdot\hat{\mathbf{r}}'$. Therefore, Eq. (2.33) is further modified to

$$\begin{aligned}
\psi^{(3\text{D})}(\mathbf{r}) &= e^{i\mathbf{k}_{\text{b}}\cdot\mathbf{r}} + \frac{k_{\text{b}}^2 e^{ik_{\text{b}}r}}{4\pi r}\int \text{d}^3\mathbf{r}'\Delta\epsilon(\mathbf{r}')\exp\left[i\mathbf{k}_{\text{b}}\cdot\mathbf{r}' - ik_{\text{b}}r'\cos\theta\right] \\
&= e^{i\mathbf{k}_{\text{b}}\cdot\mathbf{r}} + \frac{k_{\text{b}}^2 e^{ik_{\text{b}}r}}{4\pi r}\int \text{d}^3\mathbf{r}'\Delta\epsilon(\mathbf{r}')\exp\left(-i\mathbf{q}\cdot\mathbf{r}'\right) \\
&= e^{i\mathbf{k}_{\text{b}}\cdot\mathbf{r}} + \frac{k_{\text{b}}^2 e^{ik_{\text{b}}r}}{4\pi r}\Delta\tilde{\epsilon}(\mathbf{q}),
\end{aligned} \tag{2.35}$$

where $\Delta\tilde{\epsilon}(\mathbf{k})$ is the Fourier transform of the perturbation $\Delta\epsilon(\mathbf{r})$, and $\mathbf{q} = k_{\text{b}}\hat{\mathbf{r}} - \mathbf{k}_{\text{b}} = \mathbf{k}_{\text{sca}} - \mathbf{k}_{\text{inc}}$ denotes the difference between scattering and incident wave vector. It is noted that the scattered wave in Eq. (2.35) is basically in the form of spherical wave centered at the finite size of scatterer, which is modulated by the factor of $\Delta\tilde{\epsilon}(\mathbf{q})$
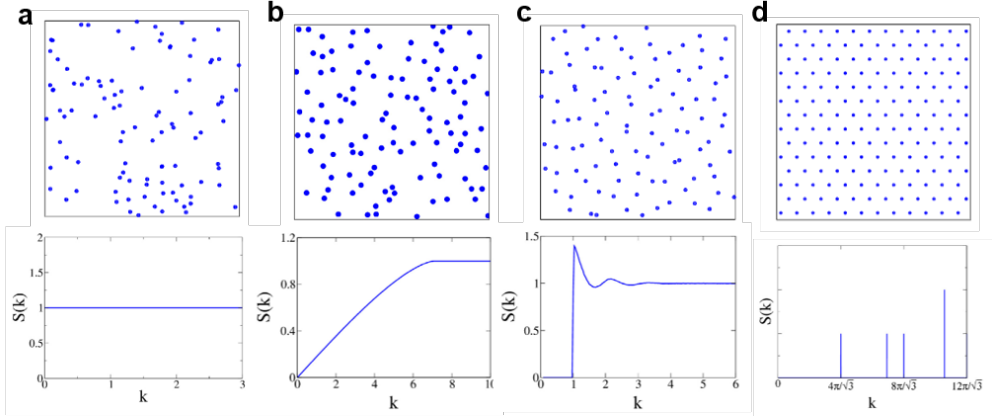
Figure 2.5: Point-process realizations (upper) and the corresponding structure factors (lower): (a) Poisson disorder, $S(\mathbf{k}) = \text{const}$; (b) hyperuniform disorder, $\lim_{|\mathbf{k}| \to 0} S(\mathbf{k}) = 0$, (c) stealthy hyperuniform disorder, $S(|\mathbf{k}| < k_c) = 0$; and (d) crystal, $S(\mathbf{k}) = \sum_{\mathbf{k}_{\text{Bragg}}} c(\mathbf{k}_{\text{Bragg}})\delta(\mathbf{k} - \mathbf{k}_{\text{Bragg}})$. Adapted from Ref. [4].

depending on the direction of scattering.

2.2.2 Structure factor and τ order metric

As described in the previous section, perturbation to an electric permittivity $\Delta\epsilon(\mathbf{r})$ gives rise to spherical scattering with direction-dependent ($\mathbf{k}_{\text{sca}} = \mathbf{q} + \mathbf{k}_{\text{inc}}$) scattered intensity:

$$
\begin{aligned}
I_{\text{sca}}(\mathbf{r}) = |\psi_{\text{sca}}(\mathbf{r})|^2 &\approx \frac{k_{\text{b}}^4}{16\pi^2 r^2}|\Delta\tilde{\epsilon}(\mathbf{q})|^2 \\
&\propto \left| \int \mathrm{d}^3\mathbf{r}'\Delta\epsilon(\mathbf{r}')e^{-i\mathbf{q}\cdot\mathbf{r}'} \right|^2 \\
&= \int \mathrm{d}^3\mathbf{r}'_1\mathrm{d}^3\mathbf{r}'_2\big[\Delta\epsilon^*(\mathbf{r}'_1)\Delta\epsilon(\mathbf{r}'_2)\big]e^{-i\mathbf{q}\cdot(\mathbf{r}'_2-\mathbf{r}'_1)}.
\end{aligned} \tag{2.36}
$$

Now, let's consider disordered perturbations $\Delta\epsilon_i(\mathbf{r})$ with $i = 1, 2, 3, \cdots$, which

constitutes an ensemble of disorder under statistically identical description:

$$\langle \Delta\epsilon(\mathbf{r})\rangle = 0 \qquad\qquad \text{mean,} \qquad (2.37)$$

$$\langle \Delta\epsilon^*(\mathbf{r}_1)\Delta\epsilon(\mathbf{r}_2)\rangle = C(\mathbf{r}_1, \mathbf{r}_2) \qquad\qquad \text{correlation,} \qquad (2.38)$$

where $\langle \cdot \rangle = N^{-1}\sum_{i=1}^{N} \cdot$ denotes the ensemble average. If there is an additional statistical homogeneity: $C(\mathbf{r}_1, \mathbf{r}_2) = C(\mathbf{r}_1 - \mathbf{r}_2)$, the statistical scattering intensity (in average) is directly derived from Eq. (2.36) as

$$
\begin{aligned}
\langle I_{\text{sca}}(\mathbf{r})\rangle &= \frac{k_{\text{b}}^4}{16\pi^2 r^2} \int \mathrm{d}^3\mathbf{r}_1' \mathrm{d}^3\mathbf{r}_2' \left\langle \Delta\epsilon^*(\mathbf{r}_1')\Delta\epsilon(\mathbf{r}_2')\right\rangle e^{-i\mathbf{q}\cdot(\mathbf{r}_2' - \mathbf{r}_1')} \\
&= \frac{k_{\text{b}}^4}{16\pi^2 r^2} \int \mathrm{d}^3\mathbf{r}_1' \mathrm{d}^3\mathbf{r}_2' C(\mathbf{r}_1' - \mathbf{r}_2') e^{-i\mathbf{q}\cdot(\mathbf{r}_2' - \mathbf{r}_1')} \\
&= \frac{k_{\text{b}}^4}{16\pi^2 r^2} \int \mathrm{d}^3\mathbf{r}' \mathrm{d}^3\Delta\mathbf{r}\, C(\Delta\mathbf{r}) e^{i\mathbf{q}\cdot\Delta\mathbf{r}} \approx \frac{k_{\text{b}}^4 V_{\text{sca}}}{16\pi^2 r^2} \tilde{S}(-\mathbf{q}), \qquad (2.39)
\end{aligned}
$$

where $V_{\text{sca}} \sim \int \mathrm{d}^3\mathbf{r}'$ is the volume scale of disordered scatterers, and $\tilde{S}$ denotes the Fourier transform of the correlation function. Here, $\tilde{S}(\mathbf{k})$ is called the *structure factor* (see Fig. 2.5 for example), the statistical description of a disordered scatterer that provides a directional scattering intensity. Also note that tilde notation for $\mathbf{k}$-space representation is possibly omitted throughout the dissertation unless otherwise specified. Motivated from the information that $S(\mathbf{q})$ gives, the inverse design with a target structure factor is also available. The concept of hyperuniformity [4] is a representative example; defined by the state of matter with $\lim_{\mathbf{q}\to 0} S(\mathbf{q}) = 0$, disanrders with hyperuniformity have a long-range order as similar to crystals. Furthermore, a more strict condition: $S(\mathbf{q}) = 0$ for $|\mathbf{q}| = \mathbf{k}_{\text{sca}} - \mathbf{k}_{\text{inc}} < q_0$ derives that there is no backward scattering (i.e., $\mathbf{k}_{\text{sca}} = -\mathbf{k}_{\text{inc}}$) for long-wavelength incidence $k_{\text{inc}} < q_0/2$. This kind of hyperuniform material in strict sense is called the *stealthy* hyperuniformity (Fig. 2.6), implying the existence of "bandgap" even if it is not a crystal.

Associated with the structure factor $S(\mathbf{k})$, the translational order metric τ is origi-
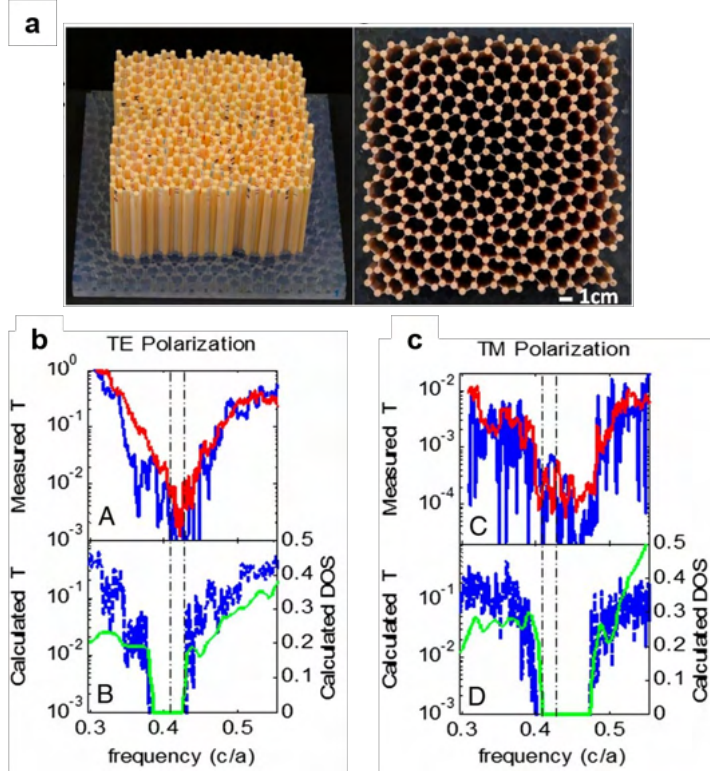
Figure 2.6: Disordered stealthy hyperuniform structure. (a) Designed sample. (b,c) measured and calculated TE (b) and TM (c) transmission, revealing a complete bandgap. Adapted from Ref. [5].

nally defined in point process [4] as

$$\tau[S(\mathbf{k})] \equiv \frac{1}{\rho^2 D^d} \int \frac{\mathrm{d}^d \mathbf{k}}{(2\pi)^d} [S(\mathbf{k}) - 1]^2, \tag{2.40}$$

where D is a characteristic length scale, d is the dimension of the Euclidean space $\mathbb{R}^d$, and ρ is the number density in infinite-volume limit. It is noted that the unity in integral of Eq. (2.40) is the structure factor of Poisson process $1 = S_{\text{Poisson}}(\mathbf{k})$, which means that in the real space, the Poisson process is perfectly uncorrelated: $C_{\text{Poisson}}(\mathbf{r}_1, \mathbf{r}_2) \sim \delta(\mathbf{r}_1 - \mathbf{r}_2)$. Therefore, the τ order metric measures the squared distance how material deviates from the perfectly uncorrelated phase [21]: $\tau = 0$ for

the Poisson process (Fig. 2.5a) and $\tau \rightarrow \infty$ for crystals or quasicrystals (Fig. 2.5d), which only contain δ-function-like Bragg peaks in their structure factors. In terms of the photonic design of deep sub-λ disorder, τ is also in relation to the transmission, localization, and Goos-Hänchen shift in one-dimensional multilayer films [22].

2.3 Time-varying photonics

From the governing equation of source-free ($\rho = 0, \mathbf{J} = 0$) and nonmagnetic ($\mu = 1$) electromagnetic systems:

$$\boldsymbol{\nabla} \times \mathbf{E} = -\frac{\partial \mathbf{B}}{\partial t} \quad \text{and} \quad \boldsymbol{\nabla} \times \mathbf{H} = \frac{\partial \mathbf{D}}{\partial t} \tag{2.41}$$

with non-dispersive and local constitutive relations $\mathbf{D} = \epsilon_0 \epsilon(\mathbf{r}, t) \mathbf{E}$ and $\mathbf{B} = \mu_0 \mathbf{H}$, wave equations of two kinds for specific conditions are derived as follows.

- For spatial systems with $\epsilon = \epsilon(\mathbf{r})$,

$$\boldsymbol{\nabla} \times \boldsymbol{\nabla} \times \mathbf{E} + \frac{\epsilon(\mathbf{r})}{c^2} \frac{\partial^2 \mathbf{E}}{\partial t^2} = 0, \tag{2.42}$$

$$\boldsymbol{\nabla} \times \frac{1}{\epsilon(\mathbf{r})} \boldsymbol{\nabla} \times \mathbf{H} + \frac{1}{c^2} \frac{\partial^2 \mathbf{H}}{\partial t^2} = 0. \tag{2.43}$$

- For temporal systems with $\epsilon = \epsilon(t)$,

$$\frac{1}{c^2} \frac{\partial^2 \mathbf{D}}{\partial t^2} + \frac{1}{\epsilon(t)} \boldsymbol{\nabla} \times \boldsymbol{\nabla} \times \mathbf{D} = 0, \tag{2.44}$$

$$\frac{\partial}{\partial t} \left[\frac{\epsilon(t)}{c^2} \frac{\partial \mathbf{B}}{\partial t} \right] + \boldsymbol{\nabla} \times \boldsymbol{\nabla} \times \mathbf{B} = 0. \tag{2.45}$$

As shown above, two pairs of the wave equations for field components $(\mathbf{E}, \mathbf{H})$ and $(\mathbf{D}, \mathbf{B})$ are equivalent, considering the optical potentials ϵ or ϵ^{-1} which are inverse of each other. Therefore, the temporal analogy of spatial photonic systems provides a lot of insight on extending the degrees of freedom, while also requiring a few considerations:

the difference between the major field components, as well as fundamental energy non-conservativeness due to the broken time-translational symmetry.

2.3.1 Temporal boundary

As described above, in temporal systems the principal EM fields should be $\mathbf{D}$ and $\mathbf{B}$ instead of conventional $\mathbf{E}$ and $\mathbf{H}$ in inhomogeneous media. In this context, the fields that are continuous at "temporal" domain are also derived as $\mathbf{D}$ and $\mathbf{H}$, which is induced by integrating both sides of Maxwell's equations in the infinitesimal vicinity of any temporal boundary at $t = t'$ with $\alpha(t) = 1/\epsilon(t)$:

$$
\mathbf{D}(\mathbf{r}, t' + 0) - \mathbf{D}(\mathbf{r}, t' - 0) = \lim_{\Delta t \to 0} \int_{t'-\Delta t}^{t'+\Delta t} dt \frac{\partial \mathbf{D}}{\partial t} = \frac{1}{\mu_0} \lim_{\Delta t \to 0} \int_{t'-\Delta t}^{t'+\Delta t} dt \boldsymbol{\nabla} \times \mathbf{B} = 0,
$$
$$
\mathbf{B}(\mathbf{r}, t' + 0) - \mathbf{B}(\mathbf{r}, t' - 0) = \lim_{\Delta t \to 0} \int_{t'-\Delta t}^{t'+\Delta t} dt \frac{\partial \mathbf{B}}{\partial t} = -\frac{1}{\epsilon_0} \lim_{\Delta t \to 0} \int_{t'-\Delta t}^{t'+\Delta t} dt \alpha(t) \boldsymbol{\nabla} \times \mathbf{D} = 0.
$$

$$(2.46)$$

Therefore, space-harmonic fields with z-direction momentum k (Fig. 2.7):

$$
\mathbf{D}(\mathbf{r}, t) = \hat{\mathbf{x}} \psi(t) \exp(ikz), \quad \mathbf{B}(\mathbf{r}, t) = \hat{\mathbf{y}} \frac{i\mu_0}{k} \frac{\mathrm{d}\psi(t)}{\mathrm{d}t} \exp(ikz) \tag{2.47}
$$

should be continuous at any discontinuities of $\alpha(t)$, unless there are δ-like spikes with finite areas.

It is also noted that the critical non-dispersive assumption is necessary. In contrast to a linear time-invariant system with time-invariant permittivity tensor $\epsilon'(\tau) = \epsilon \delta(\tau)$

$$
\mathbf{D}(\mathbf{r}, t) = \epsilon_0 \int_0^\infty \mathrm{d}\tau \epsilon'(\tau) \mathbf{E}(\mathbf{r}, t - \tau) = \epsilon_0 \epsilon \mathbf{E}(\mathbf{r}), \tag{2.48}
$$

time-varying systems are expressed using $\epsilon'(t, \tau) = \epsilon(t)\delta(\tau)$ as

$$
\mathbf{D}(t) = \epsilon_0 \int_0^\infty \mathrm{d}\tau \epsilon'(t, \tau) \mathbf{E}(t - \tau) = \epsilon_0 \int_0^\infty \mathrm{d}\tau \epsilon(t)\delta(\tau) \mathbf{E}(t - \tau) = \epsilon_0 \epsilon(t) \mathbf{E}(t).
$$

$$(2.49)$$
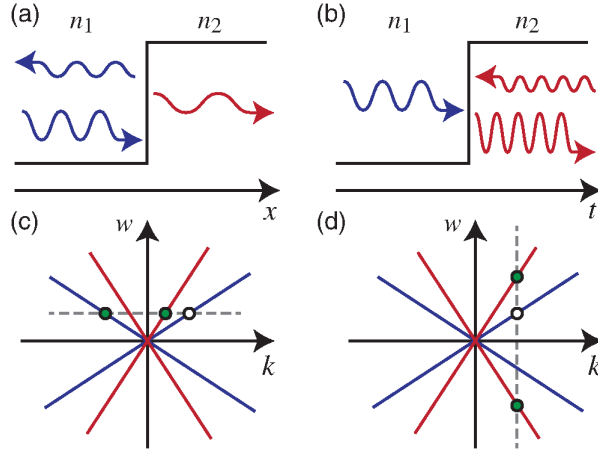
Figure 2.7: Scattering at (a,c) spatial and (b,d) temporal boudaries. In contrast to spatial systems with conserved energy ω (a,c), momentum k is conserved in temporal systems (b,d). Adapted from [6].

More detailed descriptions of general dispersive media can be found in Refs. [23–25].

2.3.2 Open-system nature

The breaking of continuous time-translational symmetry in time-varying electromagnetic (EM) systems inherently implies the breaking of the EM energy conservation. In this section, I discuss the rigorous energy conservation of EM system and the environment. As defined in Ch. 5, I assume an externally modulated time-varying permittivity $\epsilon(t) = \alpha^{-1}(t)$ applied to the infinite spatially homogeneous medium. The fundamental energy description of the EM system starts from the Poynting's theorem:

$$\frac{\partial}{\partial t}(W_{\text{Joule}} + u_{\text{EM}}) = \mathbf{J} \cdot \mathbf{E} + \left[\mathbf{E} \cdot \frac{\partial \mathbf{D}}{\partial t} + \mathbf{H} \cdot \frac{\partial \mathbf{B}}{\partial t} \right] = -\boldsymbol{\nabla} \cdot (\mathbf{E} \times \mathbf{H}), \quad (2.50)$$

where $\mathbf{J}$, $\mathbf{E}$, $\mathbf{D}$, $\mathbf{B}$, and $\mathbf{H}$ are the current density, electric field, displacement field, magnetic flux density, and magnetic field intensity, respectively; $\partial W_{\text{Joule}}/\partial t = \mathbf{J} \cdot \mathbf{E}$ is the Joule heat (i.e., the microscopic mechanical work rate driven by the Lorentz force); $\partial u_{\text{EM}}/\partial t = \mathbf{E} \cdot \partial \mathbf{D}/\partial t + \mathbf{H} \cdot \partial \mathbf{B}/\partial t$ is the rate of internal EM energy;

and $\mathbf{S} = \mathbf{E} \times \mathbf{H}$ is the Poynting vector (i.e., the EM flux). Due to the charge-free and spatially homogeneous system, $\partial W_{\text{Joule}}/\partial t = 0$ and $\boldsymbol{\nabla} \cdot \mathbf{S} = 0$, and therefore $\partial u_{\text{EM}}/\partial t = 0$, revealing the fundamental energy conservation of the entire system. Now we focus on the internal field energy rate:

$$
\begin{aligned}
\frac{\partial u_{\text{EM}}}{\partial t} &= \mathbf{E} \cdot \frac{\partial \mathbf{D}}{\partial t} + \mathbf{H} \cdot \frac{\partial \mathbf{B}}{\partial t} = \frac{\alpha(t)}{\epsilon_0} \mathbf{D} \cdot \frac{\partial \mathbf{D}}{\partial t} + \mathbf{H} \cdot \mu_0 \frac{\partial \mathbf{H}}{\partial t} \\
&= \frac{\alpha(t)}{2\epsilon_0} \frac{\partial |\mathbf{D}|^2}{\partial t} + \frac{\mu_0}{2} \frac{\partial |\mathbf{H}|^2}{\partial t}
\end{aligned} \tag{2.51}
$$

which derives the microscopic EM energy:

$$
u_{\text{EM}} = \int \mathrm{d}t \left[\frac{\alpha(t)}{2\epsilon_0} \frac{\partial |\mathbf{D}|^2}{\partial t} + \frac{\mu_0}{2} \frac{\partial |\mathbf{H}|^2}{\partial t} \right] = \frac{\alpha(t)}{2\epsilon_0} |\mathbf{D}|^2 + \frac{\mu_0}{2} |\mathbf{H}|^2 - \int \frac{\mathrm{d}t}{2\epsilon_0} \frac{\mathrm{d}\alpha(t)}{\mathrm{d}t} |\mathbf{D}|^2 \tag{2.52}
$$

Notably, the third term with integration in Eq. (2.52) vanishes in time-invariant systems with $\partial \alpha/\partial t = 0$, defining the non-conservative "instantaneous EM energy" as

$$
u_{\text{EM}}^0 = \frac{\alpha(t)}{2\epsilon_0} |\mathbf{D}|^2 + \frac{\mu_0}{2} |\mathbf{H}|^2 \tag{2.53}
$$

which only accounts for the snapshot value of EM field energy assuming the time-invariant potential.

The spatially harmonic wave is represented as

$$
\begin{aligned}
\mathbf{D}(\mathbf{r}, t) &= \text{Re} \left[\hat{\mathbf{x}} \psi(t) \exp(ikz) \right] \\
|\mathbf{D}|^2 &= \frac{1}{4} \left[\psi e^{ikz} + \psi^* e^{-ikz} \right]^2 = \frac{1}{4} \left[\psi^2 e^{2ikz} + (\psi^*)^2 e^{-2ikz} + 2|\psi|^2 \right],
\end{aligned} \tag{2.54}
$$

which gives rise to the space-averaged value:

$$
|\mathbf{D}|_{\text{avg}}^2 = \frac{k}{2\pi} \int_0^{2\pi/k} \mathrm{d}z |\mathbf{D}|^2 = \frac{1}{2} |\psi(t)|^2 \tag{2.55}
$$

24

Similarly, the magnetic field is derived from the Maxwell's equation as

$$\mathbf{H}(\mathbf{r}, t) = \mathrm{Re}\left[\hat{\mathbf{y}}\frac{i}{k}\frac{\mathrm{d}\psi(t)}{\mathrm{d}t}\exp(ikz)\right] \tag{2.56}$$

$$\left|\mathbf{H}\right|_{\mathrm{avg}}^2 = \frac{1}{2k^2}\left|\frac{\mathrm{d}\psi(t)}{\mathrm{d}t}\right|^2. \tag{2.57}$$

As a result, the space-averaged EM field energy leads to

$$
\begin{aligned}
\frac{\mathrm{d}u_{\mathrm{EM,avg}}}{\mathrm{d}t} &= \frac{\alpha(t)}{2\epsilon_0}\frac{\mathrm{d}}{\mathrm{d}t}\left|\mathbf{D}\right|_{\mathrm{avg}}^2 + \frac{\mu_0}{2}\frac{\mathrm{d}}{\mathrm{d}t}\left|\mathbf{H}\right|_{\mathrm{avg}}^2 \\
&= \frac{\alpha(t)}{4\epsilon_0}\frac{\mathrm{d}}{\mathrm{d}t}\left|\psi(t)\right|^2 + \frac{\mu_0}{4k^2}\frac{\mathrm{d}}{\mathrm{d}t}\left|\frac{\mathrm{d}\psi(t)}{\mathrm{d}t}\right|^2 \\
&= \frac{1}{4\epsilon_0}\left[\alpha(t)\frac{\mathrm{d}\left|\psi\right|^2}{\mathrm{d}t} + \frac{1}{(ck)^2}\frac{\mathrm{d}}{\mathrm{d}t}\left|\frac{\mathrm{d}\psi(t)}{\mathrm{d}t}\right|^2\right] \tag{2.58}
\end{aligned}
$$

$$u_{\mathrm{EM,avg}}(t) = \frac{1}{4\epsilon_0}\left[\alpha(t)|\psi(t)|^2 + \frac{1}{(ck)^2}\left|\frac{\mathrm{d}\psi(t)}{\mathrm{d}t}\right|^2 - \int_{-\infty}^{t}\mathrm{d}t'\frac{\mathrm{d}\alpha(t')}{\mathrm{d}t'}|\psi(t')|^2\right] \tag{2.59}$$

Resultingly, the space-averaged instantaneous EM field energy is expressed as

$$u_{\mathrm{EM,avg}}^0(t) = \frac{1}{4\epsilon_0}\left[\alpha(t)|\psi(t)|^2 + \frac{1}{(ck)^2}\left|\frac{\mathrm{d}\psi(t)}{\mathrm{d}t}\right|^2\right] \tag{2.60}$$

The time derivative of $u_{\mathrm{EM,avg}}^0(t)$ therefore corresponds to the energy gain (positive rate) or the loss (negative rate), which is externally driven by signal power to the system from the environment:

$$P_{\mathrm{in}}(t) = \frac{\mathrm{d}u_{\mathrm{EM,avg}}^0(t)}{\mathrm{d}t}. \tag{2.61}$$

Notably, it is possible to approximate the energy gain for a single-frequency wave obtained from a weakly perturbed potential $\alpha(t) = \alpha_{\mathrm{b}}[1 + \Delta\alpha(t)]$, using the time-domain version of structure factor similar to Eq. (2.39). The total field is written as

$$\psi(t) = \psi_{\text{inc}}(t) + \psi_{\text{sca}}(t) = e^{-i\omega_{\text{b}}t} + \left[s_{\text{FW}}(t)e^{-i\omega_{\text{b}}t} + s_{\text{BW}}(t)e^{+i\omega_{\text{b}}t} \right], \quad (2.62)$$

where $\omega_{\text{b}} = ck\sqrt{\alpha_{\text{b}}}$ is the incident frequency and $s_{\text{FW,BW}}(t)$ is the instantaneous scattering amplitude in forward and backward directions, respectively. Due to the range of potential change being extremely limited, $s_{\text{FW,BW}}(t)$ are slowly varying and mostly focused at $\omega = 0$ component in the frequency domain compared to the carrier frequency ω_{b}, which results in the follwoing approximation:

$$\begin{aligned}
\frac{\mathrm{d}\psi}{\mathrm{d}(\omega_{\text{b}}t)} &= -i\left[(1 + s_{\text{FW}})e^{-i\omega_{\text{b}}t} - s_{\text{BW}}e^{+i\omega_{\text{b}}t} + i\frac{\mathrm{d}s_{\text{FW}}}{\mathrm{d}(\omega_{\text{b}}t)}e^{-i\omega_{\text{b}}t} + i\frac{\mathrm{d}s_{\text{BW}}}{\mathrm{d}(\omega_{\text{b}}t)}e^{+i\omega_{\text{b}}t} \right] \\
&\approx -i\left[(1 + s_{\text{FW}})e^{-i\omega_{\text{b}}t} - s_{\text{BW}}e^{+i\omega_{\text{b}}t} \right]. \quad (2.63)
\end{aligned}$$

Then, the instantaneous EM energy in Eq. (2.60) is written as

$$\begin{aligned}
u_{\text{EM}}^0(t) &= \frac{\alpha_{\text{b}}}{4\epsilon_0}\left\{ [1 + \Delta\alpha(t)]|\psi(t)|^2 + \left| \frac{\mathrm{d}\psi}{\mathrm{d}(\omega_{\text{b}}t)} \right|^2 \right\} \\
&\approx \frac{\alpha_{\text{b}}}{4\epsilon_0}\left[2\left(|1 + s_{\text{FW}}|^2 + |s_{\text{BW}}|^2 \right) + \Delta\alpha(t)|\psi(t)|^2 \right], \quad (2.64)
\end{aligned}$$

which results in the energy gain after the end of finite perturbation (i.e., $\Delta\alpha(t > T) = \Delta\alpha(t < 0) = 0$) as

$$\begin{aligned}
\Delta u_{\text{EM}}^0 &= u_{\text{EM}}^0(t > T) - u_{\text{EM}}^0(t \to -\infty) \\
&= \frac{\alpha_{\text{b}}}{2\epsilon_0}\left[|1 + s_{\text{FW}}|^2 + |s_{\text{BW}}|^2 - 1 \right] = \frac{\alpha_{\text{b}}}{2\epsilon_0}\left[|s_{\text{FW}}|^2 + |s_{\text{BW}}|^2 + 2\operatorname{Re} s_{\text{FW}} \right].
\end{aligned}$$
$$(2.65)$$

As will be discussed in Ch. 5, the scattering intensities $|s_{\text{FW,BW}}|^2$ are statistically governed by the time-domain analog of structure factor: $S(\omega = 0, 2\omega_{\text{b}})$, respectively, while the last term $\operatorname{Re} s_{\text{FW}}$ will vanish due to the uniform phase distribution from the

random-generated ensemble of disorder realizations. Significantly, Eq. (2.65) implies that the temporal structure factor $S(\omega)$ corresponds to the power spectral density, and the incident wave absorbs the selective portion (near $\omega = 0$ and $2\omega_{\mathrm{b}}$) of the total applied power distribution $S(\omega)$.

Chapter 3

Engineered Band Structures

Band engineering near Dirac points is an emerging topic in condensed matter physics and photonics, enabling multifaceted devices of record-high conductivity and zero refractive index in both electronic and photonic structures. Recently, an extended class of Dirac cone, type I, II, or III, has attracted much attention with its controlled directionality of singular wave behaviors near the Dirac points. However, despite the significance of the discovery and applications of each type of Dirac cone, the theoretical framework and unified design structure bridging different types of Dirac cones have not been clearly elucidated.

In this chapter, I introduce a published work [15] by coauthors (Prof. Sunkyu Yu and Prof. Namkyoo Park) with permission (©American Physical Society): a universal design platform for all types of photonic Dirac cones, revealing the key parameter determining their types and transformations. Starting from the accidentally induced photonic Dirac cone, it is shown that the inverse design of an optical potential landscape enables the deterministic control of the spectral ordering, which leads to designer construction of each type of Dirac cone. This approach will pave the way for the design of artificial degeneracies with tunable anisotropy for general wave systems.

3.1 Introduction

A Dirac cone, a conical dispersion with point degeneracy (Dirac point; DP), has been a hot topic of research in condensed matter physics with its unique property of massless transport of electrons [26]. This novel feature, originating from the sublattice symmetry in a honeycomb lattice, has led to significant advances in high-performance graphene electronics [27, 28] and spintronics [29, 30]. Because of the universality of band theory in wave phenomena, the physics and applications of DPs have also been widely reproduced in other wave systems, including photonic [2, 31–33], phononic [34, 35], and circuit [36, 37] structures. In particular, the photonic Dirac cone (PDC), accidentally induced at the Γ-point with an additional flat band, became a representative optical counterpart of massless electronic transport, achieving amplitude-phase-conserved wave propagation with a zero refractive index. The Dirac frequency in PDC then operates as an electromagnetic (EM) resonant frequency where the effective electric and magnetic dipole moments simultaneously cancel external fields, defining the phase transition for optical materials between negative and positive refractive indices [2, 32].

On the other hand, the physics and its applications near DPs have been further extended by imposing a perturbation on the perfect conical band structure (Fig. 3.1a), which derives significant phase change around the DP. For example, in quantum mechanics, a bandgap opening realized by broken time-reversal symmetry with the external magnetic field gives rise to nonzero Chern numbers and topological edge states [38]. Similar band manipulations by artificial gauge fields have also been reported with the emergence of nontrivial spin Chern numbers and the analogy of the quantum spin Hall effect in classical wave systems: photonics [39, 40], acoustics [41, 42], and electric circuit systems [36, 37]. Different classes of *tilted* Dirac cones have also drawn much recent interest with their anisotropic Fermi surfaces. In terms of the band slopes near DPs, Dirac cones are classified by types I, II, or III, each having opposite signs, the same signs, or a zero of group velocities (Figs. 3.1b-d), resulting in different anisotropic Fermi

surfaces (or isofrequency contours; IFCs) at the Dirac frequency [43, 44]. While tilted type-I and type-III (as an extreme case of type-I) DPs are realized by imposing smooth deformations on structures both in quantum systems [45, 46] and photonics [44, 47, 48], it was only recently that type-II Dirac/Weyl points with extreme nonreciprocity have drawn attention [43, 49], reproduced in photonics [50–53] and acoustics [54–56]. While each type of tilted Dirac cone in given structures has been well elucidated in terms of its mechanisms and behavior and is also considered a promising platform for imposing directionality on Dirac cones, the study on the relationships between different type of DPs in terms of physics and platform compatibility is rare.

In this chapter, we present an integrated analysis for all types of tilted PDCs and thus achieve a universal design framework, to enable the deterministic realization and transition between different types of tilted Dirac cones. Starting from the effective Hamiltonian theory, we first classify deformed band structures of the accidental PDC [2] in terms of the spectral ordering of eigenvalues at the Γ-point. we then propose a perturbative inverse-design method which utilizes the spatial profile of a *target* eigenmode, achieving the successful generation of deformed dispersions that cover all types of tilted PDCs. Under the same template, we also study and reveal the frequency-dependent topological transition of IFCs in the momentum space. The effect of mirror symmetry breaking is also discussed in regard to the opening of the symmetry-protected bandgap.

3.2 Effective Hamiltonian description of photonic Dirac cones

Without loss of generality, we consider a two-dimensional (2D) square-lattice photonic crystal (PC) consisting of isotropic and nonmagnetic materials for transverse-magnetic propagations. In these platforms, the application of the $k \cdot p$ perturbation theory (see Sec. 2.1.1 and Ref. [57]) allows the approximation of band structures in the vicinity of the Γ-point, using eigenmodes and corresponding eigenfrequencies at the Γ-point. For nearly
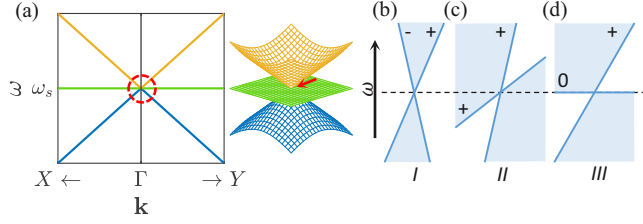
Figure 3.1: Tilted Dirac cones. (a) Band dispersion of a photonic Dirac cone with accidental triple degeneracy $\omega_s = \omega_{px} = \omega_{py}$ along the ΓX and ΓY paths. ω_s and $\omega_{px,py}$ are the eigenfrequencies of a monopole and dipoles at the Γ-point, and Γ, $X(Y)$ are the reciprocal points in the square Brillouin zone (BZ). (b-d) Schematics of vertical cross-sections for tilted PDCs: (b) type-I, (c) type-II, and (d) type-III.

---

degenerate dipole modes $|p_{x,y}\rangle$ and monopole mode $|s\rangle$, the effective Hamiltonian for the eigenvalue equation $H(\mathbf{k}) |u_\mathbf{k}\rangle = \omega(\mathbf{k}) |u_\mathbf{k}\rangle$ then becomes

$$H(\mathbf{k}) = \begin{bmatrix} \omega_s & v_x k_x & v_y k_y \\ v_x k_x & \omega_{px} & 0 \\ v_y k_y & 0 & \omega_{py} \end{bmatrix}, \tag{3.1}$$

where the diagonal terms (ω_s and $\omega_{px,py}$) are the unperturbed eigenfrequencies of a monopole and x-, y-dipoles at the Γ-point, respectively, satisfying $H(0) |s\rangle = \omega_s |s\rangle$ and $H(0) |p_{x,y}\rangle = \omega_{px,py} |p_{x,y}\rangle$. The off-diagonal terms ($v_x k_x$ and $v_y k_y$) are $\mathbf{k}$-dependent perturbations to the Γ-point Hamiltonian with group velocity coefficients $v_{x,y}$ [58]. For other lattice structures such as hexagonal [40] and rhombic lattices [59], a similar formulation using their eigenmodes can be developed in a similar way.

For simplicity, we focus on the band structures along the k_x-axis ($k_y = 0$). Along the axis, Hamiltonian H is decomposed into a 1×1 scalar operator for the p_y-mode and a 2×2 Hamiltonian matrix for the coupled s- and p_x-modes. Three bands of the Hamiltonian are then obtained as a decoupled flat band $\omega_{\text{flat}}(k_x; k_y = 0) = \omega_{py}$ and

the other coupled bands:

$$\omega_{\pm}(k_x; k_y = 0) = \frac{\omega_s + \omega_{px} \pm \sqrt{(\omega_s - \omega_{px})^2 + 4v_x^2 k_x^2}}{2} \tag{3.2}$$

with corresponding eigenmodes $|\text{flat}\rangle = |p_y\rangle$ and $|\pm\rangle = c_s^{(\pm)} |s\rangle + c_{px}^{(\pm)} |p_x\rangle$ for some normalized coefficients $c_s^{(\pm)}$ and $c_{px}^{(\pm)}$. We note that the geometry of the coupled bands $\omega_{\pm}$ near the Γ-point is mainly determined by the "diagonal" components ω_s and $\omega_{px,py}$ of the Hamiltonian.

According to Eq. (3.2), we note that three-level band structures of PDCs can be generally classified into the following five regimes, with respect to Γ-point spectral distributions: (A) $\omega_{px} = \omega_{py} = \omega_s$ (Fig. 3.1a), (B) $\omega_{px} = \omega_{py} < \omega_s$ (Fig. 3.2a), (C) $\omega_{py} < \omega_{px} = \omega_s$ (Fig. 3.2b), (D) $\omega_{py} < \omega_{px} = \omega_s$ (Fig. 3.2c), and (E) $\omega_{py} = \omega_s = \omega_{px}$ (Fig. 3.2d). In terms of this spectral ordering, it now becomes easier and clearer to classify different types of PDC. First, class A, known as the accidental degeneracy [2, 32], corresponds to the type-I PDC with an additional flat band (green band in Fig. 3.1a). Classes B-E correspond to the deformed dispersion of the accidental PDC (class A). Typical C_{4v}-symmetric PCs exemplifies case B with parabolic dispersions due to nonzero $\omega_{px,py} - \omega_s$ (Fig. 3.2a) [1], while case D signifies the directional Dirac dispersion at the Γ-point [60]. In view of the inverse-design approach of the PDC, which will be expanded in Sec. 3.3, it is worth mentioning that the Γ-point eigenfrequencies $\omega_{px,py}$ and ω_s strongly affect the effective electric and magnetic responses of materials and the detailed band geometry [60, 61]. Also see Appendix A.1.

Classifying the various dispersions of deformed PDC structures with the single Hamiltonian formulation, we search for the variations of tilted PDCs. For anisotropic classes C-E with broken C_{4v}-symmetry, type-III PDCs can be achieved away from the Γ-point (black circles and arrows in Figs. 3.2b-d). As an example, we consider the emergence of a type-III PDC in class D of $\Delta\omega_{py} = \omega_{py} - \omega_s < 0$ (Fig. 3.2c), away from the Γ-point. For this case, since the band dispersions are given by $\omega_{\text{flat}}(k_x; k_y = 0) = \omega_{py}$ and $\omega_{\pm}(k_x; k_y = 0) = \omega_s \pm |v_x k_x|$ from Eq. (3.2), there exists a single intersecting
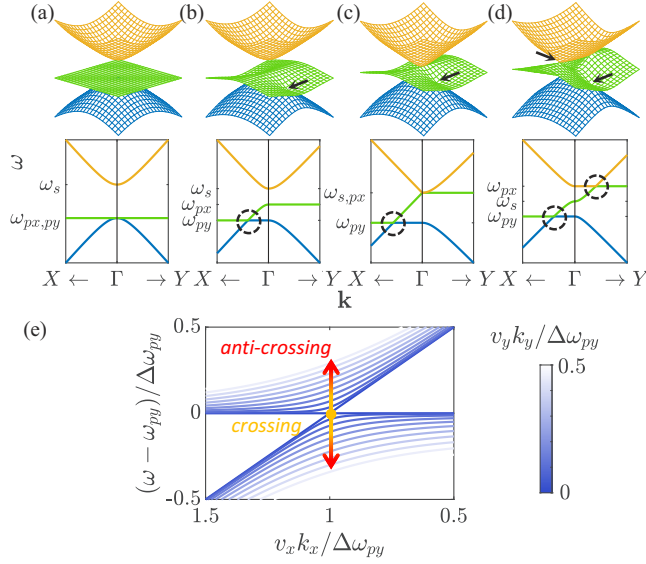
Figure 3.2: Deformation of PDCs. (a-d) Deformed band structures with Γ-point spectral distributions $\omega_{px} = \omega_{py} < \omega_s$, $\omega_{py} < \omega_{px} < \omega_s$, $\omega_{py} < \omega_{px} = \omega_s$, and $\omega_{py} < \omega_s < \omega_{px}$, respectively. The dotted circles and arrows in (b-d) indicate the emergence of type-III PDCs through anisotropic deformations. (e) Projections of band structures on the normalized $k_x - \omega$ plane, near the type-III PDC in (c), describing the band crossing and anti-crossing depending on the values of k_y. The graded color of lines represents the values of normalized k_y.

point between $\omega_-(k_x; k_y = 0)$ and $\omega_{\text{flat}}(k_x; k_y = 0)$ bands at $k_x = k_{x0} \equiv |\Delta\omega_{py}/v_x|$. In contrast, a nonzero k_y in the effective Hamiltonian leads to anti-crossing between two bands with the frequency splitting $|\omega_- - \omega_{\text{flat}}| \sim \sqrt{2}v_y k_y$ with mode coupling (Fig. 3.2e, also see Appendix A.2 for the derivation). The crossing and anti-crossing depending on k_y prove that there is a *point* degeneracy at $\mathbf{k} = (k_{x0}, 0)$ for the formation of a PDC. Because of the zero group velocity $\partial\omega_{\text{flat}}/\partial k_x = 0$, the band structures near this band-crossing point are classified as type III, which is also discussed in a similar way in Ref. [44]. we further note for later discussions that the bending of the flat band $\omega_{\text{flat}}(k_x)$ also allows the transition of type-III PDCs to type-I or type-II PDCs. Most importantly, we show that this transition between different types of the PDC can be

controlled by the spectral separation $\Delta\omega_{px,py} \equiv \omega_{px,py} - \omega_s$.

3.3 Inverse design of tilted Dirac cones

To achieve the optical potential for the target Hamiltonian in Eq. (3.1), we apply the inverse-molding of the potential landscape from the spatial profile of an eigenmode, which has been adopted in the design of disordered structures [62], non-Hermitian potentials [63], and the transverse spin of light [64]. For the Helmholtz equation

$$\left[\nabla^2 + k_0^2 \epsilon(\mathbf{r})\right] E_z(\mathbf{r}) = 0, \tag{3.3}$$

the target profile of the Bloch wave $E_z(\mathbf{r}) = e^{i\mathbf{k}\cdot\mathbf{r}} u_{\mathbf{k}}(\mathbf{r})$ at the design point $(\mathbf{k}, \omega)$ provides a necessary landscape of permittivity in a unit cell:

$$\epsilon(\mathbf{r}) = \frac{(k^2 - \nabla^2)u_{\mathbf{k}} - 2i\mathbf{k} \cdot \nabla u_{\mathbf{k}}}{k_0^2 u_{\mathbf{k}}}, \tag{3.4}$$

where $k = |\mathbf{k}|$, $k_0 = \omega/c$, and the modal profile inside the unit cell $u_{\mathbf{k}}(\mathbf{r})$ has the same periodicity as $\epsilon(\mathbf{r})$. For the three eigenmodes (Fig. 3.3b), the inverse design process allows the designer alteration of the two $p_{x,y}$-eigenmodes and their eigenfrequencies using the spatial profile of target s-mode $u_s(\mathbf{r}) = \langle\mathbf{r}|s\rangle$.

In detail, we introduce a C_{2v}-symmetric perturbation $f(\mathbf{r})$ (Fig. 3.3d) to the s-mode of the potential (Fig. 3.3c) for class A (Fig. 3.1a). This wavefunction perturbation on a target eigenmode $|s\rangle = \exp\left[f(\mathbf{r})\right]|s_0\rangle$ (Fig. 3.3e, upper) then leads to the designed potential landscape $\epsilon(\mathbf{r})$ (Fig. 3.3e, lower), with Eq. (3.4) at fixed momentum and frequency $(\mathbf{k}, \omega) = (0, \omega_{s0})$. we emphasize that the inverse-designed potential from this C_{2v}-symmetric perturbation maintains the original C_{2v}-symmetry while keeping the orthogonality between the bases of the Hamiltonian in Eq. (3.1). Critically, their mode frequencies are adjusted by the modified effective index for each mode, in such a way to derive the *nonzero* dipole resonance shifts $\Delta\omega_{px,py} \neq 0$ and the *zero* monopole
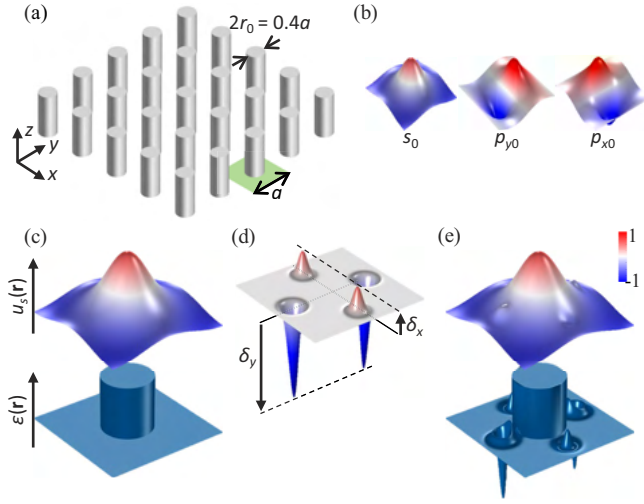
Figure 3.3: (a) Dielectric rod structure on a square lattice (radius $r_0 = a/5$, dielectric constant $\epsilon = 12.5$) [2] as a seed potential for class A in Fig. 3.1a. (b) Three eigenmode profiles (one monopole s_0 and two dipoles $p_{x0,y0}$) at the Γ-point for the potential in (a), with degenerate eigenfrequency $\omega a/2\pi c = 0.541$. (c-e) Inverse design schematics. (c) The unperturbed PDC potential $\epsilon_0(\mathbf{r})$ (lower) and its s-mode profile (upper). (d) The C_{2v}-symmetric perturbation function $f(\mathbf{r})$ with control parameters δ_x and δ_y. (e) A new target s-mode profile (upper), and the inversely designed potential with the fixed eigenfrequency $\omega_s = \omega_{s0}$ (lower). The target mode is defined by multiplying the perturbation function $f(\mathbf{r})$ with the unperturbed s-mode profile.

mode resonance shift $\Delta\omega_s = 0$, thereby breaking the accidental degeneracy. To achieve the target $\Delta\omega_{px,py}$, we utilize parameters (δ_x, δ_y) that separately determine the strength of the perturbation $f(\mathbf{r})$ in each axis, as described in Appendix A.3 with detailed numerical treatment. See also Appendix A.4 for a dipole-based design approach, where the perturbation is applied to p_x-mode.

To verify the proposed idea, the dipole frequency shifts $\Delta\omega_{px,py}$ are calculated with the finite element method (FEM) [65] as a function of (δ_x, δ_y). The contours of modal separations $\Delta\omega_{px}$ (dashed lines) and $\Delta\omega_{py}$ (solid lines) in Fig. 3.4a are almost perpendicular to the δ_x and δ_y axes, respectively, proving the nearly independent control of ω_{px} and ω_{py} with respect to the fixed ω_s. we emphasize that all five classes discussed

in Figs. 3.1 and 3.2 are classified as different regimes in the (δ_x, δ_y) plane (Fig. 3.4a: $\Delta\omega_{px} = \Delta\omega_{py} = 0$, point A; $\Delta\omega_{px} = \Delta\omega_{py}$, line B; $\Delta\omega_{px}\Delta\omega_{py} = 0$, lines D; gray and yellow regions C, E), proving the emergence of entire classes of the deformed structures within a single platform.

Because the flat band has a nonzero curvature in a real structure, especially for large k values, other types of PDC having a positive or negative slope are expected to emerge, as derivatives of type III. For precise analysis beyond the $k \cdot p$ effective Hamiltonian for large k, we use the FEM in the analysis of the dispersions. The result of the FEM analysis produces a small but positive group velocity $0 < \partial\omega_{\text{flat}}/\partial k_x \ll |v_x|$ as expected, providing an additional degree of freedom for the design of tilted PDCs. For instance, we consider three cases $P_{1,2,3}$ of deformation, class D in Fig. 3.4(a), having $\Delta\omega_{py}a/2\pi c = +0.02, -0,02$, and $+0.003$ (Figs. 3.4e-g), respectively, while preserving $\Delta\omega_{px} = 0$. As shown in Figs. 3.4e-g, the dispersion and type of the PDC is then controlled by $\Delta\omega_{py}$, which determines the relative position of the flat-like band frequency: below, above, or near the frequency $\omega_s = \omega_{px} \sim 0.541 \times 2\pi c/a$ for points $P_{1,2,3}$, respectively. The flat band for each point then intersects with different dispersion bands having opposite slope $\omega_\pm(k_x) \approx \omega_s \pm |v_x k_x|$: P_1 for ω_+ and $P_{2,3}$ for ω_-. Further, it is noted that these spectral relations follow the general classification of the tilted PDCs: type I ($\partial\omega_{\text{flat}}/\partial k_x > 0$, $\partial\omega_-/\partial k_x < 0$, Fig. 3.1b) for P_1, type II ($\partial\omega_{\text{flat}}/\partial k_x > 0$, $\partial\omega_+/\partial k_x > 0$, Fig. 3.1c) for P_2, and type III ($\partial\omega_{\text{flat}}/\partial k_x \sim 0$, $\partial\omega_+/\partial k_x > 0$, Fig. 3.1d) for P_3. Further discussions on the control of the group velocity $\partial\omega_{\text{flat}}/\partial k_x$ [66] are given in Appendix A.5.

Furthermore, each type of achieved PDC leads to the different classes of the topological transition in k-space [64, 67, 68] around the DPs: elliptic-to-elliptic (Fig. 3.4h), hyperbolic-to-hyperbolic (Fig. 3.4i), and asymmetric hyperbolic-to-hyperbolic (Fig. 3.4j) transitions, respectively for types I-III. Thus, the successful design of all types of PDCs in a single platform and the following tunable topological transition in the momentum space are proved, importantly, in addition to significantly distinct IFCs

at the Dirac frequency (single-point, two-line, and asymptotically single-line IFCs in types I-III, respectively). we emphasize that the distinctive IFC of each Dirac cone is determined by the separation of participating states [yellow, green, or blue colors in Figs. 3.4e-g); the type I and II each shows the ω-domain and k-domain separation of states, respectively, while the type III presents the simultaneous separation both in k- and ω-domains. Near these distinctive IFCs, a significantly different momentum distribution around the original DP can be achieved even with the small frequency shift of the flat band. Although the observed transition corresponds to the small-signal momentum perturbation around the Dirac momentum state, when the time-reversal symmetry is broken and thus the similar transition can occur at the Γ-point DP, the abrupt material phase transition with positive (elliptic) to negative (hyperbolic) refraction can also be realized with broken reciprocity.
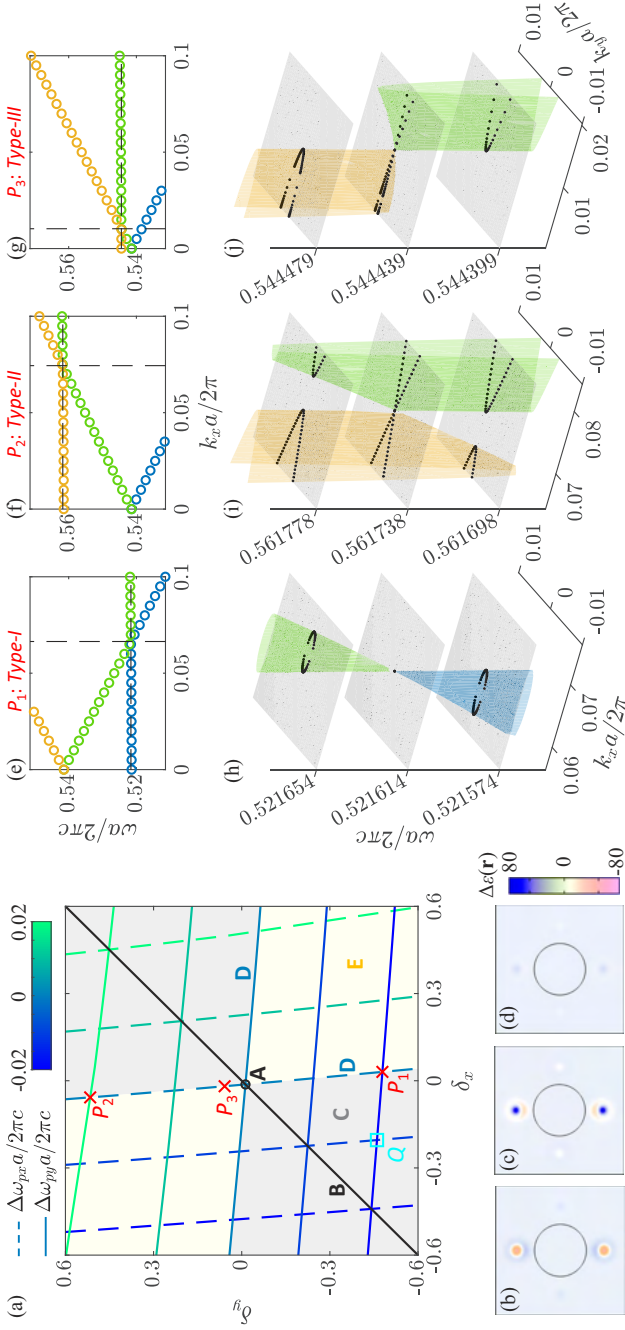
Figure 3.4: Inverse design of the deformed structures using parameters (δ_x, δ_y). (a) Contour lines of the modal separations $\Delta\omega_{px,py}$ as a function of (δ_x, δ_y). The phase diagram in (δ_x, δ_y) space represents the deformation classes A-E. Representative design points $P_1 = (0.03, -0.48)$, $P_2 = (-0.06, 0.52)$, and $P_3 = (-0.02, 0.06)$ correspond to the type-I-, type-II-, and type-III-like DPs. Design point $Q = (-0.20, -0.46)$ corresponds to another DP in relation to mirror symmetry breaking in Sec. 3.4. (b-d) Potential differences $\Delta\epsilon(\mathbf{r}) = \epsilon(\mathbf{r}) - \epsilon_0(\mathbf{r})$ inversely designed from $P_{1,2,3}$, respectively. Circles indicate the size and the position of the seed rods. (e-g) Band dispersions near the DPs with IFCs (black dots) around the DPs corresponding to $P_{1,2,3}$, respectively. (h-i) Band dispersions along the k_x-axis of PCs corresponding to $P_{1,2,3}$ and the Dirac frequencies for $P_{1,2,3}$, respectively.

38

3.4 Bandgap opening in tilted PDCs

A bandgap opening at the DPs arises from the introduction of symmetry breaking, which leads to anti-crossing of the degenerate bands, such as the inversion symmetry in a honeycomb lattice [69, 70] or a square lattice [48]. The transition from Dirac cones with linear dispersions to bandgaps with parabolic dispersions has enabled various practical applications in graphene switching devices [71] and tuning of the Purcell factors [72]. In the proposed universal platform, we investigate the realization of a bandgap opening in tilted PDCs by breaking the mirror symmetry of C_{2v}. we impose the following modification: $\delta_{x,y}(1 \pm \rho_{x,y})$ on the original perturbation for the type-III PDC (Fig. 3.5b) to obtain new mirror-symmetry-broken perturbations (Figs. 3.5a-c), where $\rho_{x,y}$ allows the mirror-asymmetric potential in the unit cell. Due to the inherent anisotropy of the tilted PDC, the response of the PDC to the mirror-symmetry-broken modification is different for each case of $\rho_x \neq 0$ and $\rho_y \neq 0$. First, for $|\text{flat}\rangle = |p_y\rangle$ and $|\pm\rangle = c_s |s\rangle \pm c_{px} |p_x\rangle$ with arbitrary coefficients c_s and c_{px}, the y-directional symmetry breaking ($\rho_y \neq 0$) for the original PDC (Fig. 3.5e) derives the anti-crossing on the k_x-axis (Fig. 3.5f) through the coupling between $|p_y\rangle$ and $|s\rangle$ of each band, leading to the bandgap opening. However, the x-directional symmetry breaking almost preserves the original PDC (Fig. 3.5d) due to the conservation of the orthogonality between $|p_y\rangle$ and $|s\rangle$ (or $|p_x\rangle$) (see Appendix A.6 for derivation).

3.5 Discussion

To summarize, we successfully designed all types of tilted PDCs in a single platform of a square-lattice photonic crystal by developing Hamiltonian-based analysis in view of the inversely designed spectral ordering. Specifically, we first classified the deformed band structures of the triply degenerate PDC and then verified the inverse-design method for the complete and deterministic design of optical structures. Through this process, the design of type-I, type-II, and type-III PDCs on the k_x-axis was achieved by exploiting
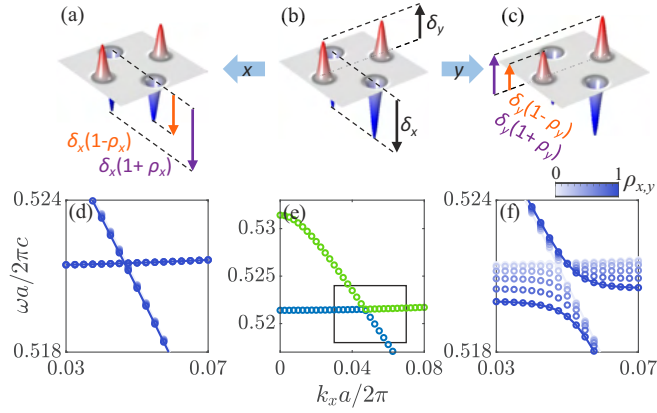
Figure 3.5: Mirror symmetry breaking of PDCs. (a-c) The profiles of mirror-symmetry-broken perturbations: (a,c) perturbation functions $f(\mathbf{r})$ obtained with the asymmetry parameters ρ_x or ρ_y for the mirror symmetry breaking of (b) the original C_{2v}-symmetric perturbation function $f(\mathbf{r})$. (d-f) Corresponding dispersion relations of the lowest two bands for (a-c): (d,f) the variations of the dispersion relations with gradual increases in $\rho_{x,y} \leq 1$, from (e) the dispersion relations for the perturbation point Q in Fig. 3.4a. The rectangle in (e) shows the magnified range for (d,f).

the nonzero slope of the flat band, achieving a tunable topological transition in the k-space. The effect of mirror symmetry breaking in relation to bandgap opening was also addressed for prospective applications. By extending our proposal to non-Hermitian systems of larger design freedom [58, 59], we expect the realization of and transition between different types of Fermi arcs in a single platform. Likewise, by exploiting time-reversal symmetry breaking, our approach should be applicable to the design of a tilted PDC with extreme nonreciprocity at the Γ-point, which derives the unidirectional material phase transition around the zero index.

Chapter 4

Engineered Scattering Responses in Spatial Domain

Resolving spatial and temporal complexities in wave-matter interactions is essential for controlling the light behavior inside disordered and nonstationary systems and therefore achieving high capacity devices. Although these complexities have usually been studied separately, a few examples exploiting both degrees of freedom have derived intriguing phenomena such as hyper-transport in evolving disorder and topological phenomena in synthetic dimensions.

In this chapter, I introduce a published work [16] by coauthors (Seungkyun Park, Prof. Sunkyu Yu, and Prof. Namkyoo Park) with permission (©John Wiley & Sons) on engineering of active disorder—disordered structures with external modulation—by employing deep neural networks. We develop a functional regressor and a material evaluator that enable inverse design of active disorder with target wave responses and evaluation of disordered structures according to the wave response controllability, respectively. By machine engineering deep-subwavelength disorder including a phase change material, We reveal functional disorder for light, which leads to angle-selective or broadband digital switching. We also develop a generative configuration of the neural network utilizing a single wave metric, which develops a family of disordered structures with independent engineering of multiple wave properties, in contrast to the traditional engineering of disorder with a specific order metric. Our approach establishes real-

ization of reconfigurable devices by exploiting the spatiotemporal complexity in wave mechanics.

4.1 Introduction

Understanding active systems—systems with signal flows dynamically tunable through interactions with their environments—is one of the important challenges for developing digital or analogue signal processing [73,74] and examining the complexity of dynamic systems [75, 76]. The deterministic design of an active system is much more intricate than that of a passive system because the relationship between a system alteration and the following signal modulation is usually nonlinear [77], even chaotic [78], or abrupt [79]. In wave mechanics, the evolution of multifaceted wave degrees of freedom (frequency, canonical and angular momenta, and topology), even with a linear system modulation, is known to be generally nonlinear except for in the regime of small perturbations [80]. Furthermore, precise prediction or tailoring of active functionalities in wave-matter interactions becomes even more challenging with material or structural complexity, as shown in light flows in a disordered structure [3, 5]. For example, the design of material perturbations for wave localization at a target position still remains a challenge, although landscape theory describes the extended boundary for the spatial emergence of localization [81, 82]. In this context, the development of a deterministic method that allows handling of correlated and vast numbers of degrees of freedom in active systems is strongly desired.

Recent advances in deep learning that have been applied to natural language processing [83], computer vision [84], and regression [85] have also been extended to physics problems, such as classical [86, 87] and quantum mechanics [88–90], fluid dynamics [91], and photonics [92–108]. In these fields, the major focus is on the extraction of the relationship between signals and systems [92–94]: the inference of signal flows in a given system operating as instantaneous numerical solving of govern-

ing equations [91, 95] or the construction of a system for a given signal flow operating as an inverse design process [96–108]. These data-driven approaches provide salient advantages over traditional numerical assessments in terms of extracting the nonlinear relationship between large system degrees of freedom by employing numerous synaptic parameters and neural activations in a deep neural network (DNN). However, the current approaches in this field still lack deep insights into active wave-matter interactions. For example, deterministic control of the system robustness or precise design of target functionalities in dynamic disordered systems have not been explored due to the inherent difficulty of resolving entangled material and dynamic complexities in wave-matter interactions.

In this chapter, we show DNN-based engineering of active disorder for digital photonics. Employing the analogy between disordered materials and complex networks [3] and inspired by a study on target control of networks [75], we investigate the disordered structure with a target activation region for modulation. The relationship between disorder landscapes and actively controlled and tunable angular transmittances is then analyzed with a functional regressor and a material evaluator, which are composed of tandem DNN structures [90, 96–98]. This DNN analysis enables deterministic design of digital functional devices: angle-selective or broadband switching of light. By machine learning the relationship between an order metric and the controllability of angular responses, we suggest a wave-response-based classification of active disorder, which subdivides the vague regimes in traditional, material-based classifications [4, 21]. Our results provide a solution for handling the complex interactions among spatial disorder, dynamic modulations, and wave responses, leading to extended design freedom for digital photonics.

4.2   Model definition

As an example of active light-matter interactions in a potential landscape of an arbitrary layout, we focus on the angular scattering response of a one-dimensional (1D) disordered platform with an active layer. With large degrees of freedom for disorder, the statistical relationship between disordered patterns and wave localization includes both bulk and interface interference effects [109] violating effective medium theory (EMT), which hinder the deterministic design of a 1D film even for the passive angular response. The problem becomes even more complex when active modulation alters the interference inside the system. Considering critical applications of this platform, including transparent displays [110], organic light-emitting diodes (OLEDs) [111], and spatial light modulators (SLMs) [112], we employ DNNs [113] for dual-spectral optimization to address this problem.
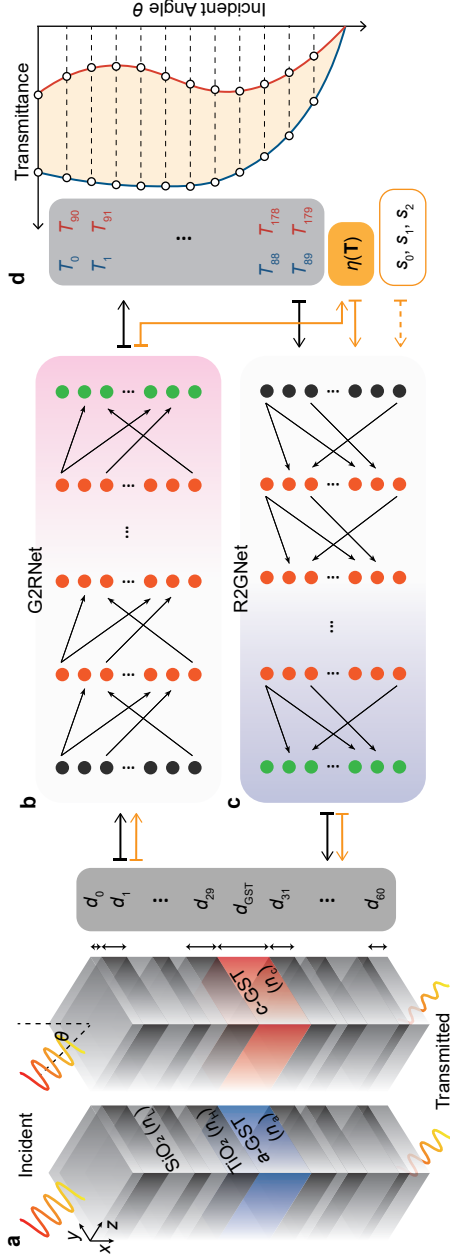
Figure 4.1: Active disorder and its DNN analysis. (a) Sixty-one-layer (SiO$_2$/TiO$_2$) film including the core GST layer with interchangeable phases (a-GST, c-GST). (b, c) Schematics of the fully connected (b) forward (G2RNet) and (c) backward (R2GNet) DNNs, mapping the (a) geometrical data $\mathbf{d} = [d_0, d_1, \cdots, d_{60}]$ and (d) optical-response data $\mathbf{T} = \left[\mathbf{T}^{(a)}, \mathbf{T}^{(c)} \right]$. d_l is the thickness of the lth layer ($0 \leq l < 61$), with $d_{30} = d_{\text{GST}}$ and d_l ($l \neq 30$) has a value between 2 nm and 198 nm, while the GST layer thickness is fixed at $d_{30} = d_{\text{GST}} = 1\mu m$. The structure is illuminated with a TE-polarized incident wave at angle θ. The refractive indices of each medium are $n_{\text{L}} = 1.43$ and $n_{\text{H}} = 2.39$ for SiO$_2$ and TiO$_2$, respectively [7, 8], and $n_{\text{a}} = 3.96$ and $n_{\text{c}} = 5.88$ for a-GST and c-GST, respectively [9]. Tm is measured in the range of $0 \leq \theta < \pi/2$ for both GST phases (a-GST, $0 \leq m < 90$; c-GST, $90 \leq m < 180$). Black, orange, and green neurons represent input, hidden, and output layers, respectively. $\eta(\mathbf{T})$ is the controllability of the optical transmittances. The prediction and inverse design from the controllability with η are depicted by yellow arrows instead of black arrows. $\mathbf{s} = [s_0, s_1, s_2]$ is the auxiliary random seed input discussed later.

45

As an example platform, we consider a SiO_2-TiO_2 multilayer disordered structure with the core layer substituted by the phase change material $Ge_2Sb_2Te_5$ (GST). The detailed structure is shown in Fig. 4.1a with its layer thicknesses $\mathbf{d} = [d_0, d_1, \cdots, d_{60}]$. Under transverse electric (TE)-polarized incidence of wavelength $\lambda_0 = 2500$nm, we examine the active control of the optical angular transmittance through the disordered structure by employing the phase change of the GST material (a-GST and c-GST for amorphous and crystalline phases, respectively [114]) in the core layer. The wave response of active disorder is quantified in the form of dual angular spectra for each GST phase: $\mathbf{T} = \left[\mathbf{T}^{(a)}, \mathbf{T}^{(c)} \right]$, where the components of each vector $T_m^{(a,c)}$ are the transmittances at a discretized incident angle between $0°$ and $90°$ (Fig. 4.1d). The main problem then becomes the extraction of the relationship between a set of structural parameters $\mathbf{d}$ and the dual-spectral angular responses $\mathbf{T}$ while the GST layer provides a fixed modulation to the disordered platform. The data for the DNNs are obtained through the transfer matrix method (TMM) as ground truth (see Appendix D.3).

4.3   DNN as a functional regressor

One of the major hurdles in the DNN inference of the relationship between light and matter is the one-to-many correspondence between a wave response and photonic structures. This issue is critical not only in guaranteeing stability during the DNN training but also in covering a wider design space in the inverse design of photonic structures from the target optical response. In resolving the one-to-many correspondence in deep-learning photonics, two related methodologies have been proposed according to the covered range of the design space [93]. Firstly, by using pre-trained DNNs for the inference of wave behaviors, the construction of the tandem inverse-design networks [90, 96–98] or the secondary learning of input photonic structures [107] have been proposed. With stable and efficient learning of DNNs, those methods allow for the coverage of a part of the complete design space. On the other hand, more complex

46

network architecture with intensive training processes have also been studied to extract multiple branches of the photonic structures for the target optical response, as demonstrated with mixture-density DNNs [105, 106], multi-branch DNNs [108], and deep generative models [99–101]. In this Section, to efficiently find a photonic structure for the target active functionality, we employ the tandem network with pre-trained forward DNNs [96].

For this goal, we construct fully connected DNNs mapping the structural parameter space to the angular response space (Geometry-to-Response, G2RNet) and vice versa (Response-to-Geometry, R2GNet; see Appendices B.1 and B.2 for details of the DNNs). We first train G2RNet for the prediction of optical responses by employing randomly generated structures and their TMM-calculated responses as input and output datasets, respectively. The cost function for the ON-OFF dual-spectral optimization is defined by the mean squared error (MSE) loss over $\mathbf{T}$:

$$L = \frac{1}{180} \sum_{m=0}^{179} \left| \hat{T}_m - T_m \right|^2, \tag{4.1}$$

where $\hat{T}_m$ and T_m are the G2RNet-predicted and ground-truth transmittances, respectively. The G2RNet-based prediction allows for higher computation speed and therefore handling of huge datasets (total of 2×10^6 realizations).

We employ the pretrained G2RNet to obtain expected optical responses from the geometry output of R2GNet. The MSE cost function that compares these responses with TMM-calculated optical responses then allows stable optimization of R2GNet, resolving the one-to-many correspondence issue between an optical response and the geometry [90, 96]. After the training, we can extract the inversely designed realization d_l at the intermediate layer of cascaded R2GNet-G2RNet for a given target response.

After training the G2RNet and R2GNet, we verify the results with the test dataset. Same as the training dataset (see Appendix B.2), the test set is also partitioned into the subclasses I-IV according to the maximum allowed value of dl (Table 1). As shown in
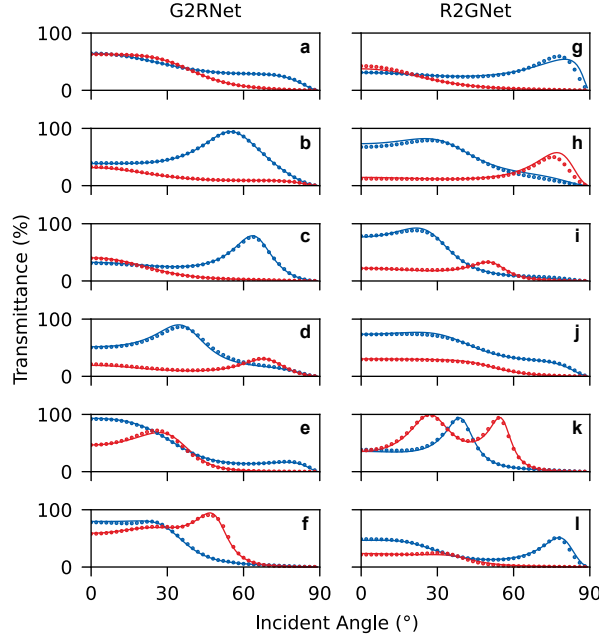
Figure 4.2: Inference by trained DNNs: (a-f) G2RNet and (g-l) R2GNet. Each realization of the (a,g) subclass I, (b,h) subclass II, (c,i) subclass III, (d,j) subclass IV, (e,k) subclass V, and (f,l) subclass VI. The solid lines and symbols denote the ground truth and DNN results, respectively. Red and blue color denote the responses for a-GST and c-GST phases.

Table 1, both DNNs provide the excellent agreements with the ground truth, achieving the MSE $\sim 5.69 \times 10^{-4}$ for the G2RNet and 1.69×10^{-3} for the R2GNet (see Figures 2a-f for each subclass realization of the G2RNet and Figures 2g-l for each subclass realization of the R2GNet).

We demonstrate two examples of target active functionalities defined for the angular response. Both examples correspond to data-driven extraction of the nonlinear relationship between the sets of $\sim 10^2$ variables (**d** and **T**), which include the interferences of multiple scatterings altered by the GST phase transition. The first example is active control of highly selective angular filtering, which is a critical functionality for SLMs, holography, and privacy films. We model the selectivity of target responses

48

with the Lorentzian line shape:

$$T^{(\mathrm{a,c})}(\theta) = \left[1 + 4\left(\frac{\theta - \theta_{(\mathrm{a,c})}}{\theta_{\mathrm{FWHM}}}\right)\right]^{-1} \tag{4.2}$$

where $T^{(\mathrm{a})}$ and $T^{(\mathrm{c})}$) correspond to the angular transmittances for the a-GST and c-GST phases with angular peaks $\theta_{\mathrm{a}} = 30°$ and $\theta_{\mathrm{c}} = 60°$, respectively, and $\theta_{\mathrm{FWHM}} = 12°$ defines the angular selectivity with the full width at half maximum (FWHM, Fig. 4.3a).

The trained DNNs successfully lead to the target angle-selective filter and its digital switching operation with the designed structural parameters (Fig. 4.3b). The TMM-calculated "true" responses (symbols in Fig. 4.3a) and the 2D TMM simulation (Fig. 4.3c,d) verify that the designed realization operates well for active tuning between a- and c-GST phases; for point-source-like incidence, only a narrow range of angular components is transmitted near the target angle ($30°$ and $60°$ for a- and c-GST). Notably, R2GNet provides systematic inverse design of active switching, in sharp contrast to previous approaches [115–118]: analytical methods [115, 116] that are restricted to the approximation of simplified platforms or heuristic approaches with numerical methods [117, 118] that are separately developed for each specific platform. We emphasize that this deterministic handling of active responses is enabled by the ON-OFF dual-spectral optimization of G2RNet and R2GNet.

The second example is a counterpart of the first one in terms of spectral richness:

Table 4.1: MSEs of the G2RNet and R2GNet for test datasets

Data set	# Samples	d_l range (nm)	G2RNet (10^{-4})	R2GNet (10^{-4})
I	833	(2, 98)	1.54	15.15
II	833	(2, 118)	2.38	39.30
III	834	(2, 138)	2.63	12.33
IV	834	(2, 158)	4.57	10.44
V	833	(2, 178)	7.25	11.06
VI	833	(2, 198)	15.77	13.07
Overall	5,000	(2, 198)	5.69	16.89
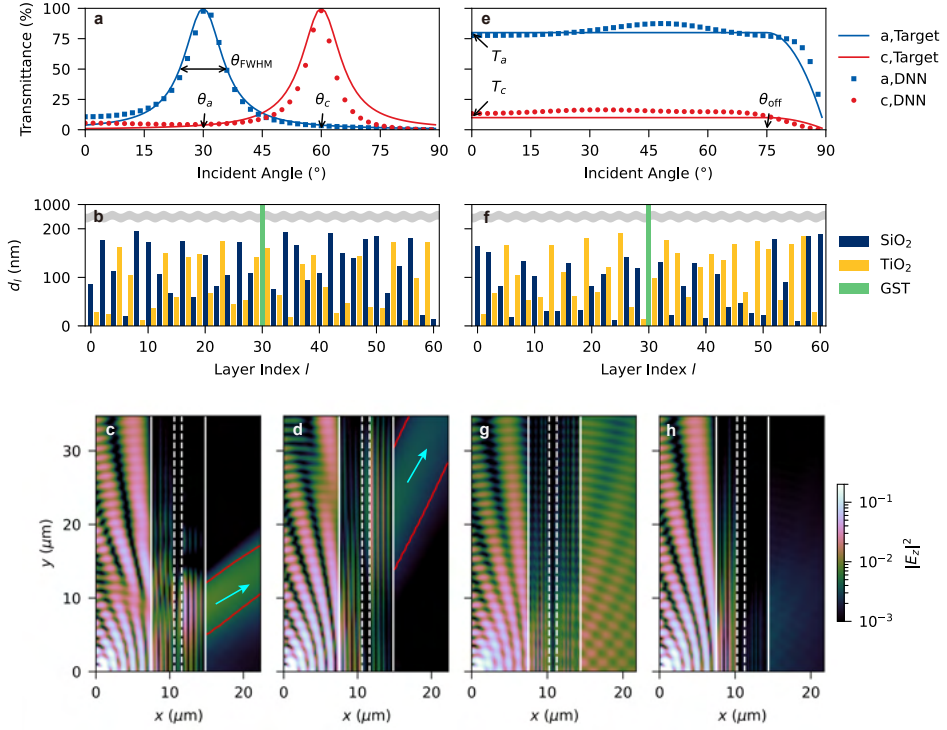
Figure 4.3: DNN functional regressor. (a-d) Angle-selective and (e-h) broadband active switching devices. (a,e) Target responses (solid lines) and DNN results (symbols, marked every 2°) for active responses of both functionalities: blue and red for *a*-GST and *c*-GST responses, respectively. $\theta_{a,c}$: target angles for selective transparency, θFWHM: target broadening, $T_{a,c}$: target transmission levels, and θ_{off}: cutoff angle. (b,f) Corresponding disordered structures (navy, yellow, and green bars for SiO_2, TiO_2, and GST layers, respectively) inversely designed from the target responses by R2GNet. (c,d,g,h) 2D intensity profiles $|E_z|^2$ for both phases of designed devices: (c,g) *a*-GST and (d,h) *c*-GST. The red lines in (c,d) indicate the contour for the half maximum of the intensity in the transmission part.

full broadband switching with an extreme modulation depth, which enables switching between completely transparent and opaque films independent of incident angle. The

target transmission response is modelled by the flat function with high θ suppression:

$$T^{(\mathrm{a,c})}(\theta) = \begin{cases} T_{\mathrm{a,c}}, & \theta < \theta_{\mathrm{off}} \\ \frac{T_{\mathrm{a,c}}(90°-\theta)(\theta-2\theta_{\mathrm{off}}+90°)}{(90°-\theta_{\mathrm{off}})^2}, & \theta \geq \theta_{\mathrm{off}} \end{cases} \tag{4.3}$$

where $T_{\mathrm{a}} = 0.85$ and $T_{\mathrm{c}} = 0.1$ are the target transmittance levels for the *a*-GST and *c*-GST phases, respectively, and $\theta_{\mathrm{off}} = 75°$ denotes the assigned cutoff angle for physical validity near the angular limit $\theta \to 90°$. Using R2GNet, we achieve the target response (Fig. 4.3e) with the designed parameters (Fig. 4.3f), leading to nearly complete transparency and opaqueness for the point-source-like incidence (Figs. 4.3g,h and Appendix B.3 for details). While this functionality is a critical feature for transparent displays and tunable backlight in liquid crystal displays, it is unachievable in crystals with inherent anisotropy and in uncorrelated disordered systems with suppressed transport but is enabled by machine engineering of disordered platforms. We conduct extended analysis for the comparison of the TMM results with the results from the finite element method (see Appendix B.4) and for the regressor model performance for different performance metrics and target parameters (see Appendix B.5).

4.4 DNN as a material evaluator

Having achieved inverse design of the platform for dynamic designer responses, we further extend our study to reveal the mechanism underlying light-matter interactions in machine-engineered active disorder, for example, the introduction of a family of disorder classified by its controllability. Despite recent efforts to classify disordered materials [4], such classifications according to various order metrics usually do not fully guarantee the expected wave properties and a successful inverse design procedure due to the nonlinear relationship between structural information and multiple interrelated wave properties [3]. Notably, in terms of active devices, such properties need to include the responsivity to active modulation, for example, the dynamic change in wave properties

51

induced by the modulation of disordered materials. For this purpose, we introduce a single parameter that enables the measuring of wave properties related to active modulation, the "controllability metric":

$$\eta \equiv \left[\frac{1}{90} \sum_{m=0}^{89} \left| T_m^{(a)} - T_m^{(c)} \right| \right]^{-1} \tag{4.4}$$

which is the wave counterpart of an order metric for disordered materials. This controllability metric η quantifies the efficiency in controlling the transmittance through a sample according to the material transition between the GST states: $\eta = 0$ for perfectly modulation-immune platforms and $\eta = 1$ for the complete transition between omnidirectional transparent and opaque states. As a bridge to traditional studies on disordered materials [4], we then try to examine the relationship between a proper order metric and the controllability metric η as a criterion for the evaluation of the degree of disorder in terms of its active wave properties.

Because the method employed in Sec. 4.3 allows only the coverage of a part of the entire design space, it is necessary to expand the covered design space in order to statistically examine the material properties of a family of disordered structures for a given η. For this purpose, we modify the DNN in Fig. 4.1 to have 1 informative and 3 auxiliary inputs instead of using the multidimensional space for the discretized angular responses T. First, a single controllability metric η is employed as the output for the modified G2RNet (mG2RNet) and the input for the modified R2GNet (mR2GNet), as shown in Figs. 4.1b,c (yellow arrows). Most importantly, we newly introduce the three-dimensional seed $\mathbf{s} = [s_0, s_1, s_2]$ as an auxiliary input for the mR2GNet, where each s_{0-2} has a random value between 0 and 1 with a uniform random distribution. We conduct mR2GNet training using expected optical responses obtained from mG2RNet, following the same process as in Fig. 4.1. When successfully training the mR2GNet with ground-truth responses (η for $\mathbf{d}$) and random seeds ($\mathbf{s}$), the network constructs the one-to-one correspondence between ($\eta, \mathbf{s}$) and $\mathbf{d}$, which naturally leads to the
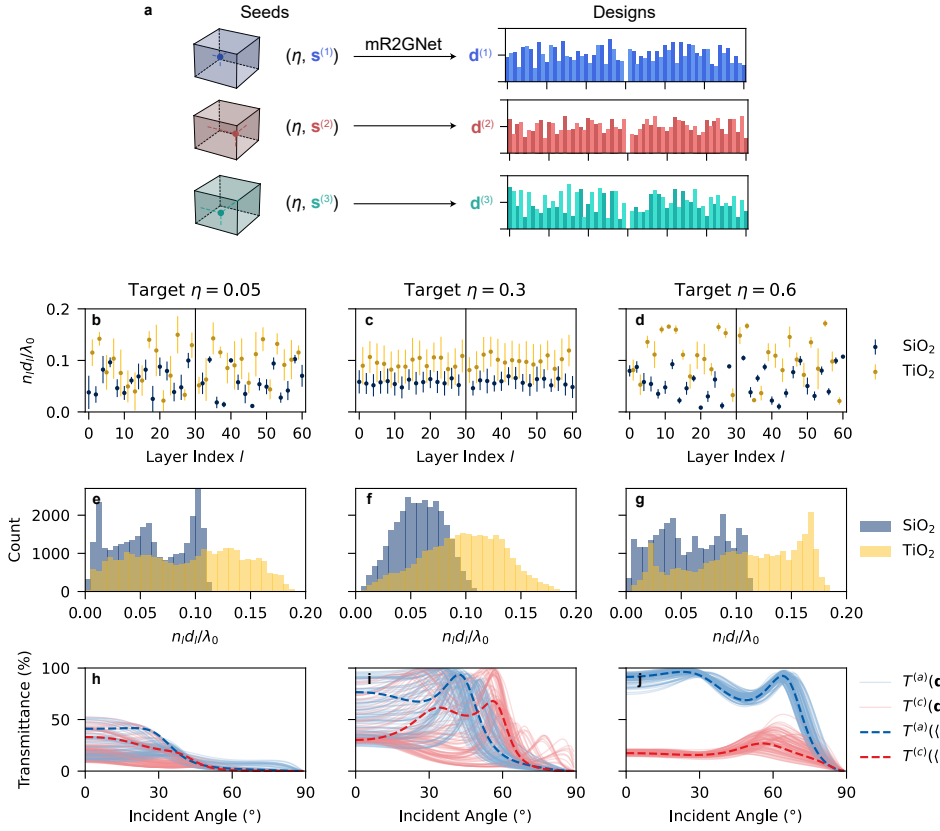
Figure 4.4: DNN material evaluator. (a) A schematic of the function of the mR2GNet expanding the design space. The multiple outputs $\mathbf{d}^{(n)}$ having the identical target controllability η are obtained through the mR2GNet with different random seeds $\mathbf{s}^{(n)}$, which is selected from the space (colored boxes) with the uniform random distribution. (b-j) Inverse design examples with target controllability metrics. (b-d) Ensemble distributions of optical phase evolution $n_l d_l$ in each layer of the designed structures. (e-g) Statistical distributions of optical phase evolution $n_l d_l$. (h-j) Corresponding angular responses for different GST phases (solid lines, blue for a-GST and red for c-GST), and ensemble-averaged results from the averaged structural parameters $\langle d \rangle$ (dashed lines). (b,e,h) $\eta = 0.05$; (c,f,i) $\eta = 0.3$; (d,g,j) $\eta = 0.6$. We plot an ensemble of 1,000 realizations for (b-g) and an ensemble of 100 realizations for (h-j) for visibility. All other parameters are the same as those in Fig. 4.3.

one-to-many correspondence between η and d due to diverse values of s (Fig. 4.4a). Therefore, as similar to multi-branch DNNs [108] or deep generative models [99–101], the suggested mR2GNet allows the extraction of multiple branches of the photonic structures for the target controllability η, which realizes a family of active disorder for a given η. Notably, when compared with multi-branch DNNs [108], our approach is especially proper to the problems in disordered photonics, because the continuous profile of s is proper to handle disordered materials, which are quantified by continuous perturbation values, not by quantized values. In Appendix B.6, we study the evolution of the structural statistics and η accuracy with the trained mR2GNet, which demonstrates the physical validity of mR2GNet in terms of continuous phase transition in the range of $0.05 \leq \eta \leq 0.6$.

Figs. 4.4b-j show an example of generating a family of active disorder: the ensembles of three different controllability metrics $\eta = 0.05, 0.3$, and 0.6, which are obtained with multiple combinations of random seeds (see Appendix B.6 for the validity of the material evaluator). Although we can assume hypothetically infinite pairs (a- and c-GST) of angular transmittances for a given η, mR2GNet filters the subsets of physically allowed optical responses with the structural variety of a family of active disorder (Figs. 4.4b-d). Notably, each material phase defined by η supports distinctive statistics for both structural (Figs. 4.4e-g) and optical (Figs. 4.4h-j) realizations. We further study the field profiles and perform a comparison with EMT (see Appendix B.7), showing that mR2GNet enables efficient inverse design in the deep-subwavelength regime that violates EMT.

We examine the structural and wave properties of active disorder in different regimes, clarifying the uniqueness of each regime. In line with the broad angular responses (Figs. 4.4h,j), robust ($\eta = 0.05$, Fig. 4.4b) or sensitive ($\eta = 0.6$, Fig. 4.4d) active disorder possesses more randomized structures than intermediate disorder ($\eta = 0.3$, Fig. 4.4c). Although highly randomized structures (Figs. 4.4b,d) and their statistics (Figs. 4.4e,g) appear similar at a glance, the DNN-based design of distinctive

patterns results in completely contrasting wave dynamics: the "hiding" of the GST core layer (Fig. 4.4h) or almost "omnidirectional" switching (Fig. 4.4j) by disordered multilayer claddings. As shown by each error bar height in Figs. 4.4b-d, the realization number of physically acceptable high-controllability responses ($\eta = 0.6$, Fig. 4.4d) is limited compared to that of low-controllability cases (Figs. 4.4b,c) because the possible spectra for high η are inevitably limited.

In the intermediate regime (Fig. 4.4c), the structures are close to the deformation of a crystalline profile rather than to uncorrelated disorder, possessing Gaussian-like structural statistics with narrow deviations (Fig. 4.4f). This set of structures leads to various candidates for an angle-selective switching operation (Fig. 4.4i), which is in line with previous studies on the relationship between crystals and their narrow angular responses [?]. Overall, the demonstrated grouping of various candidates of disorder by η provides a novel material evaluation based on wave responses.

4.5   Engineered active disorder

Compared with the traditional view on disordered photonics—classifying disordered structures based on order metrics and then examining the wave behaviors in each class of disorder—our data-driven approach in Fig. 4.4 provides a distinctive viewpoint on light-disorder interactions, which originates from the classification of "wave behavior". To characterize the wave behavior, we utilize two parameters: the angle-averaged transmittance and the controllability metric η, which evaluate the average and modulation depth of the transparency of a sample, respectively. The structural property of a material is quantified by the translational order metric τ defined in Refs [4, 21], which tends to increase from $\tau = 0$ to $\tau = \tau_c$ when the material microstructure changes from uncorrelated disorder to crystalline order (see the B.8 for the definition of τ and the setting of τ_c).

Fig. 4.5a shows the 3D plot of the relationship among T_{avg}, τ, and η obtained from

the inverse design with a given η. The extension of the design space in the mR2GNet is demonstrated allows for the handling of the order metric τ from 0 to $\sim 0.5\tau_c$, achieving the one-to-many correspondence between a wave property (η) and material profiles (τ). The result also clarifies the evolution of the average transparency and its tunability with respect to the degree of disorder. As predicted in Fig. 4.4 and per the traditional understanding of the relationship between angular responses and disorder strength [119], highly tunable ($\eta \sim 0.6$) or highly robust ($\eta \sim 0.0$) structures that possess broadband responses (Figs. 4.4c,i) are obtained with strong disorder ($\tau \sim 0$).

Furthermore, more intriguing phenomena are observed in the intermediate regime: $\eta \sim 0.3$, which includes the angle-selective digital switching platforms in Fig. 4.3a. In this regime, there are large degrees of freedom in the transparency T_{avg} because there could exist multiple pairs of ON-OFF angular profiles with the same tunability. Even at almost the same T_{avg}, a number of disorder realizations are therefore obtained with different values of τ. The DNN-based design in this case then discovers a new grouping of disordered structures not by structural metrics but by similar optical responses. This result also confirms that the traditional method for designing disorder—the inverse design of materials from τ—cannot pave a direct route to wave responses such as η or T_{avg}. In this context, our application of DNNs provides a clue to resolving the multidimensional complexity in the field of "engineered disorder" [3].

Successfully classifying disordered structures by their controllability η, a natural question then arises in terms of the inverse design process: "can we control other wave or matter quantities while preserving the target optical response (here, η)?", which is a core concept of engineered disorder [3]. The key parameter for this question is assessed with the 3D random seed input $\mathbf{s} = [s_0, s_1, s_2]$ to the mR2GNet. Each s generates a specific realization of an ensemble of disordered structures, which constitute a group of materials classified by η. For this group of materials, we examine the effect of the seed s on the other optical response (T_{avg}) and order metric (τ) to bridge the machine learning classification and traditional theory of disordered photonics.
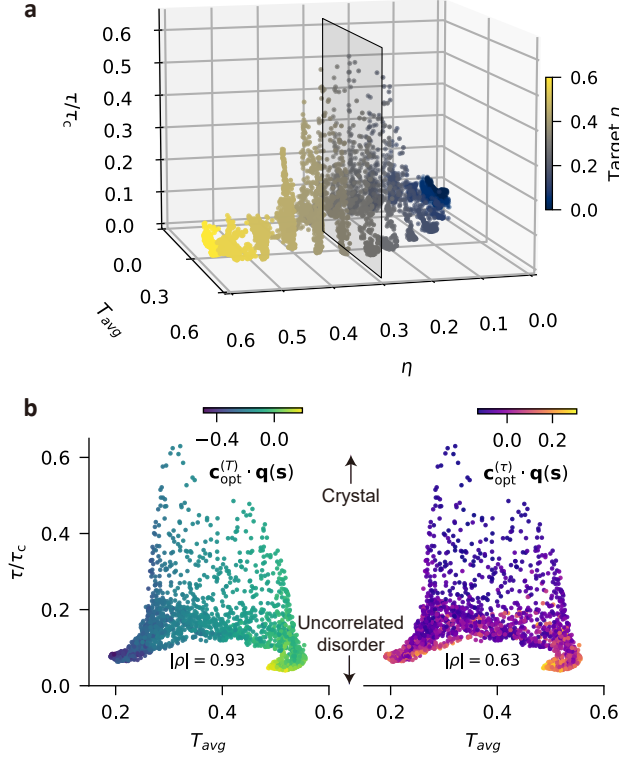
Figure 4.5: Engineered active disorder. (a) Distribution of the designed realizations in the 3D parameter space defined by the angle-averaged transmittance T_{avg}, translational order metric τ, and obtained controllability metric η. The target controllability η is represented by gradual colours. (b) 2D (T_{avg}, τ) projections of the data points with the target $\eta = 0.3$ (the transparent window in a). Left and right panels are coloured for differently optimized functions of random seeds: $\mathbf{c}_{\mathrm{opt}}^{(T)} \cdot \mathbf{q}(\mathbf{s})$ and $\mathbf{c}_{\mathrm{opt}}^{(\tau)} \cdot \mathbf{q}(\mathbf{s})$ with respect to T_{avg} and τ, respectively. All other parameters are the same as those in Fig. 4.3.

Considering $0 \le s_r \le 1$ for $r = 0, 1, 2$, we examine the influence of $\mathbf{s}$ up to its second-order contributions by defining $\mathbf{q}(\mathbf{s}) = \left[s_0, s_1, s_2, s_0 s_1, s_1 s_2, s_2 s_0, s_0^2, s_1^2, s_2^2 \right]$. If we can derive the relationship $X \approx \mathbf{c}^{(X)} \cdot \mathbf{q}(\mathbf{s})$ for a given η, where $X = T_{\mathrm{avg}}$ or τ, then deterministic handling of optical (T_{avg}) or structural (τ) responses will be allowed by obtaining a group of $\mathbf{s}$ from $X \approx \mathbf{c}^{(X)} \cdot \mathbf{q}(\mathbf{s})$. Focusing on the case of $\eta = 0.3$, we therefore optimize $\mathbf{c}^{(X)} = \mathbf{c}_{\mathrm{opt}}^{(X)}$ with an ensemble of the results from mR2GNet (Fig.

4.5a) to maximize the correlation between $f(\mathbf{s}; \mathbf{c}) = \mathbf{c}^{(X)} \cdot \mathbf{q}(\mathbf{s})$ and X (see Appendix B.9 for details of the optimization). Notably, $\mathbf{c}_{\text{opt}}^{(X)}$ describes the contribution of each element of $\mathbf{q}(\mathbf{s})$ to the mR2GNet inference of T_{avg} or τ.

Figs. 4.5b,c show the maps of the optimized representation $f(\mathbf{s}; \mathbf{c}) = \mathbf{c}^{(X)} \cdot \mathbf{q}(\mathbf{s})$ for $X = T_{\text{avg}}$ and $X = \tau$, providing strong positive (Fig. 4.5b) or negative (Fig. 4.5c) correlations of T_{avg} or τ with $f(\mathbf{s}; \mathbf{c} = \mathbf{c}_{\text{opt}}^{(X)})$, respectively. The optimized correlations $\rho_{f,T}$ and $\rho_{f,\tau}$ between the function f and the engineered responses have absolute values up to 0.93 and 0.63, respectively, leading to excellent matching to wave (T_{avg}) and matter (τ) quantities. We note that even a linear representation with $\mathbf{q}(\mathbf{s}) = [s_0, s_1, s_2]$ provides a reasonable approximation of these quantities (see Appendix B.9), demonstrating the distinct contribution of $\mathbf{s}$ elements to each wave/matter response from the mR2GNet design.

4.6 Discussion

To summarize, we employed the strength of machine learning approaches in the engineering of active disorder. Two different configurations of DNNs are applied to realize a specific disordered platform and a family of disordered structures. First, we demonstrated inverse design of disorder with a target functionality for an angular transmittance example. The results include practical applications such as angle-selective and broadband switching devices. Second, the evaluation and engineering of the degree of disorder in terms of controllability was demonstrated using the DNNs with random seeds. This approach based on a single target parameter (here, the controllability metric) discovers a family of disordered structures that allows independent control of multiple wave properties.

We note that the evaluation of active disorder according to the controllability provides a novel viewpoint on understanding the microstructures of materials in terms of wave responses. The classes of materials defined by different values of η, which had

been included in the same class for the traditional order metric τ, provide significantly distinct active responses. As shown in the large-η design, the responses include global control of the entire system with a local manipulation (here, the GST layer) analogous to the hub modulation in scale-free networks [120]. From this viewpoint, the small-η design robust to GST modulation corresponds to disconnection of the links to the GST layer through destructive interference.

Our machine learning inverse design provides clear advantages in terms of handling spatial and temporal complexities compared with previous design strategies. For example, although numerous studies have been performed on 1D disorder in the context of diagonal [121] and off-diagonal [122] disorder, crystalline [123] or disordered [109] subwavelength structures, and correlated disorder [124, 125], all of these works have employed stationary structures, lacking active control of optical responses. Previous studies on active photonic devices have also been restricted to the modulation of ordered structures of small perturbations [126–129].

In addition to intriguing works in deep-learning photonics, including the design of nanostructures [94, 95, 101], metamaterials [97, 99, 100] and metasurfaces [103], holography [102], our study on active photonic functionalities in disordered platforms will provide additional degrees of freedom in the application of deep-learning to light-matter interactions, paving the way to the handling of spatially-complex and dynamical systems. Although we examined one of the optical responses as an example—angular transmittance—the versatile features of the DNNs will enable engineering of not only the other responses (spectral responses, angular momenta, topology) but also their mixtures: the design of active disorder in the intermediate regime [3], temporal disorder [130], and disordered topological phenomena [79]. As shown in the analogy between GST-controlled disorder and target control of complex networks [75], our machine learning strategy can also be extended to other fields beyond wave mechanics, such as the interpretation and design of evolving complex networks.

Chapter 5

Engineered Scattering Responses in Time Domain

The temporal degree of freedom in photonics has been a recent research hotspot due to its analogy with spatial axes, causality, and open-system characteristics. In particular, the temporal analogs of photonic crystals have stimulated the design of momentum gaps and their extension to topological and non-Hermitian photonics. Although recent studies have also revealed the effect of broken discrete time-translational symmetry in view of the temporal analogy of spatial Anderson localization, the broad intermediate regime between time order and time uncorrelated disorder has not been examined.

In this chapter, I introduce the preprint version of a work [17] by coauthors (Dayeong Lee, Prof. Sunkyu Yu, and Prof. Namkyoo Park): investigating the inverse design of photonic time disorder to achieve optical functionalities in spatially homogeneous platforms. By developing the structure factor and order metric using causal Green's functions for the domain of time disorder, we demonstrate an engineered time scatterer, which provides unidirectional scattering with controlled scattering amplitudes. We also reveal that the order-to-disorder transition in the time domain allows for the manipulation of scattering bandwidths, which inspires resonance-free temporal color filtering. Our work will pave the way for advancing optical functionalities without spatial patterning.

5.1 Introduction

Associating temporal and spatial axes has enriched the perspective on manipulating wave phenomena. Owing to the space-time analogy between the electromagnetic paraxial equation and the Schrödinger equation, the temporal axis can be considered an alternative or auxiliary axis to the spatial dimension. This similarity between temporal and spatial axes has established the fields of quantum-optical analogy [131], non-Hermitian [132], topological [133, 134], and supersymmetric [135, 136] photonics, and universal linear optics [137]. On the other hand, the uniqueness of a temporal axis has also been a recent research focus for achieving distinct design freedom [6, 138] from spatial ones, such as the control of translational, rotational, or mirror symmetries. For example, the broken time-translational symmetry results in dynamical wave responses, which require the open-system configurations: energy or matter exchange with the system environment. In this context, dynamical wave devices with optical nonlinearity [139, 140] or non-Markovian processes [141] require the design strategy to appropriately break the time-translational symmetry. Furthermore, causality leads to unique scattering distinct from its spatial counterpart, completely blocking backscattering along the temporal axis [23].

Recent studies utilizing temporal degrees of freedom have thus focused on exploiting similarities and differences between temporal and spatial axes. The discrete time-translational symmetry in photonic temporal crystals (PTCs) [142, 143] has been examined as a temporal analogy of photonic crystals, revealing the unique phenomena along the temporal axis, such as momentum bandgaps and the localized temporal peak due to the Zak phase. The concept of disordered photonics has also been extended to the temporal axis, such as observing the statistical amplification and the scaling of Anderson localization in uncorrelated disorder [130, 144]. Various wave physics, such as amplification and lasing [145, 146], effective medium theory [147], Snell's law [23], spectral funneling [148], supersymmetry [149], parity-time symme-

try [150], nonreciprocity [151], and metamaterials [152–155], have also revealed the unique features and applications of the temporal axis inspired by its spatial counterparts. Nonetheless, these intriguing achievements cover only the partial regimes in microstructural statistics of temporal modulations, such as order with conserved symmetries [142,143,145,146,149,150,156] and their breaking with finite defects [23,151] or perturbations without any correlations [130, 144]. When considering abundant degrees of freedom in material microstructures [3], further attention to the intermediate regime between order and uncorrelated disorder for the temporal axis is mandatory.

In this chapter, we propose the concept of engineered time disorder, which allows for the designed manipulation of light scattering. Starting from the theoretical framework foranalyzingg spatial disorder, we build its temporal analog by incorporating causality in the time axis, which allows for examining the relationship between the time structure factor, time-translational order metric, and wave scattering. We demonstrate that the molding of the structure factor enables the completely independent engineering of forward and backward scattering. By investigating the order-to-disorder transition in the temporal modulation of the system, we also enable bandwidth engineering of unidirectional scatterings, such as time disorder for broadband scattering and resonance-free color filtering. Our result verifies the spatial-pattern-free design of conventional optical functionalities and represents a great advantage of time disorder in bandwidth engineering with respect to temporal crystals.

5.2   Temporal scattering

Consider a nonmagnetic, isotropic, and spatially homogeneous optical material having the time-modulated relative permittivity $\epsilon(t)$. For the x-polarized planewave of the displacement field $\mathbf{D}(\mathbf{r}, t) = \hat{\mathbf{x}}\psi(t)e^{ikz}$, where k is the wavenumber, the governing equation is6,14,16:

$$\left[\frac{\mathrm{d}^2}{\mathrm{d}t^2} + \frac{c^2 k^2}{\epsilon(t)}\right]\psi(t) = 0 \tag{5.1}$$

where c is the speed of light. Because k is conserved according to the spatial translational symmetry, Eq. (5.1) is the temporal analogy of the one-dimensional (1D) Helmholtz equation for spatially varying materials, exhibiting space-time duality28 by imposing the role of the optical potential on $[\epsilon(t)]^{-1}$. To investigate the regime of weak scattering, we express the real-valued optical potential as $\alpha(t) \equiv \epsilon^{-1}(t) = \alpha_{\mathrm{b}}[1 + \Delta\alpha(t)]$, where α_{b} is the potential at $t \to \pm\infty$. With the assumption of weak perturbation during a finite temporal range, the time-varying component $\alpha_{\mathrm{b}}\Delta\alpha(t)$ becomes analogous to the weakly perturbed permittivity in spatial-domain problems1. Notably, as those time-varying systems are open systems, the energy provided by the environment $P_{\mathrm{in}}(t) = \mathrm{d}u_{\mathrm{EM}}^0/\mathrm{d}t$ results in the nonconservative EM field energy14,16 $u_{\mathrm{EM}}^0(t) = [\mathbf{E}^*(t) \cdot \mathbf{D}(t) + \mathbf{H}^*(t) \cdot \mathbf{B}(t)]/4$.

For a given temporal variation of the system, we employ the harmonic incidence $\psi_{\mathrm{inc}}(t) = \exp\left(-i\omega_{\mathrm{b}}t\right)$, where $\omega_{\mathrm{b}} = \alpha_{\mathrm{b}}^{1/2}kc$ is the optical (incident) frequency at $t \to \pm\infty$ for a wavelength of interest $\lambda_0 = 2\pi/k$. Under the first-order Born approximation [157] with $|\Delta\alpha(t)| \ll 1$, the time-domain scattering field $\psi_{\mathrm{sca}}(t)$ becomes:

$$\psi_{\mathrm{sca}} \approx -\omega_{\mathrm{b}}^2 \int_{-\infty}^{\infty} dt' \Delta\alpha(t')\psi_{\mathrm{inc}}(t')G(t;t') \qquad (5.2)$$

where $G(t;t')$ is the Green's function for the impulse response of the temporal delta function scatterer $\delta(t - t')$ (see Appendix C.1).

Although Eq. (5.2) is identical to the 1D scattering problem in the spatial domain31, the uniqueness of the time-varying material is in selecting the mathematical form of the Green's function among several candidates: the Feynman, retarded, and advanced propagators [158]. Due to the unidirectional flow of time, the temporal Green's function satisfies causality: $G(t;t') = 0$ for $t < t'$. To fulfil the temporal boundary conditions for the displacement field and magnetic field [6, 142] at $t = t'$, the analytical form of the retarded Green's function for the temporal impulse becomes (Fig. 5.1a, see also
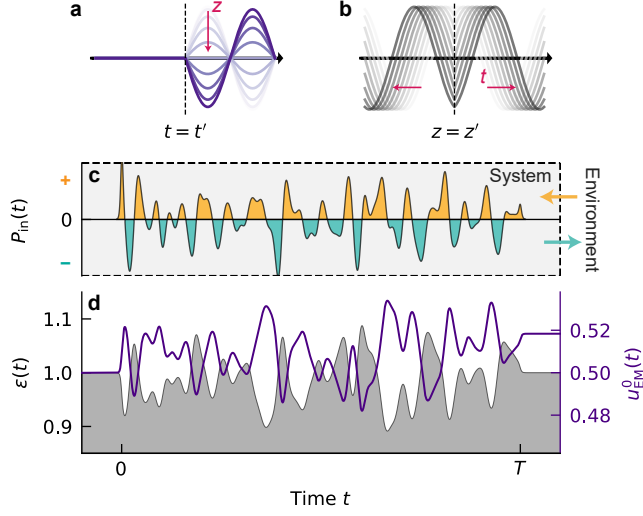
Figure 5.1: Concept of temporal scattering as open-system responses. (a,b) Schematics of temporal and spatial Green's functions: (a) $\mathrm{Re}\left[G(t;t')e^{+ikz}\right]$ and (b) $\mathrm{Re}\left[G(z;z')e^{-i\omega t}\right]$. Shaded lines in (a,b) indicate the evolution of each Green's function. (c) Schematic of system modulation by signal power $P_{\mathrm{in}}(t)$ from the environment, representing the system gain and loss for positive and negative P_{in}, respectively. (d) Energy alteration from light-matter interactions with the time disorder driven by $P_{\mathrm{in}}(t)$ in (c). $\epsilon(t)$ (grey area) and $u^0_{\mathrm{EM}}(t)$ (purple line) are the time-varying permittivity confined inside the temporal range $[0, T]$ and the instantaneous electromagnetic energy density, respectively.

Appendix C.2):

$$G(t;t') = \frac{1}{\omega_{\mathrm{b}}} \sin\left[\omega_{\mathrm{b}}(t - t')\right]\Theta(t - t'), \tag{5.3}$$

where $\Theta(t - t')$ is the Heaviside step function of $\Theta(t > 0) = 1$ and $\Theta(t \leq 0) = 0$ (see Appendix C.3 for numerical validitation of the Born approximation). The Green's function in Eq. (5.3) can be separated into $G(t;t') = G_{\mathrm{FW}}(t;t') + G_{\mathrm{BW}}(t;t')$ for $G_{\mathrm{FW,BW}}(t;t') = \pm \exp\left[\pm i\omega_{\mathrm{b}}(t - t')\right]\Theta(t - t')/(2i\omega_{\mathrm{b}})$, where each sign of $\pm\omega_{\mathrm{b}}$ determines the propagation direction with the conserved k.

We emphasize that causality imposes the uniqueness on the temporal Green's

function, i.e., the coexistence of the forward (or transmitted) and backward (or reflected) waves in $t > t'$ (Fig. 5.1a). Such a mathematical form of $G(t; t')$ is in sharp contrast to the spatial Green's function $G(z; z') \sim \exp\left(ik|z - z'|\right)$, which exhibits the separate existence of the forward ($e^{+ik(z-z')}$) and backward ($e^{-ik(z-z')}$) waves in $z > z'$ and $z \leq z'$, respectively (Fig. 5.1b). This uniqueness emphasizes the open-system nature of time-varying systems, despite the fact that the governing equation of Eq. (5.1) is mathematically analogous to the spatial one. When an external modulation to the system is applied by a time-varying signal power Pin (Fig. 5.1c), the unique form of the causal Green's function in a time-varying system—interfering forward and backward basis (Fig. 5.1a)—breaks the conservation of the electromagnetic energy inside the system (Fig. 5.1d). In this context, the independent control of forward and backward scattering in temporally random heterogeneous materials compels a design strategy distinct from their spatial counterparts.

From Eqs. (5.2) and (5.3), the scattering field becomes (see Appendix C.1):

$$\psi_{\text{sca}}(t) = \frac{\omega}{2i}\left[e^{-i\omega_b t}\int_{-\infty}^{\infty}dt'\Delta\alpha(t') - e^{+i\omega_b t}\int_{-\infty}^{\infty}dt' e^{-2i\omega_b t'}\Delta\alpha(t')\right]. \qquad (5.4)$$

Although the thermodynamic limit is an ideal criterion to characterize the statistical features of wave-matter interactions in disordered systems [159], the nonconservative optical energy (Fig. 5.1d) may cause unphysical results, such as the divergence of the energy in momentum gaps [130, 143]. Therefore, we assume a finite-range temporal variation $\Delta\alpha(t)$ with $\Delta\alpha(t < 0) = \Delta\alpha(t > T) = 0$ in examining Eq. (5.4). We also employ the ergodic hypothesis, i.e., the statistical equivalence between the average over all realizations and the average over one statistically homogeneous realization, where a correlation depends only on the time difference, at the thermodynamic limit [159]. The ergodicity allows for the homogeneous correlation function $\hat{C}(t_1, t_2) \equiv \langle\Delta\alpha^*(t_1)\Delta\alpha(t_2)\rangle = C(\Delta t)$ for $0 \leq t_{1,2} \leq T$ and $\Delta t = t_1 - t_2$, where $\langle\cdot\rangle$ denotes the ensemble average. We separate the ensemble-averaged scattering power after the temporal perturbation ($t > T$) into the forward ($\langle\text{PFW}\rangle$) and backward ($\langle\text{PBW}\rangle$) waves

(see Appendix C.1) as:

$$\langle P_{\mathrm{FW}} \rangle = \frac{\omega_{\mathrm{b}}^2}{4} \int_0^T dt_1' \int_0^T dt_2' C(t_1' - t_2'),$$

$$\langle P_{\mathrm{BW}} \rangle = \frac{\omega_{\mathrm{b}}^2}{4} \int_0^T dt_1' \int_0^T dt_2' C(t_1' - t_2') e^{2i\omega_{\mathrm{b}}(t_1' - t_2')}. \tag{5.5}$$

With a sufficiently broad temporal range, each power approaches the Fourier transform of $C(\Delta t)$ ($S(\omega) = \mathcal{F}[C(\Delta t)]$ where $\mathcal{F}$ denotes the Fourier transform. Also, see Appendix C.1), as follows:

$$\langle P_{\mathrm{FW}} \rangle \approx \frac{\omega_{\mathrm{b}}^2 T}{4} S(0), \quad \langle P_{\mathrm{BW}} \rangle \approx \frac{\omega_{\mathrm{b}}^2 T}{4} S(2\omega_{\mathrm{b}}) \tag{5.6}$$

where we define $S(\omega)$ as the "time structure factor" governing scattering from temporal disorder, i.e., the temporal counterpart of the static structure factor [4, 159]. It is worth mentioning that $S(\omega)$ is the power spectral density of the signal that determines the time-varying perturbation of an optical potential. While Eq. (5.6) allows for engineering forward and backward scatterings, we note that the condition of suppressing the forward wave $\langle P_{\mathrm{FW}} \rangle \approx 0$ directly corresponds to the time-domain realization of the concept of hyperuniformity [3–5, 160–164], as $S(\omega \to 0) \sim 0$. It is worth mentioning that although time-domain hyperuniformity has been observed in soft matter physics, such as the 144 avalanche size of the Oslo model [165], to our knowledge, the corresponding phenomena and their engineering in wave physics have still been missing.

Therefore, engineering the power flows $P_{\mathrm{FW,BW}}$ using time disorder is achieved by moulding $S(\omega)$ near $\omega = 0$ and $2\omega_{\mathrm{b}}$. Notably, in the design of $S(\omega)$, three conditions should hold for $C(\Delta t)$ and $S(\omega)$: the Hermiticity $C(\Delta t) = C^*(-\Delta t)$ with real-valued $S(\omega)$, $|\mathrm{Re}\,[C(\Delta t)]| \leq C(\Delta t = 0)$ from the maximum of the correlation function, and $S(\omega) \geq 0$ from the autocorrelation theorem (see Appendix C.4). We also note that we set $\langle \Delta \alpha(t) \rangle = 0$ to remove insuppressible scattering at the zero frequency limit [4] $S(\omega = 0)$, which is the necessary condition to freely engineer the forward scattering

power P_{FW}.

To establish the designed manipulation of light through photonic time disorder, we demonstrate the engineering of time disorder: unidirectional scattering for the independent control of $\langle P_{\mathrm{FW}} \rangle$ and $\langle P_{\mathrm{BW}} \rangle$, order-to-disorder transition for spectral manipulation, and momentum-selective spectral shaping. We note that there are two different classes of one-to-many correspondence between a scattering response and the realizations of disorder. First, because scattering phenomena are governed by $S(0)$ and $S(2\omega_{\mathrm{b}})$ for a planewave of ω_{b}, a family of time disorder can be achieved by altering the overall shape of $S(\omega)$ while preserving $S(0)$ and $S(2\omega_{\mathrm{b}})$. Second, even for the same $S(\omega)$, there is an infinite number of realizations of time disorder because the entire landscape is uniquely determined by all the orders of correlation functions [159]. Therefore, to rigorously study the relationship between scattering and disorder, a number of different realizations with a given $S(\omega)$ should be examined. In the following discussion, we focus on the first origin in examining a family of disorder, also conducting the statistical analysis due to the second origin.

5.3   Unidirectional scattering

We demonstrate the unidirectional scattering achieved by suppressing $S(0)$ or $S(2\omega_{\mathrm{b}})$. We set a time and frequency scale $t_0 = \lambda_0/c = 2\pi/\omega_0$, and assume the incident frequency $\omega_{\mathrm{b}} = \omega_0$, where the ambient potential is assumed as $\alpha_{\mathrm{b}} = 1$. We set the structure factor functions $S_{\mathrm{FW}}(\omega)$ and $S_{\mathrm{BW}}(\omega)$ for the forward and backward scatterings, which are designed in the frequency ranges $[-2\omega_0, 2\omega_0]$ and $[-3\omega_0, 3\omega_0]$, respectively, and zero elsewhere. The structure factors $S_{\mathrm{FW,BW}}(\omega)$ in this scenario are modulated by the design parameters $S_0 = S_{\mathrm{FW}}(\omega)$ and $S_{2\omega} = S_{\mathrm{BW}}(2\omega_{\mathrm{b}})$, respectively, while satisfying the continuity and C^1 smoothness as well as the statistical bounds for $\epsilon(t)$ (see Appendix C.5).

Fig. 5.2a shows the designed $S_{\mathrm{FW}}(\omega)$ and $S_{\mathrm{BW}}(\omega)$ for different values of S_0 and

$S_{2\omega}$, respectively. With the corresponding $C(\Delta t)$ from $S_{\text{FW,BW}}(\omega)$, we generate a set of $\epsilon(t)$ realizations through the multivariate Gaussian process (see Appendices C.4 and C.6). Three example realizations are depicted in Fig. 5.2b for the suppressions of (i) both forward and backward (case A), (ii) backward only (case B), and (iii) forward only (case D), which have the corresponding time structure factor shown in Fig. 5.2a.

For each case, an ensemble of 10^4 realizations is generated, and their scattering responses are examined using the time-domain transfer matrix method (TD-TMM) [144, 166]. Figs. 5.2c, d show that the ensemble average of the rigorous TMM results (error bars) provides good agreement with the $S(\omega)$-based prediction with the Born approximation (lines). Engineering temporal modulation using the time structure factor allows for completely independent manipulation of temporal scattering: unidirectional scattering only with forward (case B) or backward (case D) propagations or scattering-free temporal variations (cases A and C).
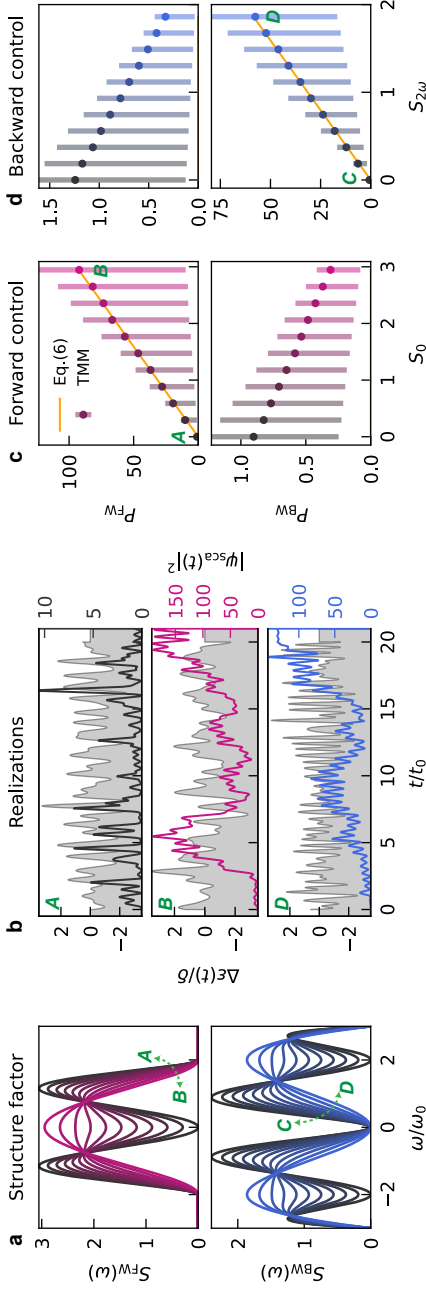
Figure 5.2: Engineering unidirectional scattering. (a) Structure factors $S_{FW}(\omega)$ (top) and $S_{BW}(\omega)$ (bottom) with varying design parameters S_0 and $S_{2\omega}$, respectively. The design parameters are represented by gradual colours (A: $S_0 = 0$, B: $S_0 \sim 2.95$, C: $S_{2\omega} = 0$, and D: $S_{2\omega} \sim 1.86$). b, An example of the $\Delta\epsilon(t)$ realizations (grey areas) and the corresponding scattering intensity $|\psi_{sca}(t)|^2$ (solid lines) for the A, B, and D states in (a). $t_0 = 2\pi/\omega_0 = \lambda_0/c$. (c,d) Comparison of the scattering powers from the structure factor prediction (solid lines) and rigorous TD-TMM (error bars) for each ensemble (10^4 realizations) with different design parameters S_0 and $S_{2\omega}$ in (a,b): the suppression of the (c) backward and (d) forward scattering. The top and bottom figures represent the forward and backward power, respectively, after $t > 20t_0$. Markers denote the ensemble average from the TD-TMM results. Error bars denote the 1st to 3rd quartiles of the ensemble. Structure factors $[S_{FW,BW}(\omega), S_{0,2\omega}]$, scattering field ($\psi_{sca}$), and scattering powers ($P_{FW,BW}$) are normalized with δ^2/ω_0, δ, and δ^2, respectively, where $\delta = [C(\Delta t = 0)]^{1/2}$.

69

5.4 Engineered time disorder for spectral manipulation

The main advantage of utilizing disordered systems in wave physics is the ability to manipulate multiple wave quantities with different sensitivities to material phases [3]. Such intricate wave-matter interactions allow for the alteration of the target wave quantity while preserving other ones, as shown in the independent manipulation of localization and spectral responses in spatial domains [109, 136]. In this context, we focus on the independent control of two wave properties—scattering and spectral responses—using photonic time disorder.

In designing temporal systems through the language of the time structure factor, ordered systems (e.g., photonic temporal crystals [143]) are depicted by a set of Bragg peaks, indicating certain harmonic frequencies at which the system interacts with an incident wave. In contrast, time disorder close to the Poisson process [161] shows a broadband structure factor that guarantees a continuum frequency response; at the extreme, the uncorrelated Poisson disorder possesses the structure factor of an infinite plateau. Using such a clear distinction between order and uncorrelated disorder and the relationship between the structure factor and scattering, we explore the intermediate regime between two extremes in photonic time disorder.

To quantify the transition between order and uncorrelated disorder, we introduce the transition parameter ξ for the structure factor $S(\omega)$: from $\xi = 0$ mimicking crystals to $\xi = 1$ for a near-Poisson case. We set the extreme case of the structure factors $S_{\text{C}}(\omega)$ and $S_{\text{P}}(\omega)$ for the crystal and near-Poisson state, respectively, defining the transition between them, as (Fig. 5.3a, see Appendix C.7)

$$S(\omega) = (1 - \xi)S_{\text{C}}(\omega) + \frac{1}{2}\left[S_{\text{P}}\left(\frac{\omega - 2\omega_0}{\xi}\right) + S_{\text{P}}\left(\frac{\omega + 2\omega_0}{\xi}\right)\right]. \qquad (5.7)$$

Fig. 5.3b shows the structure factors obtained from different mixing of $S_{\text{C}}(\omega)$ and $S_{\text{P}}(\omega)$, targeting the suppression of forward power $P_{\text{FW}} \sim 0$ with $S(\omega = 0) = 0$. As the transition from the A to D states occurs, the heights of the Bragg peaks from $S_{\text{C}}(\omega)$
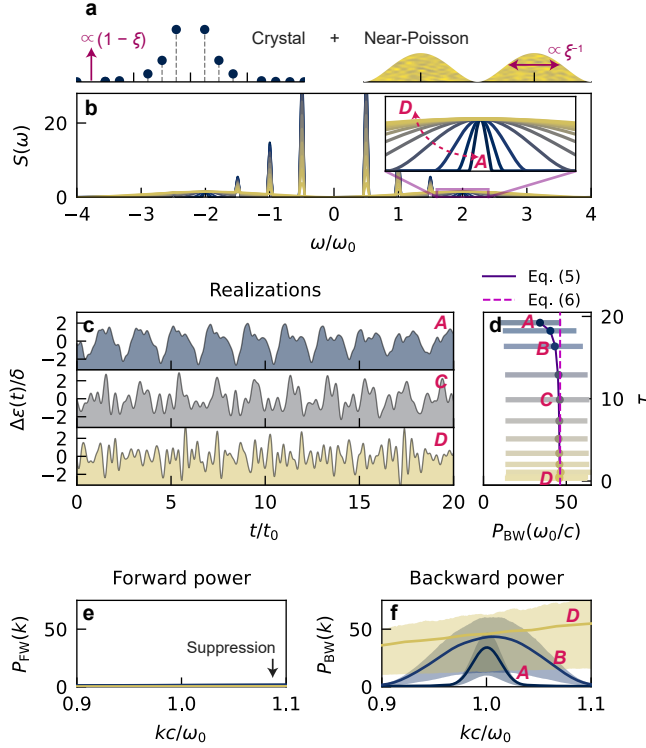
Figure 5.3: Time disorder for bandwidth engineering. (a) Schematics of the structure factors for crystalline (left) and near-Poisson disorder (right). ξ is the transition parameter between order ($\xi = 0$) and disorder ($\xi = 1$). (b) Structure factors $S(\omega)$ for the order-to-disorder transition with varying ξ: from crystalline (navy) to near Poisson (yellow). A, $\xi = 0.025$; B, $\xi = 0.1$; C, $\xi = 0.3$; D, $\xi = 1$. (c) Examples of realizations of $\Delta\epsilon(t)$ for A, C, and D. (d) Statistical relationship between the backward scattering power and the time-translational order metric τ. The scattering theory prediction (solid and dashed lines with Eqs. (5.5) and (5.6), respectively) and rigorous TD-TMM (error bars) are compared for each ensemble of 10^4 realizations. (e,f) Spectral responses of the (e) forward and (f) backward scattering powers near the target momentum ($0.9 < kc/\omega_0 < 1.1$) for A, B, and D in (d). Solid lines and coloured areas denote the ensemble averages and the 1st to 3rd quartiles, respectively. Structure factors [$S(\omega)$], order metric (τ), and scattering powers ($P_{\text{FW,BW}}$) are normalized with δ^2/ω_0, δ^4, and δ^2, respectively, where $\delta = [C(\Delta t = 0)]^{1/2}$.

at $\omega \neq 2\omega_0$ decrease, while the bumps $S_P(\omega)$ centred at $\omega = \pm 2\omega_0$ (Fig. 5.3b, inset) are continuously broadened. Eq. (5.7) allows for maintaining the integral of $S(\omega)$ over the frequency domain to restrict the average fluctuation in the time domain realizations. The designed transition therefore enables the characterization of time disorder solely depending on the "pattern" of disorder, not on the magnitude of the fluctuation.

Fig. 5.3c shows examples of the realization of time disorder for different ξ values in Fig. 5.3b, all of which are designed to derive backward scattering only. The transition parameter ξ qualitatively describes the temporal material phase transition from nearly crystalline to nearly uncorrelated disorder. To characterize each disorder more quantitatively, we introduce the time-translational order metric τ:

$$\tau = t_0^{-1} \int_{-4\omega_b}^{4\omega_b} d\omega \left| S(\omega) - \frac{\pi\delta^2}{4\omega_0} \right|^2, \tag{5.8}$$

where $\pm 4\omega_0$ denotes the range of nonzero $S(\omega)$ (see Appendix C.7). Analogous to its original definition in the spatial domain [4, 161], τ characterizes the distance of a given temporal evolution from the Poisson process, describing how much a given $\epsilon(t)$ is ordered in the time domain. As shown in Fig. 5.3d, the designed backward scattering from Eq. (5.6) and the resulting TD-TMM show good agreement, while better agreement is achieved when we leave out the infinite temporal range approximation by using Eq. (5.5).

The most significant difference between crystals and uncorrelated disorder can be found in their spectral responses. As shown in Figs. 5.3e, f, the change in material phases between order and uncorrelated disorder provides a designed manipulation of the bandwidth of temporal modulations while preserving the target scattering response: the suppression of forward scattering. Remarkably, near-Poisson time disorder (case D) guarantees almost $\pm 10\%$ range of spectrum bandwidth for the suppression of forward scattering and the constant backward scattering, improving the bandwidth 40 times compared to that of the near-crystal one (case A). Therefore, the use of randomness

in the temporal modulation enables a significant bandwidth enhancement and thus the noise-robust signal processing preserving optical functionalities.

In general, the comparison between crystals and disorders gives rise to the trivial tradeoff between efficiency and broadband properties. While the narrow and high peak in the structure factor of crystals results in high efficiency at a certain target frequency but the sensitivity in the vicinity of the frequency (i.e., narrowband response), broad bump-like structure factors of disorders show less efficient but robust (broadband) responses. In contrast, we note that the advantage of utilizing disorder for both robustness and "controlled" efficiency originates from the tradeoff within multiple peaks as shown in Fig. 5.3a: taking both robustness and efficiency at a target frequency ($\omega \sim 2\omega_0$), while losing efficiencies at the other frequencies ($\omega/\omega_0 \sim 0.5, 1, 2, 2.5, \cdots$).

5.5 Momentum-selective spectral shaping

Through Figs. 5.2 and 5.3, we demonstrate the control of the scattering directivity under monochromatic conditions and its spectral engineering through an order-to-disorder transition. Based on this result, we show a novel methodology for the filtering of light waves—temporal "resonant-less" colour filter—using a platform with spatial translational symmetry. The proposed approach is in sharp contrast to conventional platforms for light filtering, such as multilayers [167] or resonators [168].
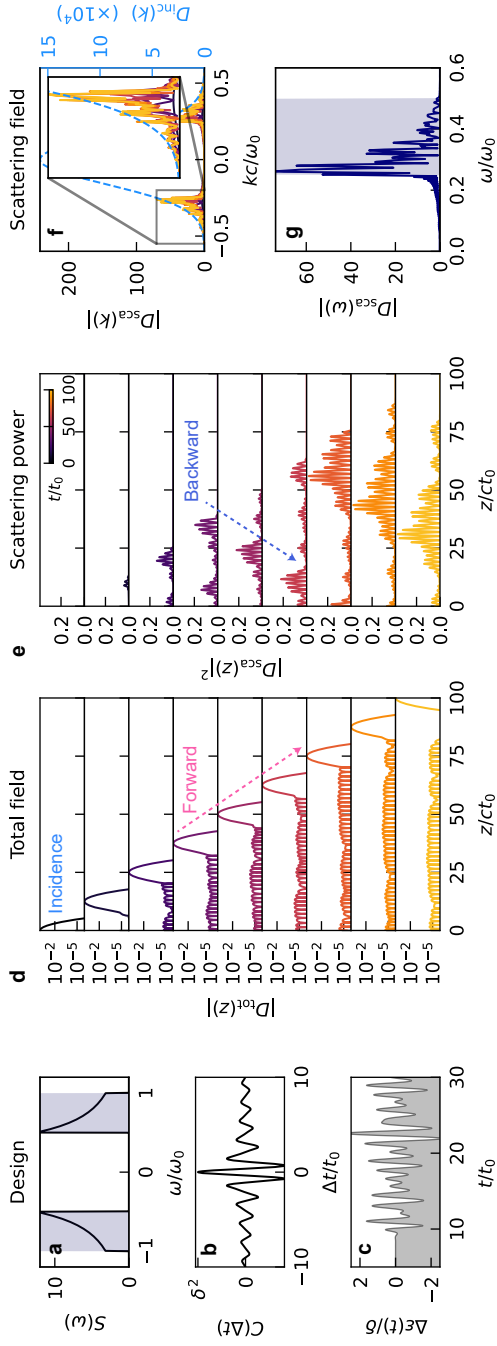
Figure 5.4: Momentum-selective scatterer. (a) Target structure factor for momentum-dependent spectral shaping of backscattering. (b,c) The corresponding (b) temporal correlation function and (c) sample realization of $\Delta\epsilon(t)$. (d,e) Time evolution of a Gaussian pulse $D_{\text{inc}}(z, t = 0) = \exp\left[-(z/\sigma_z)^2/2\right]$ undergoing a tailored temporal perturbation from $t/t_0 = 10$ to 90: (d) the total field amplitude and (e) scattering power. Arrows indicate the direction of propagation for the incident and back-reflected fields. (f,g) Spectral responses of the scattering field: (f) the time evolution of the k-space field $D_{\text{sca}}(k, t)$ and (g) the ω-domain field $D_{\text{sca}}(z = 0, \omega)$ at a fixed point. The blue dashed line in (f) denotes $D_{\text{inc}}(z, t = 0)$. The shaded area in (g) represents the filtering band $S(2ck)$. The gradual colours in (d-f) represent the time evolutions from $t = 0$ (black) to $100t_0$ (yellow). Structure factors $S(\omega)$ and fields $D_{\text{sca}}(z)$, $D_{\text{sca,inc}}(k)$, and $D_{\text{sca}}(\omega)$ are normalized with δ^2/ω_0, δ, $\delta c/\omega_0$, and δ/ω_0, respectively, where $\delta = [C(\Delta t = 0)]^{1/2}$. $\sigma_z = ct_0$ in (d-g).

74

As an example of this application, we consider the propagation of a pulse and its interaction with the designed photonic time disorder, which leads to unidirectional and bandpass scattering. Because the forward scattering is governed by $S(0)$ regardless of the light momentum k, the momentum-resolved operation for the forward scattering is prohibited. Therefore, we focus on the filtering of backward waves while suppressing forward waves, as illustrated in Fig. 5.4a, which filters out the range of "wave" momenta k by the corresponding "material" temporal frequencies $|\omega| = 2c|k| \in [\omega_{\min}, \omega_{\max}]$ $(= [\omega_0/2, \omega_0]$ in Fig. 5.4a). Notably, the nonzero lower bound $\omega_{\min}$, which imposes a stricter condition on suppressing the forward wave, comprises the temporal realization of the stealthy hyperuniformity [4, 161], as $S(|\omega| < \omega_{\min}) \sim 0$. We also set $S(\omega) \sim \omega^{-2}$ dependency in the target range to compensate for the ω^2 dependency of scattering power [Eq. (5.6)]. The temporal correlation and a sample realization of a given structure factor are shown in Figs. 5.4b, c.

The initial displacement field $D(z, t = 0)$ is a real-valued scalar function that satisfies $D(k) = D^*(-k)$. We assume a Gaussian pulse $D(z, t = 0) = \exp\left[-(z/\sigma z)^2/2\right]$. The time evolution of the field through the time disorder filter becomes

$$D(z, t) = \int_{-\infty}^{\infty} \frac{dk}{2\pi} D(k, t = 0) e^{ikz} \psi_{\text{tot}}(t; k), \tag{5.9}$$

where $\psi_{\text{tot}}(t; k)$ is the single-component response of the incident planewave $\psi_{\text{inc}}(t) = e^{-ikct}$. Snapshots of the pulse evolution are shown in Fig. 5.4d, exhibiting $+z$ propagation (pink arrow) and a scattered tail behind it.

The evolutions of scattered fields in real- and k-space are illustrated in Figs 4e and f, respectively. After the modulation, the generated backscattered field propagates along the $-z$-direction (blue arrow). Fig. 5.4f and its ω-axis representation (Fig. 5.4g) clearly demonstrate the filtering functionality, which preserves the envelope shape of the original incident pulse while suppressing the designed band stop range $ck/\omega_0 \in [-1/4, 1/4]$.

The mechanism of the suggested temporal colour filter is fundamentally distinct

from conventional optical filters, which utilize the bounded momentum responses through spatial inhomogeneity (for example, using mirrors, scatterers, or resonators) and the following constraint on spectral responses through dispersion relations. In contrast, the proposed temporal colour filter does not require spatial inhomogeneity. While the momentum of light is preserved through spatial translational symmetry, the spectral responses are filtered through broken temporal translational symmetry, which is the nature of time-varying open systems.

5.6 Discussion

Recently, several important studies have explored time disorder [130, 144], revealing the growth of the statistical intensity of waves with log-normal distributions and temporal Anderson localization, both of which are obtained with uncorrelated disorder. In contrast, the significance of our result is on bridging temporal light scattering and correlated time disorder, which allows for the deterministic engineering of scattering direction, bandwidth, and spectral shaping.

In terms of time-dependent perturbation theory, our statistical approach corresponds to a weak perturbation with the spectral transition amplitude $S(\omega)$ that gives rise to the transition from the incident (initial state, ω_{b}) to forward or backward scattering (1st-order perturbations, $\pm\omega_{\mathrm{b}}$) with the energy differences $S(\Delta\omega = -2\omega_{\mathrm{b}}, 0)$, respectively, as similar to Fermi's golden rule. Furthermore, this is consistent with a so-called time correlation function in the Green-Kubo (G-K) relationship [169, 170] to describe the transport coefficient in fluid [171] or thermal [172] systems. While the listed phenomena all share the universal linear response theory in both classical and quantum physics, the direct application of the essence of the G-K relation to temporal light scattering is demonstrated for the first time, and it serves as a toolkit for dynamical photonic systems.

Notably, time-varying wave systems can be experimentally realized through time-

varying transmission lines (TVTLs) [6, 145, 173–176] in the microwavae regime. Because transmission lines are ideal platforms for describing one-dimensional wave propagations, TVTLs with temporal modulations via loaded LC resonators or varactor diodes allow for reproducing intriguing phenomena in time-varying wave systems. For the practical implementation of our disordered systems, the TVTL is also expected to be a suitable platform, which only requires the free-form control of time-varying parameters. Notably, the realization of photonic time disorder beyond the microwave regime is a much more challenging issue. Although the unidirectional scattering with suppressed forward scattering can be realized independent upon the modulation speed ($S(0) = 0$), the engineering of backward scattering $S(2\omega_{\mathrm{b}})$ requires ultrafast modulations, which is one of the controversial topics in recent studies on photonic momentum gaps [177]. For example, to achieve the significant modulation of backward scattering in the infrared or visible range, the femtosecond modulation of optical refractive indices is necessary. All-optical modulation based on second-order [177] or third-order optical nonlinearity can be a possible mechanism. To increase the effective material perturbation in strong light-matter interactions, the use of two-dimensional materials [178], plasmonic platforms [179], or epsilon-near-zero metamaterials [180] can be a candidate platform.

To summarize, we developed the patternless realization of EM scattering in temporally disordered media. Starting from the analytical formulation of wave scattering with the time structure factor, we demonstrated the moulding of the structure factors for engineered scattering. This top-down approach enables the design of modulation signals for unidirectional scattering in spatially homogeneous systems. By examining the order-to-disorder transition in the temporal domain, we also develop bandwidth engineering while preserving unidirectional scattering, which enables the realization of resonance-free colour filters. To develop a more concrete theoretical foundation of disordered photonics in the time domain, exploring the uniqueness and criteria of photonic time disorder, such as the energy-nonconservative nature of momentum gaps with hyperuniformity [4] and stealthy [3] and its relation to the thermodynamic limit, will

be a further research topic. In terms of engineered disorder, unidirectional scattering achieved with photonic time disorder will provide extended design freedom in realizing optical nonreciprocity [181, 182]. To break Lorentz reciprocity [182], the generalization of photonic time disorder to the spatio-temporal domain will be necessary. The bandwidth engineering through order-to-disorder transition as shown in our work will then be applicable to realize broadband optical isolation.

Chapter 6

Conclusion

As presented in this Dissertation, the research focus during my Ph.D. program has been mainly on the inverse design of photonic devices in terms of functionality and active tunability, based on numerical, theoretical, and data-driven methods.

In the first part, I demonstrated how to design photonic tilted Dirac dispersions for novel anisotropic control of light flows inside photonic crystal structures. While the C_{4v}-symmetry in the original structure gives rise to the presence of accidental degeneracy at the Γ-point, the breaking of the symmetry into the reduced C_{2v}-symmetry enabled the relative shift of Γ-point eigenmode frequencies in a top-down manner, resulting in the new emergence of tilted Dirac cones apart from the Γ-point for all the types I, II, and III according to the sign of group velocities. On top of that, the further breaking of C_{2v}-symmetry by additional mirror symmetry considerations in different directions also clarified their role in dispersion crossing and anti-crossing in relation to the gap opening, which illustrates the prospective application in switching operation by asymmetric modulation.

Next, I demonstrated the inverse design of photonic active switching devices, which is mostly in accordance with the title of this Dissertation, by utilizing deep neural networks. There are two kinds of networks: first, a forward network maps structural information of design parameters into the corresponding optical responses, while a re-

verse network maps a target optical response into the possible candidate for the design solution. Constructing a tandem structure of the reverse network followed by the pretrained forward network, it was able to properly obtain one inverse-designed structure for target active responses for on/off switching. I also studied the relationship among modulation sensitivity (or, robustness) against the external modulation, conventionally defined order metric of the material structure, and the average transmittance, which provides new insight into their relationship in terms of engineered disorder.

Finally, I studied the "activeness" of the photonic active devices: the temporal features of the optical scattering phenomena driven by a time-varying optical potential. With the newly developed relationship between temporal scattering and the corresponding temporal structure factor, which quantifies the disordered state of the material phase, it was able to target-control the temporal scattering in forward and backward directions independently. Further analyzing the order-to-disorder transition in the temporal domain, the advantage of using disordered modulation rather than the periodical one in terms of bandwidth control was also verified with the demonstration of pattern-free temporal color filters without spatial resonance structure.

The above studies do independently become a building block for understanding the design degrees of freedom in active devices: as an anisotropy control unit, as a tunable directivity control unit, and as fundamentals of time-varying physics with temporal disorder and the inherent energy description, which hopefully will contribute to the advance in the design of energy-efficient and high-functionality optical devices, such as an optical processor.

Appendix A

Supplementary Information for Chapter 3

A.1 Effective wave parameter analysis

We focus on optical potentials at the parameter space point $(0.00, -0.13)$ in Fig. 3.4a, which corresponds to the deformation class D. For this potential, the eigenfrequency at Γ-point is $0.54142\pi c/a$ for s- and p_x-modes and $0.53642\pi c/a$ for p_y-mode. The dispersion of the three bands near Γ-point is shown in Fig. A.1a (2D cross-section) and Fig. A.1b (3D view), showing the directional linear dispersion toward X-axis [60] and different topologies of isofrequency contours (IFC).

Effective material parameters for a give dispersion are then calculated from the transmission and reflection for a slab structure [61]. In Fig. A.1f, the spectral dispersions of effective permittivities ϵ_z for x- (blue) and y-directional (purple) propagations are shown, which are almost the same without directionality. The permittivities have also a zero at the s-mode frequency. In contrast, in Fig. A.1g, the effective permeabilities μ_y for x-direction (blue) and μ_x for y-direction (purple) propagations have different zeros, corresponding to p_x- or p_y-mode eigenfrequencies, respectively. These results represent the different roles of s- and $p_{x,y}$-modes in the electric and magnetic responses of the medium, which correspond to an equivalent rod and ring resonator, respectively. The eigenfrequencies ω_s and $\omega_{px,py}$ are then the resonant frequencies where the complete

81
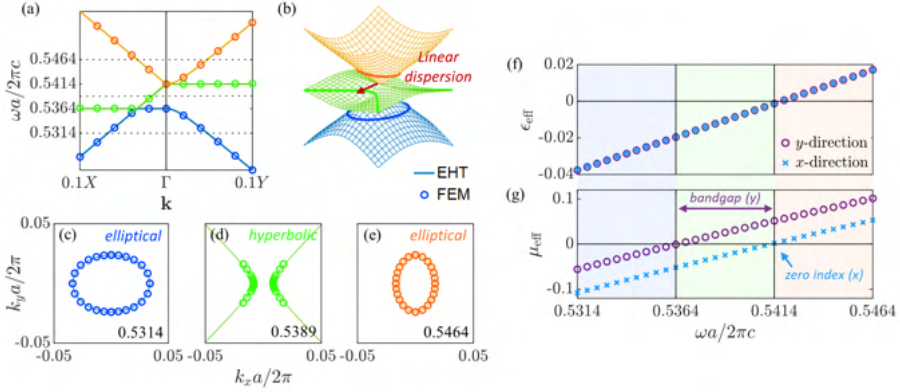
Figure A.1: (a,b) Band dispersions of the photonic crystal for the design point $(\delta_x, \delta_y) = (0.00, -0.13)$ in Fig. 3.4a, obtained by the FEM (marker) and the effective Hamiltonian theory (line). (c-e) IFCs at frequencies $\omega a/2\pi c = 0.5314$, 0.5389, and 0.5464, respectively, presented in (b) as bold lines. (f,g) Effective material parameters of the medium: (f) ϵ_z for y- (purple) and x- (blue) directional propagation, and (g) μ_x for y- (purple), μ_y for x- (blue) directional propagation.

cancellation of external field components E_z and $H_{y,x}$ occur.

Using the above wave parameter analysis, we interpret the geometry of band structures. First, the hyperbolic IFC (green bold line in Fig. A.1b) originates from the different signs of μ_x and μ_y, as shown in the region of $0.5364 < \omega a/2\pi c < 0.5414$ in Fig. A.1g. On the other hand, the elliptic IFCs (orange and blue bold lines in Fig. A.1b) originate from the same sign of μ_x and μ_y. The y-directional bandgap ($0.5364 < \omega a/2\pi c < 0.5414$) is obtained with negative $\epsilon_z \mu x$. Finally, a wave propagating in x-direction at $\omega = \omega_s = \omega_{px}$ undergoes zero refractive index with finite impedance, due to the Dirac dispersion with $\epsilon_z = \mu_y = 0$. The corresponding wave behaviors in the real space are depicted in Fig. A.2. The good agreement of wave propagations between the designed medium and the corresponding effective medium demonstrates the validity of the effective Hamiltonian approximation.
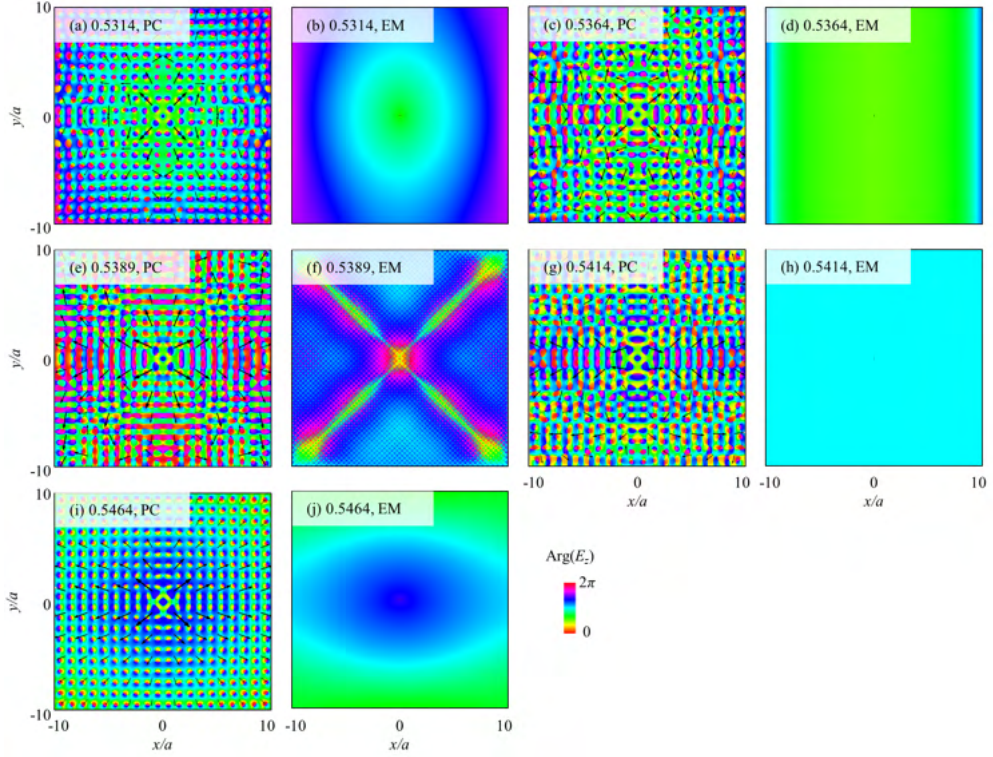
Figure A.2: Phase of E_z for the electromagnetic wave propagation from a line source at the origin for (a,c,e,g,i) the designed optical medium in Fig. A.1 and (b,d,f,h,j) the medium with the corresponding effective permittivities and permeabilities. The oscillating frequencies $\omega a/2\pi c$ are selected as (a,b) 0.5314, (c,d) 0.5364, (e,f) 0.5389, (g,h) 0.5414, and (i,j) 0.5464.

A.2 Derivation of band anti-crossing near a type-III Dirac point

The effective Hamiltonian for the deformation class D (without loss of generality, $\omega_s = \omega_{px} > \omega_{py}$) can be written using the Γ-point basis as the sum of on-axis

Hamiltonian for $k_y = 0$ and the other terms:

$$H(\mathbf{k}) = H_{\text{axis}} + V = \begin{bmatrix} \omega_s & v_x k_x & 0 \\ v_x k_x & \omega_s & 0 \\ 0 & 0 & \omega_{py} \end{bmatrix} + \begin{bmatrix} 0 & 0 & v_y k_y \\ 0 & 0 & 0 \\ v_y k_y & 0 & 0 \end{bmatrix}. \tag{A.1}$$

The unperturbed Hamiltonian H_{axis} has three eigenfrequencies $\omega_\pm(k_x) = \omega_s \pm |v_x k_x|$ and $\omega_{\text{flat}}(k_x) = \omega_{py}$ with corresponding eigenmodes $|\pm\rangle = \begin{bmatrix} 1 & \pm 1 & 0 \end{bmatrix}^T / \sqrt{2}$ and $|\text{flat}\rangle = \begin{bmatrix} 0 & 0 & 1 \end{bmatrix}^T$, which form a single intersection point between the bands of ω_- and ω_{flat}, at $k_x = k_{x0} \equiv |(\omega_s - \omega_{py})/v_x|$.

For the perturbation with nonzero k_y, the first-order degenerate perturbation theory [57] derives the matrix elements of V with regard to $|-\rangle$ and $|\text{flat}\rangle$ as

$$\langle -|V|-\rangle = \frac{v_y k_y}{2} \begin{bmatrix} 1 & -1 & 0 \end{bmatrix} \begin{bmatrix} 0 & 0 & 1 \\ 0 & 0 & 0 \\ 1 & 0 & 0 \end{bmatrix} \begin{bmatrix} 1 \\ -1 \\ 0 \end{bmatrix} = 0 \tag{A.2}$$

and $\langle \text{flat}|V|\text{flat}\rangle = 0$, $\langle -|V|\text{flat}\rangle = \langle \text{flat}|V|-\rangle = v_y k_y/\sqrt{2}$ in a similar way. Using the basis $\mathcal{W} = \{|-\rangle, |\text{flat}\rangle\}$, the perturbation is represented by

$$[V]_{\mathcal{W}} = \frac{v_y k_y}{\sqrt{2}} \begin{bmatrix} 0 & 1 \\ 1 & 0 \end{bmatrix}, \tag{A.3}$$

which splits the degenerate frequency by new eigenvectors and corresponding eigenvalues: $\omega_\uparrow = v_y k_y/\sqrt{2}$, $\omega_\downarrow = -v_y k_y/\sqrt{2}$, $|\uparrow\rangle = (|-\rangle + |\text{flat}\rangle)/\sqrt{2}$, and $|\downarrow\rangle = (|-\rangle - |\text{flat}\rangle)/\sqrt{2}$. The band anti-crossing near the DP is then given by $|\omega_\uparrow - \omega_\downarrow| = \sqrt{2}|v_y k_y|$, which originates from the coupling of the degenerate modes at the DP.

A.3   Perturbative inverse design method

We employ a C_{2v}-symmetric multiplicative perturbation function $f_0(\mathbf{r})$ with parameters (δ_x, δ_y):

$$f_0(\mathbf{r}) = \delta_x \left[\phi\left(\frac{x-d}{\sigma}, \frac{y}{\sigma} \right) + \phi\left(\frac{x+d}{\sigma}, \frac{y}{\sigma} \right) \right]$$
$$+ \delta_y \left[\phi\left(\frac{x}{\sigma}, \frac{y-d}{\sigma} \right) + \phi\left(\frac{x}{\sigma}, \frac{y+d}{\sigma} \right) \right], \tag{A.4}$$

where $d = a/3$, $\sigma = 0.035a$, and $\phi(\xi, \eta) = e^{-(\xi^2 + \eta^2)/2}$. Because our design is restricted in the finite unit cell $\mathbf{r} \in [-a/2, a/2]^2$ with periodic boundary conditions, we use a differentiable form at the boundary ($\partial f / \partial \mathbf{n} \sim 0$) by symmetrizing for the boundary:

$$f(\mathbf{r}) = \sum_{\mathbf{R}} f_0(\mathbf{r} - \mathbf{R}), \tag{A.5}$$

where $\mathbf{R} = a(n_x, n_y)$ represents a few lattice vectors for integers $n_{x,y} = 0$ or ± 1.

A.4   Dipole-based design

To demonstrate the universality of the inverse design technique, in this section, we show the inverse design based on a dipole p_x-mode. By applying the perturbation function $f(\mathbf{r})$ of the same form to the dipole-x mode profile $u_{px0}(\mathbf{r})$, we obtain a new target mode $u_{px}(\mathbf{r}) = \exp\left[f(\mathbf{r}) \right] u_{px}(\mathbf{r})$ with the parameters (δ_x, δ_y). Then, the potential for the target mode by Eq. (3) leads to the frequency shifts $\Delta\omega_{s,py} = \omega_{s,py} \breve{\ } \omega_{px}$ as a function of (δ_x, δ_y) (Fig. A.3).

When compared to Fig. 3.4a in the main text, Fig. A.3 shows that both $\Delta\omega_s$ (dashed lines) and $\Delta\omega_{py}$ (solid lines) have steep gradients for the parameters. However, the independent control of $\Delta\omega_s$ and $\Delta\omega_{py}$ is still valid, allowing the reproduction of the results from the monopole-based design.
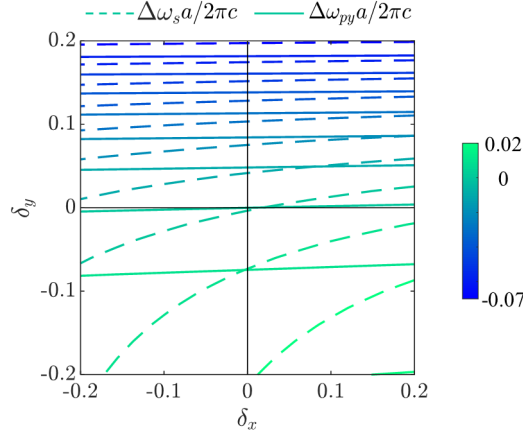
Figure A.3: Contour lines of the modal separations $\Delta\omega_{s,py}$ with the fixed p_x-mode frequency, as a function of (δ_x, δ_y). Solid (or dashed) lines denote the frequency shift of the dipole p_y (or monopole s) mode.

A.5 Practical implementation and the flat band control

In this note, we present the platform based on the photonic-molecular unit cell to achieve the practical realization of continuous potential landscapes in the main text. The structure is composed of five homogeneous dielectric rods: four identical dielectric rods ($\delta_x = \delta_y = 0$) around the center rods as shown in Fig. A.4a, which guarantees C_{4v}-symmetry and thus $\omega_p = \omega_{px} = \omega_{py}$. We apply the gradient descent method [66] as a numerical optimization process to achieve the accidental degeneracy. The frequency difference $(\omega_p - \omega_s)^2$ is set to the loss function for this numerical assessment, which is minimized with respect to the structural parameters (radii of the center and lateral rods r_0, r_1, and displacement of the lateral rods from the center d) with while maintaining the permittivity of the rods as $\epsilon_0 = \epsilon_1 = 12.5$. Using this process, we obtain a parameter set for the triple accidental degeneracy among s- and $p_{x,y}$-modes: $r_0 = 0.192a$, $r_1 = 0.059a$, and $d = 0.297a$. For the structure with optimized parameters, the degenerate frequency is determined to be $\omega_p = \omega_{px,py} = 0.515 \times 2\pi c/a$.

With the inverse design, we further impose the perturbation to the newly-obtained
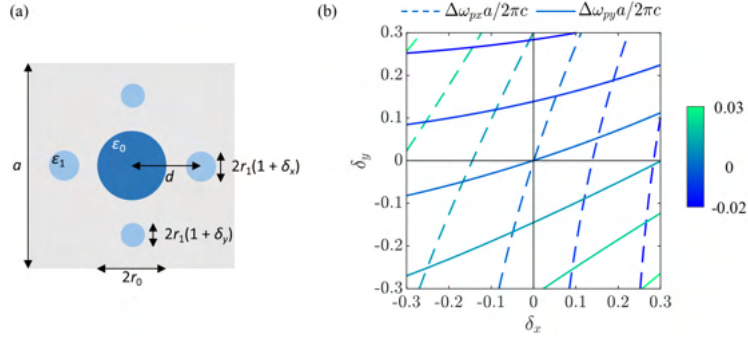
Figure A.4: (a) C_{4v}-symmetric photonic molecular unit cell with material and structural parameters: the permittivity ϵ_0 and the radius r_0 of the central rod, the permittivity ϵ_1 and the radius r_1 of the lateral rods, and the distance d between the center and lateral rods. (b) Contour lines of the modal separations $\Delta\omega_{px,py} = \omega_{px,py} - \omega_s$, as a function of radius modulation parameters (δ_x, δ_y) in (a).

structure with the accidental degeneracy, by controlling radii of the lateral rods. Controlling the parameters (δ_x, δ_y), we achieve the frequency shifts $\Delta\omega_{px,py} = \omega_{px,py} - \omega_s$ as shown in Fig. A.4b as a function of (δ_x, δ_y) of which the contour lines appear as dotted and solid lines, respectively. This photonic molecule unit cell enables the practical realization of tilted photonic Dirac cones.

In the proposed practical platform, we also investigate the control of the slope of flat bands. The effective Hamiltonian described in the main text assumes the perfectly flat band having zero group velocity. However, a real structure that follows the first principle of Maxwell's equations results in the emergence of nonzero slopes of the flat band, which originates from higher-order coupling terms [57]. Notably, the further control of the flat band slope significantly improves the design degree of freedom, achieving a clear transition between the type I and type II Dirac cones without shifting the flat band.

Fig. A.5 shows the result of controlling the slope of the flat band using structural parameters. We employed the gradient descent method to find the parameter set (r_0, r_1) shown in Fig. A.4 for accidental degeneracy with fixed parameters (d, ϵ). Figs. A.5a,b
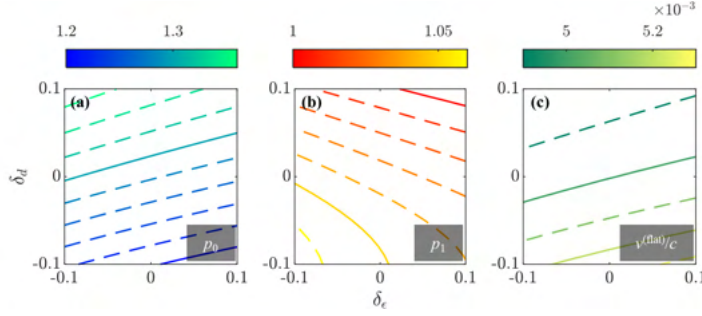
Figure A.5: (a, b) Optimized result of the parameters (radii of the center and lateral rods) $p_0 = r_0^{(\text{opt})}/r_0^{(\text{i})}$ and $p_1 = r_1^{(\text{opt})}/r_1^{(\text{i})}$ for accidental degeneracy by gradient descent method, as a function of the other fixed parameters $\delta_d = (d - a/3)/(a/3)$ and $\delta_\epsilon = (\epsilon - 12.5)/12.5$. Here the starting point for the optimization is given as $(r_0(\text{i}), r_1(\text{i})) = a(0.163, 0.058)$. (c) Intrinsic slope of the flat band defined by $v^{(\text{flat})}/c = [\omega(\mathbf{k}_s) - \omega(0)]/ck_s$, where $\mathbf{k}_s = 2\pi/a(0.1, 0)$, for the derived band structure with parameters $r_0^{(\text{opt})}$ and $r_1^{(\text{opt})}$.

show the control of the group velocity ($v^{(\text{flat})} = [\omega(\mathbf{k}_s) - \omega(0)]/k_s$, where $\mathbf{k}_s = 2\pi/a(0.1, 0)$) of the flat band while maintaining the accidental degeneracy. As shown in Fig. A.3c, the tuning range of $v^{(\text{flat})}$ is close to $\pm 4\%$ with the reasonable modulation of structural parameters up to $\delta_d = \pm 0.1$ and $_\epsilon = 0.1$. Further research on more significant change of the flat band will be a topic of future study.

A.6 Effect of mirror symmetry breaking

In this section, we examine quantitatively the effect of mirror-asymmetric function. For example, broken mirror symmetry in y-direction can be achieved by rewriting the perturbation function in Eq. (A.4) as

$$
\begin{aligned}
f_0(\mathbf{r}) =& \delta_x \left[\phi\left(\frac{x-d}{\sigma}, \frac{y}{\sigma}\right) + \phi\left(\frac{x+d}{\sigma}, \frac{y}{\sigma}\right) \right] \\
&+ \delta_y(1+\rho_y)\phi\left(\frac{x}{\sigma}, \frac{y-d}{\sigma}\right) + \delta_y(1-\rho_y)\phi\left(\frac{x}{\sigma}, \frac{y+d}{\sigma}\right)
\end{aligned}
\tag{A.6}
$$

with nonzero asymmetry parameter ρ_y. This modifies the on-axis Hamiltonian in Eq. (A.1) to

$$H_{\text{axis}} = H_{\text{axis}}^{(0)} + V_y = \left[H_{\text{axis}}^{(0)} + V_y^{(+)} \right] + V_y^{(-)} = H_{\text{axis}}' + V_y^{(-)}, \qquad \text{(A.7)}$$

where

$$H_{\text{axis}}^{(0)} = \begin{bmatrix} \omega_s^{(0)} & v_x^{(0)} k_x & 0 \\ v_x^{(0)} k_x & \omega_{px}^{(0)} & 0 \\ 0 & 0 & \omega_{py}^{(0)} \end{bmatrix} \qquad \text{(A.8)}$$

is the k_x-axis Hamiltonian when $\rho_y = 0$, V_y is the perturbation by turning on the parameter ρ_y, $V_y^{(\pm)} = (V_y \pm P_y V_y P_y)/2$ are the even $(+)$ and the odd $(-)$ part of V_y with respect to y-inversion operator P_y, satisfying $V_y^{(\pm)} P_y = \pm P_y V_y^{(\pm)}$, and

$$H_{\text{axis}}' = \begin{bmatrix} \omega_s & v_x k_x & 0 \\ v_x k_x & \omega_{px} & 0 \\ 0 & 0 & \omega_{py} \end{bmatrix} \qquad \text{(A.9)}$$

is a new k_x-axis Hamiltonian in which the even part of perturbation $V_y^{(+)}$ is taken into account for a new set of Γ-point eigenfrequencies $(\omega_s, \omega_{px}, \text{and } \omega_{py})$ and velocity coefficients (v_x, v_y). It is noted that the nonzero ρ_y cannot ensure that the perturbation is fully odd; however, the even part $V_y^{(+)}$ does not change the symmetric properties significantly because it is still C_{2v}-symmetric due to even parity in x- as well as y-direction.

The perturbation by the odd part $V_y^{(-)}$ is applied to the DP on k_x-axis, which is defined by the new Hamiltonian H_{axis}'. Without loss of generality, the DP is made up of two degenerate states $|-\rangle = c_s |s\rangle + c_{px} |p_x\rangle$ and $|\text{flat}\rangle = |p_y\rangle$ with arbitrary coefficients c_s and c_{px}. From symmetry considerations of $V_y^{(-)}$ such that $V_y^{(-)}(x, y) = +V_y^{(-)}(-x, y) = -V_y^{(-)}(x, -y)$ in the position-space representation, we obtain the

following matrix elements:

$$\langle -|V_y^{(-)}|\text{flat}\rangle = c_s^* \langle s|V_y^{(-)}|\text{flat}\rangle \neq 0 \tag{A.10}$$

due to the fact that

$$\int_{-a/2}^{a/2} u_{px}^* V_y^{(-)} u_{py} \mathrm{d}x = 0, \quad \int_{-a/2}^{a/2} u_s^* V_y^{(-)} u_{py} \mathrm{d}x(\mathrm{d}y) \neq 0, \tag{A.11}$$

while $\langle -|V_y^{(-)}|-\rangle = \langle \text{flat}|V_y^{(-)}|\text{flat}\rangle = 0$. The nonzero off-diagonal matrix element $\langle -|V_y^{(-)}|\text{flat}\rangle$ thus means the band anti-crossing even on the axis.

On the other hand, the Hamiltonian with broken x-mirror symmetry is written as

$$H_{\text{axis}} = H_{\text{axis}}^{(0)} + V_x = \left[H_{\text{axis}}^{(0)} + V_x^{(+)} \right] + V_x^{(-)} = H_{\text{axis}}' + V_x^{(-)} \tag{A.12}$$

for a modified perturbation function with nonzero ρ_x:

$$\begin{aligned}
f_0(\mathbf{r}) = & \delta_y \left[\phi\left(\frac{x}{\sigma}, \frac{y-d}{\sigma}\right) + \phi\left(\frac{x}{\sigma}, \frac{y+d}{\sigma}\right) \right] \\
& + \delta_x(1+\rho_x)\phi\left(\frac{x-d}{\sigma}, \frac{y}{\sigma}\right) + \delta_x(1-\rho_x)\phi\left(\frac{x+d}{\sigma}, \frac{y}{\sigma}\right).
\end{aligned} \tag{A.13}$$

In this case, the matrix elements are determined by

$$\langle -|V_x^{(-)}|-\rangle = 2\,\mathrm{Re}\,\langle s|V_x^{(-)}|p_x\rangle, \tag{A.14}$$

which is not necessarily zero, and $\langle \text{flat}|V_x^{(-)}|\text{flat}\rangle = \langle \text{flat}|V_x^{(-)}|-\rangle = 0$ from similar symmetry considerations with Eq. (A.11). There is a significant difference from the previous case of y-mirror symmetry breaking; the possibly nonzero matrix element in Eq. (A.14) is at the diagonal position, which just shifts the band ω_- but does not lead to the coupling between the two bands. Therefore, they still maintain the "crossing" state. The FEM calculations in Figs. 3.5d, f verify this result.

Appendix B

Supplementary Information for Chapter 4

B.1 DNN Parameters

G2RNet is composed of an input layer (61 neurons), 10 hidden layers (180 neurons for each layer, which are all batch-normalized [183] and activated by the GELU function [184]), and an output layer (180 neurons, which are batch-normalized and activated by the sigmoid function for bounded wave response values). Similarly, R2GNet is composed of an input layer (180 neurons), 6 hidden layers (120 neurons for each layer, which are all batch-normalized and activated by the GELU function), and an output layer (60 neurons, which are batch-normalized and activated by the sigmoid function, and one neuron that preserves the fixed value for the thickness dGST = 1000 nm).

B.2 Dataset and training information

A data point representing a multilayer realization and its angular response is composed of a randomly generated thickness vector $\mathbf{d} = [d_0, d_1, \cdots, d_{60}]$ and the corresponding angular response vector $\mathbf{T} = [T_0, T_1, \cdots T_{179}]$ calculated by the transfer matrix method (TMM), which constitutes the total dataset of 2×10^6 realizations. To improve the learning scope of physically allowed responses, we diversify the realizations with
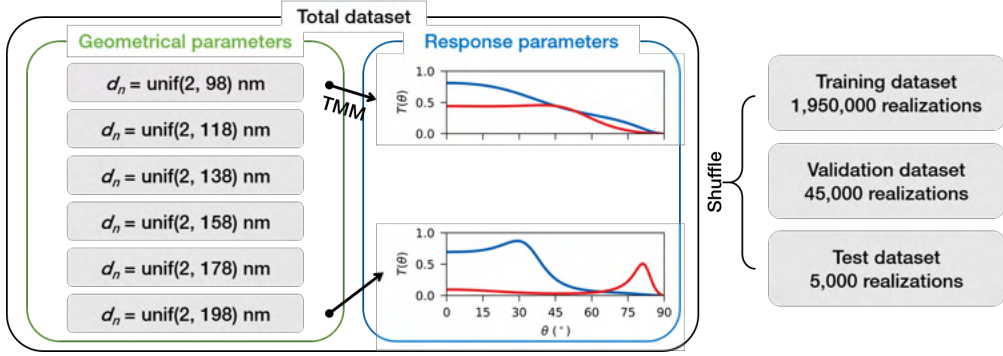
Figure B.1: The structure data d_l are generated from 6 uniform distributions of different ranges, and their corresponding optical response data are calculated through the TMM. The total dataset of 2×10^4 realizations is divided into training, validation, and test datasets.

different characteristic lengths and their deviations by applying various ranges for the uniform random generation of d_l: (i) $d_l = \mathrm{unif}(2, 98)$ nm, (ii) $d_l = \mathrm{unif}(2, 118)$ nm, (iii) $d_l = \mathrm{unif}(2, 138)$ nm, (iv) $d_l = \mathrm{unif}(2, 158)$ nm, (v) $d_l = \mathrm{unif}(2, 178)$ nm, and (vi) $d_l = \mathrm{unif}(2, 198)$ nm (Fig. B.1), where $\mathrm{unif}(a, b)$ denotes the uniform random distribution between a and b. The overall bound of d_l is thus (2, 198) nm, which corresponds to the limit of the final sigmoid activation in R2GNet. All the partial datasets (i-vi) constitute the same portion (1/6) of the total dataset, which are then uniformly shuffled and divided again into training, validation, and test datasets of 1.95×10^6, 4.5×10^4, and 5×10^3 realizations, respectively.

For the training, we use the adaptive momentum (ADAM) [D. P. Kingma, J. Ba, arXiv:1412.6980 (2014)]] optimizer with momentum decay rate β = (0.9, 0.999), stability factor ϵ = 1×10^{-8}, and initial learning rates 1×10^{-2}, 1×10^{-3}, 1×10^{-1}, and 1×10^{-3} for G2RNet, R2GNet, mG2RNet, and mR2GNet, respectively. During the training process, the training dataset is further split into 39 mini-batches of 5×10^4 realizations for stochastic optimization in every epoch, and the learning rates are scheduled to be reduced by half when there is no decrease in the training loss during 25
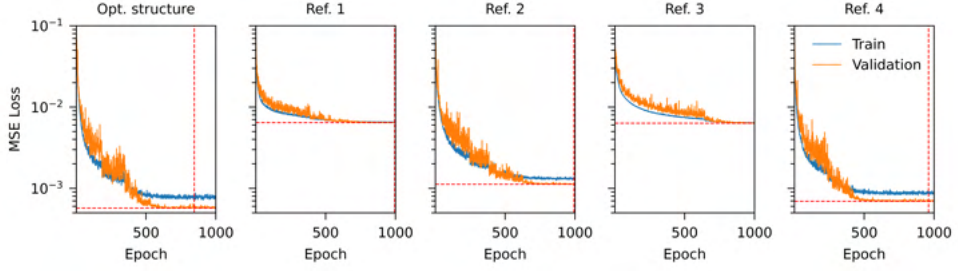
Figure B.2: From left to right, each network has 10, 10, 10, 2, and 6 hidden layers of 180, 45, 90, 180, and 180 neurons per layer, respectively. The minimum validation losses of 5.7×10^4, 6.4×10^{-3}, 1.1×10^{-3}, 6.3×10^{-3}, and 6.9×10^{-4} are indicated by red dashed lines; the leftmost optimal structure is used in the main text.

consecutive epochs. The training of the DNNs is performed by PyTorch on 2 parallel NVIDIA RTX 2080ti GPUs. Various combinations of the hyperparameters for the DNN architecture in the main text are also tested. The results in Figs. B.2-B.5 show that the DNNs with more hidden layers and neurons are optimized to a smaller loss.
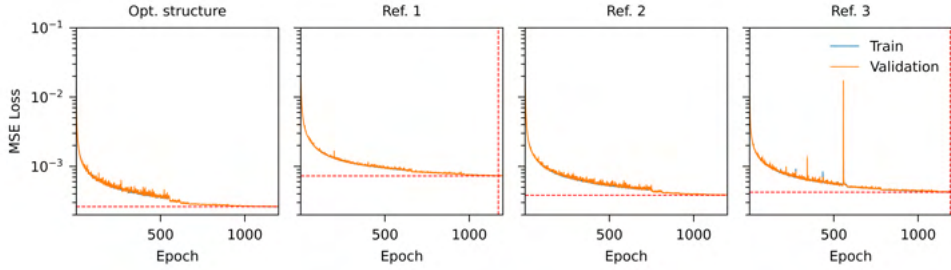
Figure B.3: From left to right, each network has 6, 6, 6, and 3 hidden layers of 120, 30, 60, and 120 neurons per layer in the R2G part, respectively, along with 10 hidden layers of 180 neurons each in the pre-trained G2RNet part in common. The minimum validation losses of 2.6×10^{-4}, 7.3×10^{-4}, 3.8×10^{-4}, and 4.2×10^{-4} are indicated by red dashed lines; the leftmost optimal structure is used in the main text.
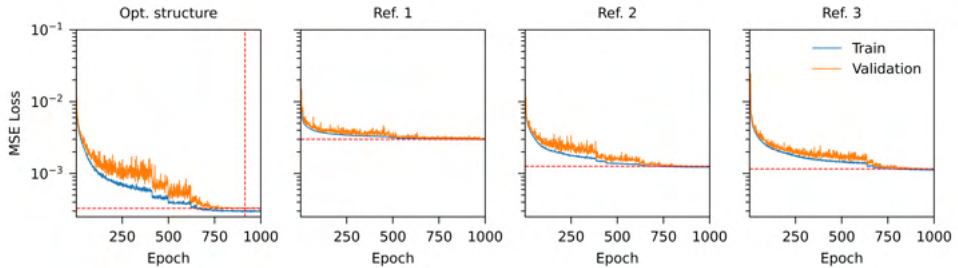
Figure B.4: From left to right, each network has 6, 6, 6, and 3 hidden layers of 120, 30, 60, and 120 neurons per layer, respectively. The minimum validation losses of 3.3×10^{-4}, $3.0 \times 10^{--3}$, $1.7 \times 10{-3}$, and 1.1×10^{-4} are indicated by red dashed lines; the leftmost optimal structure is used in the main text.
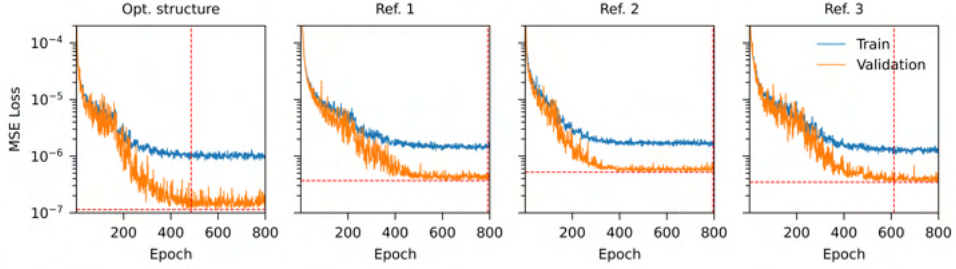
Figure B.5: From left to right, each network has 4, 4, 4, and 2 hidden layers of 120, 30, 60, and 120 neurons per layer in the R2G part, respectively, along with 6 hidden layers of 120 neurons each in the pre-trained G2RNet part in common. The minimum validation losses of 1.1×10^{-7}, 3.6×10^{-7}, 5.2×10^{-7}, and 3.5×10^{-7} are indicated by red dashed lines; the leftmost optimal structure is used in the main text.

B.3 Normalized intensity profiles

In the 2D simulation for verifying the device operations, we assume a cylindrical wave excitation. The wave intensity then decreases with order of $\sim 1/r$ as it propagates in outgoing direction, even if there is no scattering through a device. This reduction thus gives rise to the difference in color scales at the both sides of the device in Figure 3g despite its transparency. In Fig. B.6, the normalized field intensity $|E_{\text{tot}}/E_{\text{inc}}|^2$ is plotted, which compensates the $\sim 1/r$ decrease in intensity, to clearly show this effect. Figs. B.6a-d correspond to Figs. 4.3c,d,g, and h in the main text, respectively. In Fig. B.6c, now the both sides of the device show the similar relative wave intensity level to the incident cylindrical wave.

In addition, we also verify graphically the high-θ suppression due to the cut-off angles in broadband active switching devices by extending the simulation domain in y-direction ($0 < y < 100\ \mu$m, Figs. B.6c,d). By measuring the angles of the contours with the corresponding target transmission levels ($T_a = 0.8$, $T_c = 0.1$), it turns out that the designed device exhibits actual cut-off angles about $\sim 83.4°$ and $\sim 76.6°$ for a-GST (transparent, Fig. B.6c) and c-GST (opaque, Fig. B.6d) phases, respectively.

Although these values are quite deviated from the target cut-off angle $75°$, especially for the transparent operation, they show good agreements with the ground-truth responses of the proposed device, as shown in Figure 3. In Figure 3e, the blue symbol (*a*-GST, ground-truth) drops at the higher angle than that of the blue line (*c*-GST, target), while the red symbol (*c*-GST, ground-truth) drops almost coincidentally with the red line (*c*-GST, target).

B.4 Field distributions calculated by the finite element method

We verify the examples of the functional regressor in the main text by using the finite element method (FEM). The FEM-calculated results in Fig. B.6 show the cylindrical electromagnetic (EM) wave excited from a line source at the origin, including the perfectly matched layer surrounding the domain for suppressing unrealistic reflections. B.7 shows excellent agreement with Fig. 4.3 in the main text. Although we assume cylindrical wave excitations in both TMM and FEM calculations, the TMM utilizes only the Bessel function of the first kind $J_0(k_0 r)$,

$$J_0(k_0 r) \sim \int \mathrm{d}^2 \mathbf{k} \exp(i\mathbf{k} \cdot \mathbf{r}) \delta(|\mathbf{k}| - k_0), \tag{B.1}$$

due to the singularity in the second kind $Y_0(k_0 r)$. This results in marginal differences between the interference patterns of the two results.
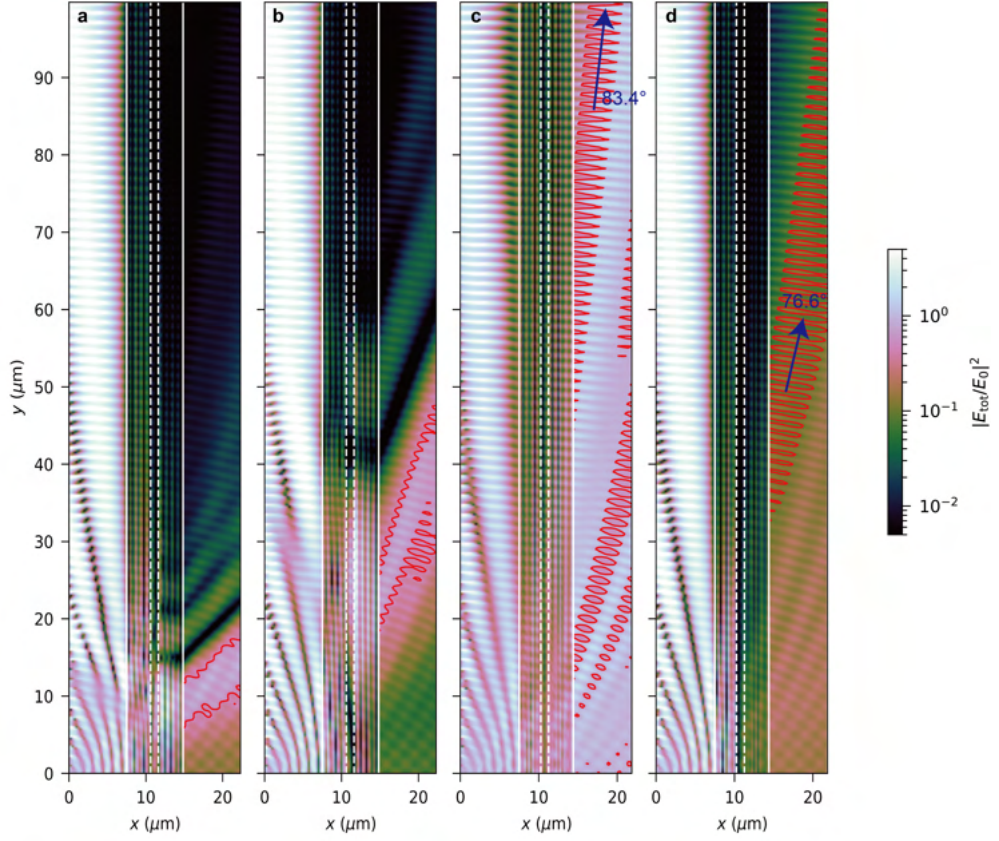
Figure B.6: Extended plot for Figs. 4.3c,d,g,h with normalization. The field intensity is normalized by the cylindrical wave intensity. Red contours indicate the normalized intensity levels for (a,b) the half-maximum values for the angle-selective switching device (= 0.5) and (c,d) the cut-off values for the broadband switching device (= 0.8 for (c) and = 1.0 for (d)). Blue arrows in (c,d) indicate the angle of contour profiles, representing the cut-off angle.

B.5 Model performance of R2GNet

The regression performance of the trained R2GNet can be evaluated by various metrics: mean absolute error (MAE), root mean squared error (RMSE), or averaged R-squared score ($R^2 = (R_a^2 + R_c^2)/2$) of the TMM-calculated true response $\mathbf{T}^{(\text{true})}$ from the
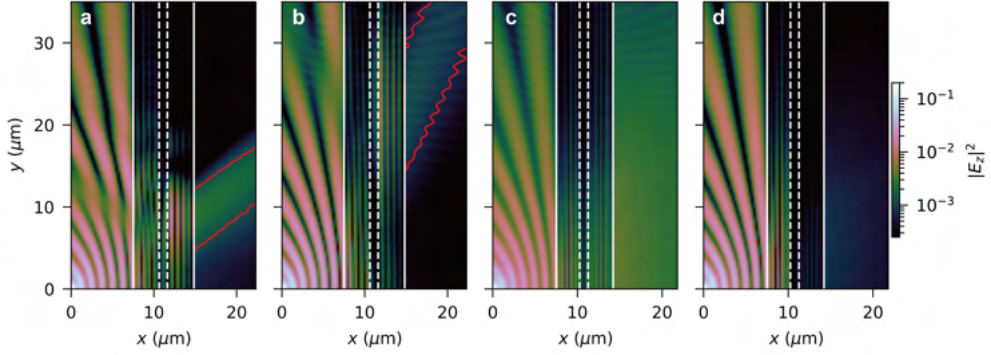
Figure B.7: 2D intensity profiles calculated by the FEM. (a,b) Angle-selective and (c,d) broadband switching devices for both GST phases: (a,c) *a*-GST and (b,d) *c*-GST.

designed realizations with respect to the target response $\mathbf{T}^{(\text{tar})}$, as defined in Eq. (B.2):

$$\text{MAE} = \frac{1}{180} \sum_{m=0}^{1} 79 \left| T_m^{(\text{true})} - T_m^{(\text{tar})} \right|,$$

$$\text{RMSE} = \left[\frac{1}{180} \sum_{m=0}^{1} 79 \left| T_m^{(\text{true})} - T_m^{(\text{tar})} \right|^2 \right]^{1/2},$$

$$R_a^2 = 1 - \frac{\sum_{m=0}^{89} \left| T_m^{(\text{true})} - T_m^{(\text{tar})} \right|^2}{\sum_{m=0}^{89} \left| T_m^{(\text{tar})} - \text{mean}\left[T^{(\text{tar})} \right] \right|^2},$$

$$R_c^2 = 1 - \frac{\sum_{m=90}^{179} \left| T_m^{(\text{true})} - T_m^{(\text{tar})} \right|^2}{\sum_{m=90}^{179} \left| T_m^{(\text{tar})} - \text{mean}\left[T^{(\text{tar})} \right] \right|^2}, \tag{B.2}$$

For angle-selective and broadband switching devices, we examine the target parameters defining the device operation in Figs. B.8-B.10: (θ_a, θ_c) and (T_a, T_c), respectively. The comparison is conducted with different auxiliary parameters for angle-selective and broadband switching of $\theta_{\text{FWHM}} = 6°$, $12°$, and $18°$ and $\theta_{\text{off}} = 45°$, $75°$, and $85°$, respectively. While the RMSE is sensitive to the outlying errors, as depicted by the yellow point in Fig. B.9c, the MAE (Fig. B.8) shows relatively continuous distributions of the errors. In contrast, the R^2 score exhibits sensitivity of the metric to the relative
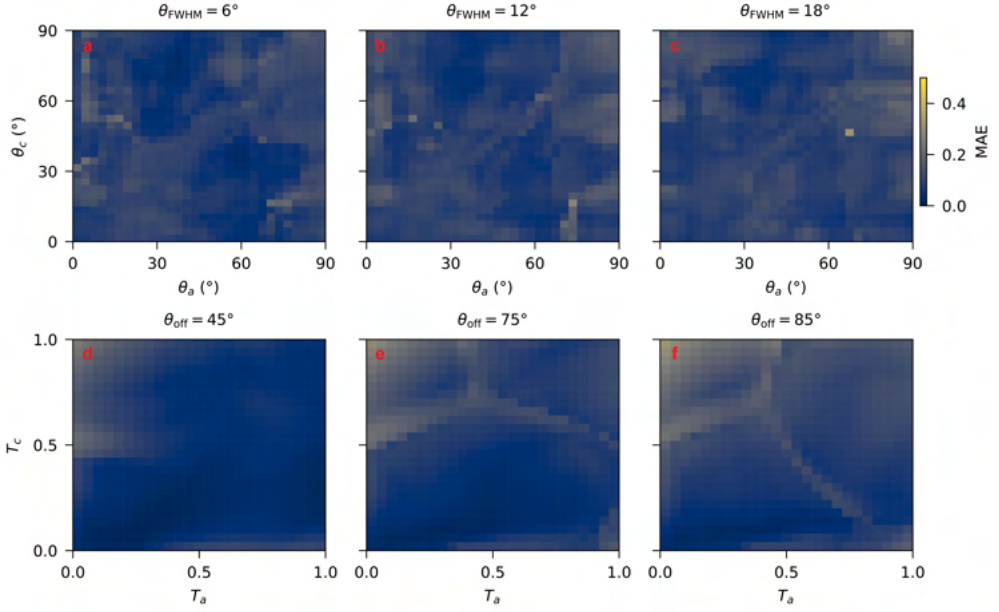
Figure B.8: Model performance evaluated by the MAE. (a-c) Angle-selective switching with target ON-OFF angles (θ_a, θ_c) for three different target broadenings $\theta_{\mathrm{FWHM}} = 6°$, $12°$, and $18°$. (d-f) Broadband switching with target ON-OFF transmission levels (T_a, T_c) for three different target cutoff angles $\theta_{\mathrm{off}} = 45°$, $75°$, and $85°$.
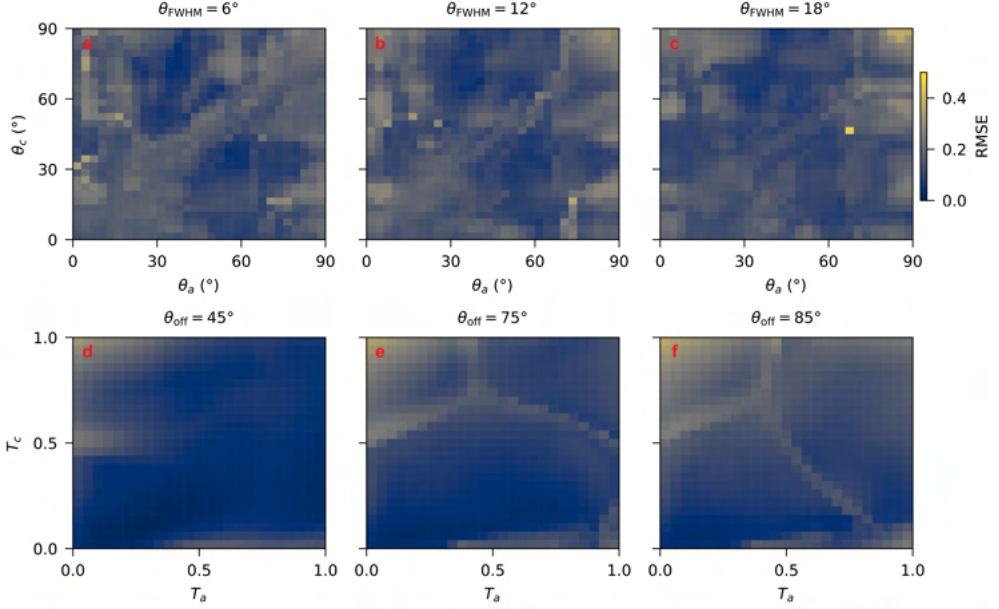
Figure B.9: Model performance evaluated by the RMSE.

shape deformation of the response lines rather than to the absolute error itself. Thus, the R^2 scores are extremely spread out compared to the other two metrics, revealing the clear boundaries between good and poor performances.

B.6 Validity of mR2GNet

The validity of the trained mR2GNet can be evaluated with the evolution of its output distributions. Similar to Figure 3c-f in the main text, the gradual change in the structural statistics and the accuracy of the controllability metric is shown in Fig. B.11. The smooth variation in both the structural distributions and wave responses shows that mR2GNet describes a physically acceptable transition in terms of wave controllability ($\eta = 0$ to 0.6). In addition, the direct comparison between the target and ground-truth η quantitatively verifies the accuracy of mR2GNet. As shown in the right panels of Fig. B.11, almost all of the realizations achieve true TMM-calculated controllability with a
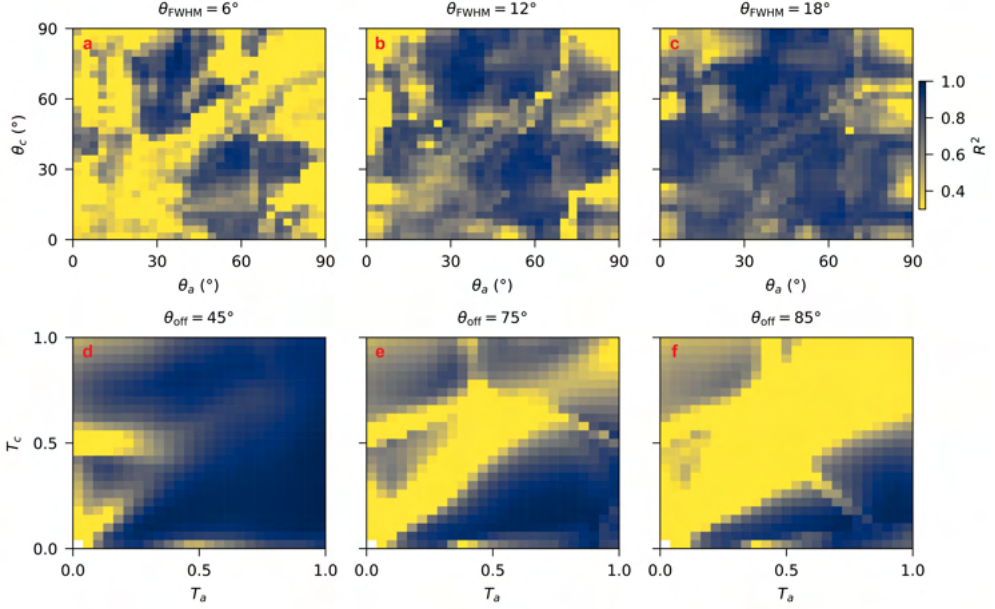
Figure B.10: Model performance evaluated by the R^2 score.

deviation from the target value of less than 0.05.

B.7   Plane-wave responses and effective medium approximation

In this Note, we provide further information regarding the inverse design of the target controllability in the main text (Fig. 4.4). First, the one-dimensional field distributions for selected angular components (0, 15, 30, 45, and 60 degrees) are shown in Fig. B.12, emphasizing the critical role of the GST layer in the energy confinement in relation to the difference between ON and OFF transmittances.

We also compare the results with those of effective medium theory (EMT). For the arrays of the designed average layer thickness $\langle d_l \rangle$ with target controllability $\eta = 0.05$, 0.3, and 0.6, each of the left ($0 \leq l < 30$) and right ($31 \leq l < 61$) parts has its
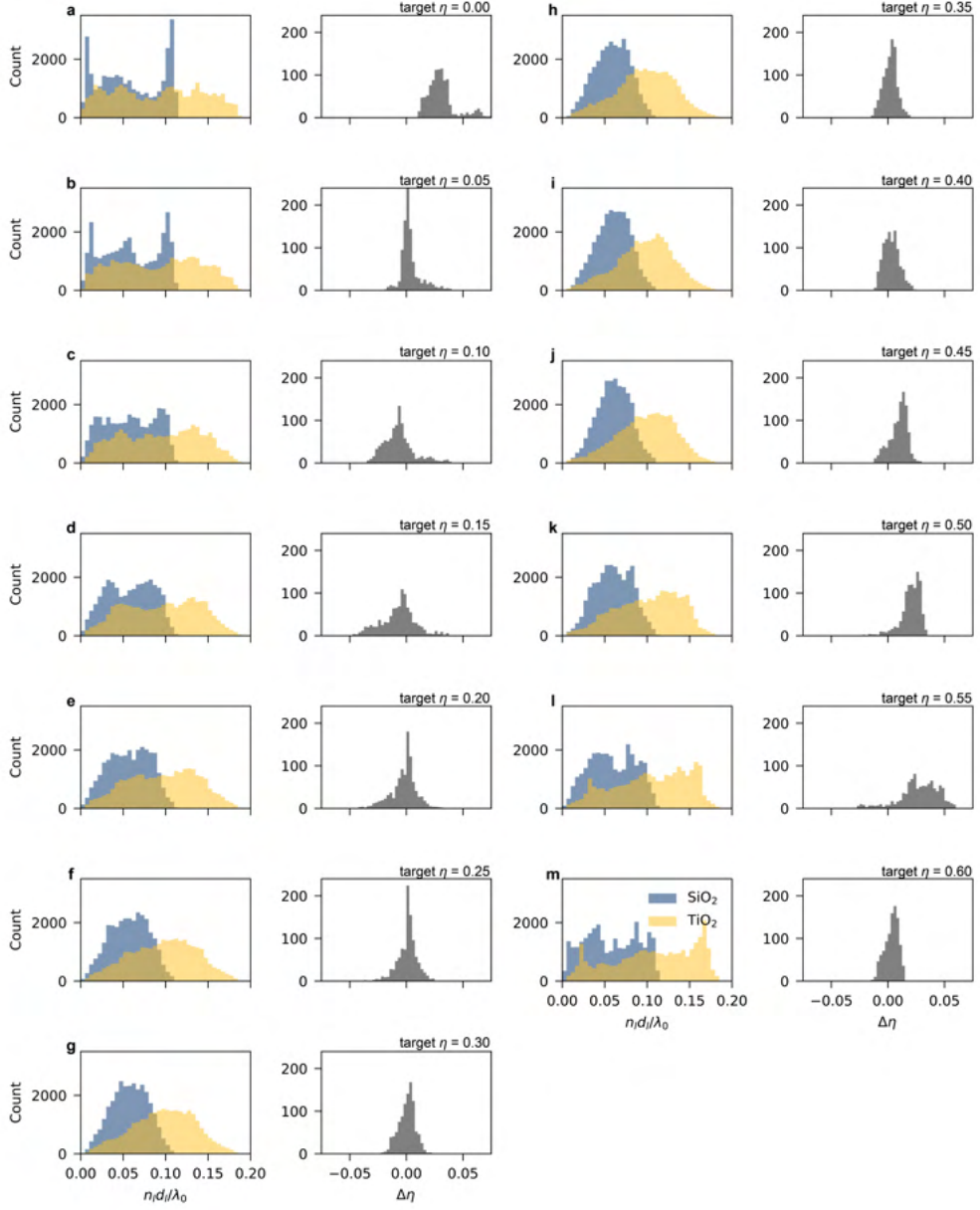
Figure B.11: Evolution of structural statistics and wave controllability from the mR2GNet-designed realizations. $\eta = 0 \text{ to } 0.6$ for (a-m), respectively. Left: distributions of the optical phase evolution, which are the same as Figs. 4.4d-f in the main text. Right: distributions of the deviation of the true controllability from the target controllability, as the model performance of mR2GNet.

corresponding effective permittivity as follows:

$$\epsilon_{\text{EMT}}^{(\text{L,R})} = \frac{\sum_l \epsilon_l \langle d_l \rangle}{\sum_l \langle d_l \rangle} \tag{B.3}$$

The equivalent thickness of the homogeneous layer $d_{\text{tot}}^{(\text{L,R})}$ is then obtained by the following relation:

$$n_{\text{EMT}}^{(L,R)} d_{\text{tot}}^{(\text{L,R})} = \sum_l n_l \langle d_l \rangle , \tag{B.4}$$

where $n_{\text{EMT}}^{(L,R)} = \left[\epsilon_{\text{EMT}}^{(L,R)} \right]^{1/2}$ and $n_l = \epsilon_l^{1/2}$. The responses obtained from the effective permittivity $\epsilon_{\text{EMT}}^{(L,R)}$ and the layer thickness $d_{\text{tot}}^{(L,R)}$ for the homogeneous layer are shown in Fig. B.13 in comparison with the results from mR2GNet. Although the structures from mR2GNet and EMT support identical optical path lengths, there are significant deviations between them, which originate from the phase shift at the boundary, as shown in the relationship between subwavelength localization and the Goos-Hänchen effect[41]. The deviation between mR2GNet and EMT emphasizes the advantage of our machine-learning approach, which enables inverse design of active disorder, overcoming the difficulty in analytical approaches.

B.8 Calculation of the τ order metric

While the conventional translational order metric τ is originally calculated from the pair correlation function over a continuous and infinite domain under the assumption of statistically homogeneous point processes[40], we instead utilize the definition of the τ metric that allows inhomogeneity of finite samples[39]. For a finite range of a 1D two-phase medium composed of alternating layers with low and high permittivities εL and εH, respectively, the indicator function for a material phase is defined as

$$I(x) = \begin{cases} 0, & \epsilon(x) = \epsilon_{\text{L}} \\ 1, & \epsilon(x) = \epsilon_{\text{H}} \end{cases} \tag{B.5}$$
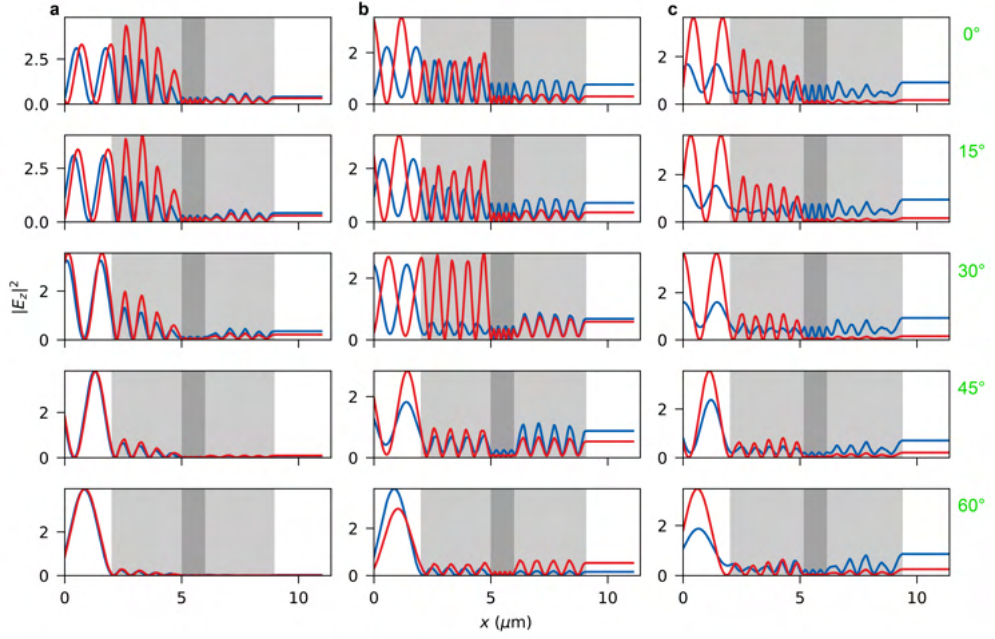
Figure B.12: One-dimensional field distributions for different target controllability values: (a) $\eta = 0.05$, (b) $\eta = 0.3$, and (c) $\eta = 0.6$ with incident angles $\theta_{\text{inc}} = 0°$, $15°$, $30°$, $45°$, and $60°$. Blue and red lines denote a-GST and c-GST phases. White, light grey, and grey regions denote the surrounding air, disordered multilayers, and GST layer, respectively.
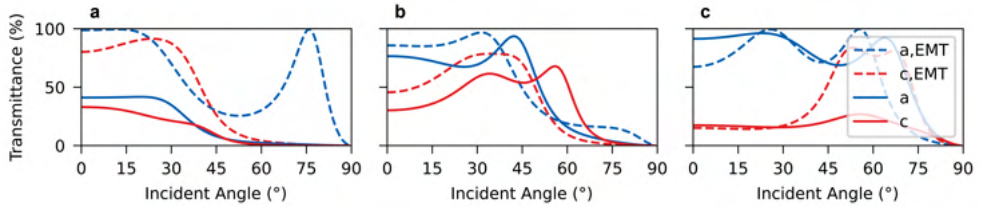
Figure B.13: Comparison with EMT for different target controllability values: (a) $\eta = 0.05$, (b) $\eta = 0.3$, and (c) $\eta = 0.6$. Solid lines: the mR2GNet results, which are the responses of the averaged structure $\langle d_p \rangle$ for the obtained ensemble; dashed lines: the EMT results, which are the responses of the equivalent homogeneous medium.

where $\epsilon(x)$ is the permittivity landscape function with the binary value $\epsilon_{L,H}$ in the finite range. By discretizing this range with N_s points, we achieve the τ metric from the discrete Fourier transform

$$\tilde{I}_k = \sum_{n=0}^{N_s-1} I_n \exp(i2\pi nk/N_s) \tag{B.6}$$

of the indicator array $I_n = I(n\Delta x)$:

$$\tau \equiv \sum_{k\neq 0} \left[\frac{\left|\tilde{I}_k\right|^2}{N} - \left(1 - \frac{N}{N_s}\right) \right]^2. \tag{B.7}$$

where $N = \sum_{n=0}^{N-1} I_n$ is the number of 1śs in the indicator array. The order metric used in this work is an averaged value of τ in the left and right parts of the GST layer. In Figure 5, we normalize the order metrics with τ_c, which is the τ value of the ideal crystal of 30 layers with a periodicity of 200 nm and $N/N_s = 0.5$.

B.9   Extended data for the optimization process

To extract the optimal $\mathbf{c}$, we utilize the gradient ascent optimization that maximizes the correlation

$$\rho_{f,X}(\mathbf{c}) = (N-1)^{-1} \sum_{i=0}^{N-1} \tilde{f}(\mathbf{s}^i; \mathbf{c}) \tilde{X}^i \tag{B.8}$$

between $f(\mathbf{s})$ and $X = T_{\mathrm{avg}}$ or τ, where i is the index for N data points and the tilde denotes the normalized quantity with zero mean and unit variance. While $|\rho_{f,X}| = 1$ allows complete engineering of active disorder for each quantity X, the optimization process leads to

$$\mathbf{c}_{\mathrm{opt}}^{(X)} = \mathrm{argmax}_{\mathbf{c}:||c||=1} |\rho_{f,X}(\mathbf{c})|, \tag{B.9}$$

which describes the contribution of each component in $\mathbf{q}(\mathbf{s})$ to wave (T_{avg}) or matter (τ) quantities.

In detail, the optimization of the 9-dimensional coefficient vector $c^{(X)} = (c_0, c_1, \cdots, c_8)$ enables engineering of active disorder, as shown in Fig. 4.4 in the main text. In detail, we employ 9-dimensional spherical coordinates with a fixed radius,

$$
\begin{aligned}
c_0 &= \cos \phi_0, \\
c_1 &= \sin \phi_0 \cos \phi_1, \\
c_2 &= \sin \phi_0 \sin \phi_1 \cos \phi_2, \\
&\vdots \\
c_7 &= \sin \phi_0 \sin \phi_1 \sin \phi_2 \cdots \cos \phi_7 \\
c_8 &= \sin \phi_0 \sin \phi_1 \sin \phi_2 \cdots \sin \phi_7
\end{aligned}
\tag{B.10}
$$

to impose normalization and a periodic boundary for the parameters $\boldsymbol{\Phi} = (\phi_0, \phi_1, \cdots, \phi_7)$. The gradient ascent iteration with respect to the spherical coordinates is then applied as follows:

$$
\boldsymbol{\Phi}_{n+1}^{(X)} = \boldsymbol{\Phi}_n^{(X)} + \gamma [\nabla_{\boldsymbol{\Phi}} |\rho_{f,X}(\mathbf{c}(\boldsymbol{\Phi}))|]_{\boldsymbol{\Phi} = \boldsymbol{\Phi}_n^{(X)}}
\tag{B.11}
$$

where γ is the step size and $\rho_{f,X}$ is the correlation coefficient between the polynomial expression $f(\mathbf{s}; \mathbf{c}(\boldsymbol{\Phi}))$ up to the second order and the target quantity $X = T_{\mathrm{avg}}$ or τ as defined in the main text. With proper choices of the learning rate and total step number, we observe that the parameter vector Φ and the following $\mathbf{c}_{\mathrm{opt}}(X) = \mathbf{c}(\Phi_{\mathrm{final}}^{(X)})$ converge to their optima, as shown in Fig. B.14.

In addition, the optimization results with a linear expression, $\mathbf{q}(\mathbf{s}) = \mathbf{s}$, $\mathbf{c}(\boldsymbol{\Phi}) = (c_0, c_1, c_2) = (\cos \phi_0, \sin \phi_0 \cos \phi_1, \sin \phi_0 \sin \phi_1)$, are shown in Fig. B.15. This simplified analysis also provides reasonable correlations ($|\rho^{(T)}| = 0.8$, $|\rho^{(T)}| = 0.34$), again emphasizing the distinct role of $\mathbf{s}$ elements.
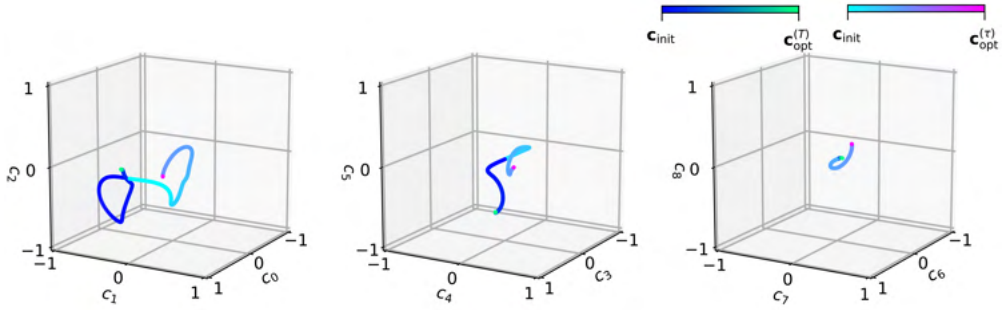
Figure B.14: Optimization trajectories. Left, center, and right panels depict the optimization trajectories of linear (c_0, c_1, c_2 for s_0, s_1, s_2), cross (c_3, c_4, c_5 for $s_0 s_1, s_1 s_2, s_2 s_0$), and second-order ($c_6, c_7, c_8$ for s_0^2, s_1^2, s_2^2) coefficients, respectively, for the evolving $\mathbf{c}^{(T)}(\Phi_n)$ and $\mathbf{c}^{(\tau)}(\Phi_n)$. The optimization time step is $n = 0, 1, 2, \cdots, 3000$ with a step size $\gamma = 0.1$. The initial point ($n = 0$) is set to $\mathbf{c}_{\mathrm{init}} = [1, 0, 0, \cdots]$ for both cases. As n approaches 3000, the parameters converge to the optimal points $\mathbf{c}_{\mathrm{opt}}^{(T)} = [0.27, -0.55, -0.13, 0.56, 0.20, -0.49, -0.09, 0.02, -0.00]$ and $\mathbf{c}_{\mathrm{opt}}^{(\tau)} = [-0.13, -0.21, -0.28, -0.36, -0.08, -0.20, 0.53, 0.50, 0.38]$.
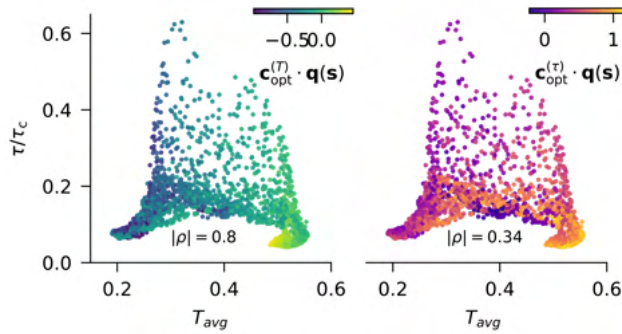
Figure B.15: Optimization for s_0, s_1, and s_2. 2D (T_{avg}, τ) projections of the data points for the target $\eta = 0.3$. Left and right panels are coloured for differently optimized functions of random seeds: $\mathbf{c}_{\mathrm{opt}}^{(T)} \cdots \mathbf{q}(\mathbf{s})$ and $\mathbf{c}_{\mathrm{opt}}^{(\tau)} \cdots \mathbf{q}(\mathbf{s})$ with respect to T_{avg} and τ, respectively. $\mathbf{q}(\mathbf{s}) = \mathbf{s}$, and $\mathbf{c} = [c_0, c_1, c_2]$. All other parameters are the same as those in Fig. 4.3.

Appendix C

Supplementary Information for Chapter 5

C.1   Scattering with Born approximation

With the perturbed potential $\alpha(t) \equiv \epsilon^{-1}(t) = \alpha_{\mathrm{b}}[1 + \Delta\alpha(t)]$, Eq. (5.1) in the main text is modified as follows:

$$\left(\frac{\mathrm{d}^2}{\mathrm{d}t^2} + \omega_{\mathrm{b}}^2\right)\psi(t) = -\omega_{\mathrm{b}}^2 \Delta\alpha(t)\psi(t). \tag{C.1}$$

Assuming that the impulse response of the above operator $\left(\mathrm{d}^2/\mathrm{d}t^2 + \omega_{\mathrm{b}}^2\right)$ is expressed as:

$$\left(\frac{\mathrm{d}^2}{\mathrm{d}t^2} + \omega_{\mathrm{b}}^2\right)G(t,t') = \delta(t - t') \tag{C.2}$$

with a Green's function $G(t,t')$, the total field $\psi_{\mathrm{tot}}(t)$ as the solution of Eq. (C.1) is given by the sum of the homogeneous solution $\psi_{\mathrm{inc}}(t) = \exp\left(-i\omega_{\mathrm{b}}t\right)$ (i.e., the incident wave) and the inhomogeneous solution $\psi_{\mathrm{sca}}(t)$ (i.e., the scattered wave), where:

$$\begin{aligned}
\left(\frac{\mathrm{d}^2}{\mathrm{d}t^2} + \omega_{\mathrm{b}}^2\right)\psi(t) &= -\omega_{\mathrm{b}}^2 \Delta(\alpha)(t)\psi(t) = -\omega_{\mathrm{b}}^2 \int_{-\infty}^{\infty} dt' \Delta\alpha(t')\psi(t')\delta(t - t') \\
&= -\omega_{\mathrm{b}}^2 \int_{-\infty}^{\infty} dt' \Delta\alpha(t')\left(\frac{\mathrm{d}^2}{\mathrm{d}t^2} + \omega_{\mathrm{b}}^2\right)G(t,t'),
\end{aligned} \tag{C.3}$$

which gives:

$$
\begin{aligned}
\psi_{\text{tot}}(t) &= \psi_{\text{inc}}(t) - \omega_{\text{b}}^2 \int_{-\infty}^{\infty} dt' \Delta\alpha(t')\psi_{\text{tot}}(t')G(t,t') \\
&= \psi_{\text{inc}}(t) - \omega_{\text{b}}^2 \int_{-\infty}^{\infty} dt' \Delta\alpha(t')G(t,t') \left\{ \psi_{\text{inc}}(t') - \omega_{\text{b}}^2 \int_{-\infty}^{\infty} dt'' \Delta\alpha(t'')G(t',t'')[\cdots] \right\}.
\end{aligned}
$$

(C.4)

Up to the first-order Born approximation, the scattered field is therefore expressed as:

$$
\psi_{\text{sca}}(t) \simeq -\omega_{\text{b}}^2 \int_{-\infty}^{\infty} dt' \Delta\alpha(t')G(t,t')\psi_{\text{inc}}(t').
$$

(C.5)

Combining Eqs. (5.2) and (5.3) in the main text with the incident wave $\psi_{\text{inc}}(t) = \exp(-i\omega_{\text{b}}t)$, the separated form of the scattering wave in Eq. (5.4) is derived as follows:

$$
\begin{aligned}
\psi_{\text{sca}}(t) &= -\omega_{\text{b}}^2 \int_{-\infty}^{\infty} dt' \Delta\alpha(t')G(t,t')\psi_{\text{inc}}(t') \\
&= -\omega_{\text{b}} \int_{-\infty}^{\infty} dt' \Delta\alpha(t') \sin\left[\omega_{\text{b}}(t-t')\right] e^{-i\omega_{\text{b}}t'} \\
&= -\frac{\omega_{\text{b}}}{2i} \int_{-\infty}^{t} dt' \Delta\alpha(t') \left[e^{i\omega_{\text{b}}(t-t')} - e^{-i\omega_{\text{b}}(t-t')} \right] e^{-i\omega_{\text{b}}t'} \\
&= \frac{\omega_{\text{b}}}{2i} \int_{-\infty}^{t} dt' \Delta\alpha(t') \left[e^{-i\omega_{\text{b}}t} - e^{i\omega_{\text{b}}(t-2t')} \right] \\
&= \frac{\omega_{\text{b}}}{2i} \left[e^{-i\omega_{\text{b}}t} \int_{-\infty}^{t} dt' \Delta\alpha(t') - e^{+i\omega_{\text{b}}t} \int_{-\infty}^{t} dt' e^{-i\omega_{\text{b}}2t'} \Delta\alpha(t') \right], \quad \text{(C.6)}
\end{aligned}
$$

where the resulting two terms in Eq. (C.6) are the forward and backward scattering waves, respectively, as follows:

$$
\begin{aligned}
\psi_{\text{sca,FW}}(t) &= \frac{\omega_{\text{b}}}{2i} e^{-i\omega_{\text{b}}t} \int_{-\infty}^{t} dt' \Delta\alpha(t'), \\
\psi_{\text{sca,BW}}(t) &= \frac{\omega_{\text{b}}}{2i} e^{+i\omega_{\text{b}}t} \int_{-\infty}^{t} dt' e^{-i\omega_{\text{b}}2t'} \Delta\alpha(t').
\end{aligned}
$$

(C.7)

The scattered power is obtained by the square of the scattering wave $\psi_{\text{sca}}(t) =$

$\psi_{\mathrm{sca,FW}}(t) + \psi_{\mathrm{sca,BW}}(t)$ in Eq. (C.7):

$$
\begin{aligned}
|\psi_{\mathrm{sca}}(t)|^2 &= |\psi_{\mathrm{sca,FW}}(t) + \psi_{\mathrm{sca,BW}}(t)|^2 \\
&= |\psi_{\mathrm{sca,FW}}(t)|^2 + |\psi_{\mathrm{sca,BW}}(t)|^2 + 2\,\mathrm{Re}\left[\psi_{\mathrm{sca,FW}}^*(t)\psi_{\mathrm{sca,BW}}(t)\right], \quad (\mathrm{C.8})
\end{aligned}
$$

where $P_{\mathrm{FW}} = |\psi_{\mathrm{sca,FW}}(t)|^2$ and $P_{\mathrm{BW}} = |\psi_{\mathrm{sca,BW}}(t)|^2$ are the scattering powers in the forward and backward directions, respectively, and the last term

$$
2\,\mathrm{Re}\left[\psi_{\mathrm{sca,FW}}^*(t)\psi_{\mathrm{sca,BW}}(t)\right] \tag{C.9}
$$

corresponds to the interference between the two waves. The scattering power in the forward direction is calculated from Eq. (C.7) as follows:

$$
\begin{aligned}
P_{\mathrm{Fw}}(t) = |\psi_{\mathrm{sca,FW}}|^2 &= \left|\frac{\omega_{\mathrm{b}}}{2i}e^{-i\omega_{\mathrm{b}}t}\int_{-\infty}^{t}dt'\Delta\alpha(t')\right|^2 \\
&= \frac{\omega_{\mathrm{b}}^2}{4}\left[\int_{-\infty}^{t}dt'\Delta\alpha(t')\right]^*\left[\int_{-\infty}^{t}dt'\Delta\alpha(t')\right] \\
&= \frac{\omega_{\mathrm{b}}^2}{4}\int_{-\infty}^{t}dt_1'\int_{-\infty}^{t}dt_2'\Delta\alpha^*(t_1')\Delta\alpha(t_2'), \tag{C.10}
\end{aligned}
$$

where the primed variables $t_{1,2}'$ denote the coordinates of two independent scatterers. The ensemble-averaged forward scattering power is then expressed using the two-point correlation function $\hat{C}(t_1', t_2') \equiv \langle\Delta\alpha^*(t_1')\Delta\alpha(t_2')\rangle$:

$$
\langle P_{\mathrm{FW}}(t)\rangle = \frac{\omega_{\mathrm{b}}^2}{4}\int_{-\infty}^{t}dt_1'\int_{-\infty}^{t}dt_2'\,\langle\Delta\alpha^*(t_1')\Delta\alpha(t_2')\rangle = \frac{\omega_{\mathrm{b}}^2}{4}\int_{-\infty}^{t}dt_1'\int_{-\infty}^{t}dt_2'\hat{C}(t_1', t_2'). \tag{C.11}
$$

Setting the finite range of perturbation (i.e., $\hat{C}(t_1', t_2') = 0$ for $t_{1,2}' < 0$ or $t_{1,2}' > T$), the forward scattering power after the perturbation ($t > T$) becomes:

$$
\langle P_{\mathrm{FW}}(t)\rangle = \frac{\omega_{\mathrm{b}}^2}{4}\int_{-\infty}^{T}dt_1'\int_{-\infty}^{T}dt_2'\hat{C}(t_1', t_2') = \frac{\omega_{\mathrm{b}}^2}{4}\int_{-\infty}^{T}dt_1'\int_{-\infty}^{T}dt_2'C(t_1' - t_2') \tag{C.12}
$$

with statistical homogeneity along the temporal axis: $\hat{C}(t_1', t_2') = C(t_1' - t_2')$. Similarly, the backward scattering power is expressed as

$$\langle P_{\mathrm{BW}}(t) \rangle = \frac{\omega_{\mathrm{b}}^2}{4} \int_{-\infty}^{T} dt_1' \int_{-\infty}^{T} dt_2' C(t_1' - t_2') e^{2i\omega_{\mathrm{b}}(t_1' - t_2')}. \qquad \text{(C.13)}$$

When the typical correlation time is much less than the finite duration T, the two-point correlation function $\hat{C}(t_1', t_2')$ can be expressed as a sparse matrix with vanishing off-diagonal components. In this sufficiently long perturbation (large T), the exact results from the double integral in Eqs. (C.12) and (C.13) can be approximated as follows (Fig. C.1):

$$
\begin{aligned}
\langle P_{\mathrm{FW}}(T) \rangle &= \frac{\omega_{\mathrm{b}}^2}{4} \int_{0}^{T} dt_1' \int_{0}^{T} dt_2' C(t_1' - t_2') \\
&\simeq \frac{\omega_{\mathrm{b}}^2}{4} \int_{0}^{T} dt_1' \int_{-\infty}^{\infty} dt_2' C(t_1' - t_2') = \frac{\omega_{\mathrm{b}}^2}{4} \int_{0}^{T} dt_1' \int_{-\infty}^{\infty} d\Delta t C(\Delta t) \\
&= \frac{\omega_{\mathrm{b}}^2 T}{4} \int_{-\infty}^{\infty} d\Delta t C(\Delta t) = \frac{\omega_{\mathrm{b}}^2 T}{4} S(\omega = 0), \\
\langle P_{\mathrm{BW}}(T) \rangle &= \frac{\omega_{\mathrm{b}}^2}{4} \int_{0}^{T} dt_1' \int_{0}^{T} dt_2' C(t_1' - t_2') e^{2i\omega_{\mathrm{b}}(t_1' - t_2')} \\
&\simeq \frac{\omega_{\mathrm{b}}^2}{4} \int_{0}^{T} dt_1' \int_{-\infty}^{\infty} dt_2' C(t_1' - t_2') e^{2i\omega_{\mathrm{b}}(t_1' - t_2')} \\
&= \frac{\omega_{\mathrm{b}}^2}{4} \int_{0}^{T} dt_1' \int_{-\infty}^{\infty} d\Delta t C(\Delta t) e^{2i\omega_{\mathrm{b}}\Delta t} \\
&= \frac{\omega_{\mathrm{b}}^2 T}{4} \int_{-\infty}^{\infty} d\Delta t C(\Delta t) e^{2i\omega_{\mathrm{b}}\Delta t} = \frac{\omega_{\mathrm{b}}^2 T}{4} S(\omega = 2\omega_{\mathrm{b}}). \qquad \text{(C.14)}
\end{aligned}
$$
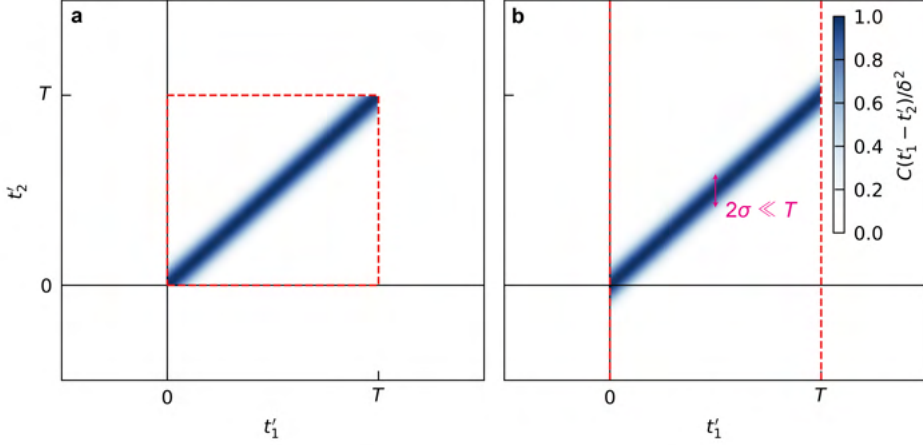
Figure C.1: Condition of long-range approximation. (a) Illustration of the exact 2D integration [Eq. (C.12)] in the finite domain of a square shape with red dashed lines. (b) Illustration of the approximated integration [Eq. (C.14)] with the infinitely extended domain between two red dashed lines for a sufficiently large T compared to the correlation time scale σ.

C.2 Causal Green's function

According to the causality of temporal systems, the analytic expression of Green's function can be derived from the following ansatz:

$$
G(t, t') = \begin{cases} 0 & (t < t') \\ c_1 e^{-i\omega_{\rm b}(t-t')} + c_2 e^{+i\omega_{\rm b}(t-t')} & (t \geq t') \end{cases} .
\tag{C.15}
$$

Incorporating the boundary conditions in Sec. 2.3.1: (1) the continuity of $G(t, t')$ (i.e., **D** field) and (2) the discontinuous jump of $\partial_t G(t, t')$ (i.e., **B** field) with the amount of

the area of the delta function at $t = t'$:

$$G(t, t') = 0 = c_1 + c_2, \tag{C.16}$$

$$\left. \frac{\partial G(t, t')}{\partial t} \right|_{t=t'+0} - \left. \frac{\partial G(t, t')}{\partial t} \right|_{t=t'-0} = 1 = -i\omega_{\mathrm{b}}(c_1 - c_2) - 0. \tag{C.17}$$

Therefore, $c_1 = -c_2 = i/2\omega_{\mathrm{b}}$, and Eq. (5.3) in the main text is obtained.

On the other hand, Green's function of the Helmholtz equation [Eq. (C.2)] can be obtained alternatively using a Fourier transform by supposing that:

$$G(t, t') = \int_{-\infty}^{\infty} \frac{d\omega}{2\pi} \tilde{G}(\omega, t') e^{-i\omega t} \quad \text{and} \quad \tilde{G}(\omega, t') = \int_{-\infty}^{\infty} dt \tilde{G}(t, t') e^{i\omega t}, \tag{C.18}$$

Eq. (C.2) is expressed in the frequency domain as:

$$\left(\omega_{\mathrm{b}}^2 - \omega^2 \right) \tilde{G}(\omega, t') = e^{i\omega t'}, \quad \therefore \tilde{G}(\omega, t') = -\frac{e^{i\omega t'}}{\omega^2 - \omega_{\mathrm{b}}^2}. \tag{C.19}$$

The Green's function in the time domain is then obtained again by applying the inverse Fourier transformation to the above equation, while the result of the integration in the inverse Fourier transformation can be different according to the physical systems of interest, as shown in the retarded, advanced, or Feynman propagators for the Klein-Gordon equation [158]. In this respect, among the possible approximations for locating the poles ($\omega = \pm\omega_{\mathrm{b}}$) in Eq. (C.19) in relation to Cauchy's residue theorem (above or below the real axis, Fig. C.2), we choose both poles below the real axis to guarantee
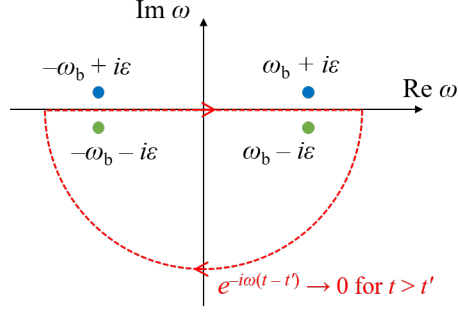
Figure C.2: Schematic of the contour integration in Eq. (C.20). clockwise half-infinite contour for $t > t'$ (red dashed line) and selected poles (green dots) below the real axis, compared to the other candidates (blue dots) above the real axis.

---

the causality condition, $G(t < t', t') = 0$:

$$
\begin{aligned}
G(t, t') &= -\int_{-\infty}^{\infty} \frac{d\omega}{2\pi} \frac{e^{-i\omega(t-t')}}{\omega^2 - \omega_b^2} \\
&= -\lim_{\epsilon \to 0+} \int_{-\infty}^{\infty} \frac{d\omega}{2\pi} \frac{e^{-i\omega(t-t')}}{(\omega - \omega_b + i\epsilon)(\omega + \omega_b + i\epsilon)} \\
&= \Theta(t - t') \lim_{\epsilon \to 0+} \frac{2\pi i}{2\pi} \sum_{\omega_{\text{pole}} = \pm\omega_b - i\epsilon} \text{Res} \left[\frac{e^{-i\omega(t-t')}}{(\omega - \omega_b + i\epsilon)(\omega + \omega_b + i\epsilon)}, \omega_{\text{pole}} \right] \\
&= \frac{1}{\omega_b} \Theta(t - t') \left[-\frac{e^{-i\omega_b(t-t')}}{2i} + \frac{e^{i\omega_b(t-t')}}{2i} \right] = \frac{1}{\omega_b} \sin\left[\omega_b(t - t')\right] \Theta(t - t').
\end{aligned}
$$

$$\text{(C.20)}$$

C.3   Numerical validation of the Born approximation

The Born approximation is valid when the first-order amplitude of the scattering wave is much smaller than the incident wave amplitude2, which also results in the convergence

of the Born series. Therefore, it is necessary to obtain:

$$\left| \omega_{\mathrm{b}}^2 \int_{-\infty}^{\infty} dt' \Delta\alpha(t') G(t,t') \psi_{\mathrm{inc}}(t') \right| = \left| \omega_{\mathrm{b}} \int_{-\infty}^{t} dt' \Delta\alpha(t') \sin\left[\omega_{\mathrm{b}}(t-t')\right] e^{-i\omega_{\mathrm{b}}t'} \right| \ll 1.$$
(C.21)

We introduce two parameters regarding the perturbation $\Delta\alpha(t)$: the fluctuation scale δ and the correlation time σ, which determine the upper bound of the fluctuation $|\Delta\alpha(t)| \leq \delta$ and the lower bound of a nonzero spectral component, as $\Delta\alpha(\omega > \sigma^{-1}) = 0$, respectively. We also assume a finite-time modulation with time T, such that $\Delta\alpha(t) = 0$ for $t < 0$ or $t > T$. Sufficient conditions for Eq. (C.21) are derived as follows:

$$\left| \omega_{\mathrm{b}} \int_{-\infty}^{t} dt' \Delta\alpha(t') \sin\left[\omega_{\mathrm{b}}(t-t')\right] e^{-i\omega_{\mathrm{b}}t'} \right| \leq \omega_{\mathrm{b}} \int_{-\infty}^{t} dt' |\Delta\alpha(t')| \leq \omega_{\mathrm{b}} T \delta \ll 1,$$
(C.22)

and

$$\sigma^{-1} \ll 2\omega_{\mathrm{b}},$$
(C.23)

each describing the weak and slowly varying perturbation.

The above analysis can be verified using numerical assessments. Supposing $T = 10t_0$ and the above δ and σ as the square root of amplitude and the standard deviation of the Gaussian correlation function: $C(\Delta t) = \delta^2 \exp\left[-(\Delta t/\sigma)^2/2\right]$, we estimate the error of the Born approximation compared to the numerically calculated ground-truth results (transfer matrix method, TMM) for various combinations of (σ, δ). For this, we quantify the error with the mean absolute percentage error (MAPE) over the time period ($0 < t < T$):

$$\mathrm{MAPE} = \frac{1}{T} \int_0^T dt \frac{\left|\psi_{\mathrm{sca}}^{(\mathrm{Born})}\right|^2 - \left|\psi_{\mathrm{sca}}^{(\mathrm{TMM})}\right|^2}{\left|\psi_{\mathrm{sca}}^{(\mathrm{TMM})}\right|^2}.$$
(C.24)

Fig. C.3 shows the ensemble-averaged MAPE for 10^3 realizations per ensemble, demon-
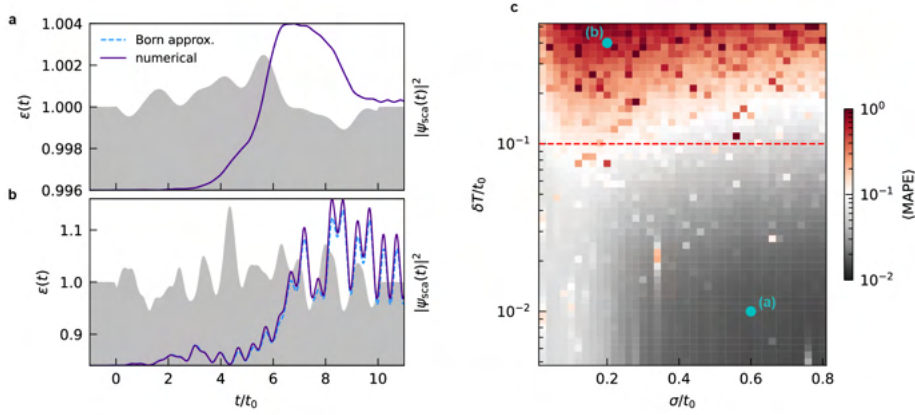
Figure C.3: Numerical validations of the Born approximation. (a,b) Two realizations for $(\sigma/t_0, \delta T/t_0) = (0.6, 0.01)$ (a) and (0.2, 0.4) (b) with $T = 10t_0$. (c) Ensemble-averaged MAPE for various combinations of $(\sigma/t_0, \delta T/t_0)$. 10^3 realizations per ensemble.

strating the acceptable regime of the two parameters, as marked by the red dashed line in Fig. C.3c. For example, each of the two points (a, b) in Fig. C.3c exemplifies the good and bad approximation results, respectively. While the approximated (blue dashed line) and ground-truth (purple solid line) scattering intensities are well matched in Fig. C.3a, there is a noticeable error between the two results in Fig. C.3b.

C.4 Gaussian random generation and the conditions for structure factors

Throughout our study, the random realization of the correlated disorder is obtained by the multivariate Gaussian process. Among various methods for obtaining Gaussian random fields [185], we employ the matrix decomposition method based on the Cholesky factorization. Note that a correlated disorder $\mathbf{x} = L\mathbf{z}$ is expressed as a linear transform of an uncorrelated standard normal disorder $\mathbf{z}$ with an operator L, where L,

x, and z are defined in a finite-dimensional vector space based on the discretization of the time domain. It is observed that L is the lower-triangular operator of the Cholesky decomposition 3 of covariance matrix Γ:

$$\Gamma \equiv \langle \mathbf{x}\mathbf{x}^{\dagger} \rangle = \langle (L\mathbf{z})(L\mathbf{z})^{\dagger} \rangle = \langle L\mathbf{z}\mathbf{z}^{\dagger}L^{\dagger} \rangle = L \langle \mathbf{z}\mathbf{z}^{\dagger} \rangle L^{\dagger} = LL^{\dagger} \qquad (C.25)$$

where the component of Γ is expressed using the correlation function $C(\Delta t)$:

$$\Gamma_{i,j} = \langle x_i x_j^* \rangle = \langle \Delta\alpha^*(t_j)\Delta\alpha(t_i) \rangle = C(t_j - t_i) \qquad (C.26)$$

To generate a discretized random realization $\mathbf{x} = [\Delta\alpha(t_1), \Delta\alpha(t_2), \cdots]^T$ with a given correlation function $C(\Delta t)$, it is necessary to decompose the covariance matrix Γ with Cholesky factorization, which is derived from $C(\Delta t)$. The lower triangular matrix L can then be applied to an uncorrelated standard normal vector $\mathbf{z}$.

There are a few conditions to be considered for this numerical generation of correlated disorder. First, the Hermiticity of $C(\Delta t)$ is trivial by definition:

$$
\begin{aligned}
C(-\Delta t) &= \langle \Delta\alpha^*(t - \Delta t)\Delta\alpha(t) \rangle = \langle \Delta\alpha^*(t)\Delta\alpha(t + \Delta t) \rangle \\
&= \langle \Delta\alpha(t)\Delta\alpha^*(t + \Delta t) \rangle = C^*(\Delta t)
\end{aligned}
\qquad (C.27)
$$

which leads to the real-valued structure factor from:

$$
\begin{aligned}
C^*(\omega) &= \left[\int_{-\infty}^{\infty} d\Delta t\, C(\Delta t)e^{i\omega\Delta t} \right]^* = \int_{-\infty}^{\infty} d\Delta t\, C^*(\Delta t)e^{-i\omega\Delta t} \\
&= \int_{-\infty}^{\infty} d\Delta t\, C(-\Delta t)e^{-i\omega\Delta t} = \int_{\infty}^{-\infty} (-d\Delta t)C(\Delta t)e^{i\omega\Delta t} \\
&= \int_{-\infty}^{\infty} d\Delta t\, C(\Delta t)e^{i\omega\Delta t} = S(\omega)
\end{aligned}
\qquad (C.28)
$$

The second condition regards the maximum value of the correlation function:

$-S(0) \leq \operatorname{Re} C(\Delta t) \leq S(0)$, proven by

$$
\begin{aligned}
\langle |\Delta\alpha(t+\Delta t) \pm \Delta\alpha(t)|^2 \rangle &= \langle |\Delta\alpha(t+\Delta t)|^2 + |\Delta\alpha(t)|^2 \pm 2\operatorname{Re}\Delta\alpha^*(t+\Delta t)\Delta\alpha(t) \rangle \\
&= \langle |\Delta\alpha(t+\Delta t)|^2 \rangle + \langle |\Delta\alpha(t)|^2 \rangle \\
&\quad \pm 2\operatorname{Re}\langle \Delta\alpha^*(t+\Delta t)\Delta\alpha(t) \rangle \\
&= 2S(0) \pm 2\operatorname{Re}C(\Delta t) \geq 0
\end{aligned}
\tag{C.29}
$$

Finally, we note that semi-positive $S(\omega)$ is also required as a sufficient condition to generate a covariance matrix. Suppose that $0 \leq S(\omega)$, the positive semi-definiteness of the covariance matrix Γ is derived from the following relationship:

$$
\begin{aligned}
\mathbf{y}^\dagger \Gamma \mathbf{y} &= \sum_{i,j} y_i^* \Gamma_{i,j} y_j = \sum_{i,j} y_i^* y_j C(t_j - t_i) = \sum_{i,j} y_i^* y_j \int_{-\infty}^{\infty} \frac{d\omega}{2\pi} S(\omega) e^{-i\omega(t_j - t_i)} \\
&= \int_{-\infty}^{\infty} \frac{d\omega}{2\pi} S(\omega) \sum_{i,j} y_i^* y_j e^{-i\omega(t_j - t_i)} = \int_{-\infty}^{\infty} \frac{d\omega}{2\pi} S(\omega) \left| \sum_j y_j e^{i\omega t_j} \right|^2 \geq 0, \ \ \forall \mathbf{y},
\end{aligned}
\tag{C.30}
$$

where $\mathbf{y} = [y_1, y_2, \cdots]^T$ is an arbitrary vector. Every Hermitian and positive-definite matrix has a unique Cholesky decomposition3, which consequently leads to the successful generation of a realization from a given positive structure factor. We note that the above Gaussian random generation can also be achieved with more cost-efficient methods such as the turning bands method or spectral method [185].

C.5 Design of structure factors for target forward and backward scatterings

While the two values of a structure factor $S(\omega = 0)$ and $S(\omega = 2\omega_0)$ independently determine the statistical scattering amplitudes in the forward and backward directions, respectively, the overall shape of the structure factor beyond the two function values,

including area, continuity, and smoothness, should be considered simultaneously for the generation of realizations. For example, the area of structure factors:

$$2\pi C(\Delta t = 0) = \int_{-\infty}^{\infty} d\omega S(\omega) \tag{C.31}$$

should be controlled for removing the scaling effect of disorder fluctuation in realizations. In addition, a target structure factor's continuous and smooth shape is also necessary for the stable numerical generation of realizations.

Considering the above points, for example, the structure factor for forward control $S_{\mathrm{FW}}(\omega)$ can be designed with the following considerations. First, the structure factor is factorized with $\left[1 - (\omega/2\omega_0)^2\right]$ to satisfy $S_{\mathrm{FW}}(\pm 2\omega_0) = 0$, resulting in the expression:

$$S_{\mathrm{FW}}(\omega) = \left[1 - \left(\frac{\omega}{2\omega_0}\right)\right]^2 [S_0 + X(\omega)], \tag{C.32}$$

where $X(\omega)$ is an auxiliary function such that $X(\omega = 0) = 0$ to satisfy $S_{\mathrm{FW}}(\omega = 0) = S_0$. Note that the order n should not be less than 2, which is necessary for smoothening the shape of the structure factor in the vicinity of $\omega = 2\omega_0$, with $S'_{\mathrm{FW}}(\pm 2\omega_0) = 0$ ($n = 2$ in the main text). In addition, $X(\omega)$ should also be factorized by ω^m, and for smoothening, we choose $m = 2$. Finally, in the setting $X(\omega) = K_{\mathrm{FW}}(4\omega/\omega 0)^2$ for a dependent variable $K_{\mathrm{FW}}(S_0)$, we apply the integral condition:

$$\int_{-\infty}^{\infty} \frac{d\omega}{2\pi} S(\omega) = C(\Delta t = 0) = \delta^2, \tag{C.33}$$

which results in:

$$S_{\mathrm{FW}}(\omega; S_0) = \left[1 - \left(\frac{\omega}{2\omega_0}\right)\right]^2 \left[S_0 + K_{\mathrm{FW}}(S_0)\left(\frac{4\omega}{\omega_0}\right)^2\right], \tag{C.34}$$

$$K_{\mathrm{FW}}(S_0) = \frac{1}{4}\left(\frac{105\pi\delta^2}{256\omega_0} - \frac{7S_0}{16}\right). \tag{C.35}$$

Similarly, we design a structure factor $S_{\mathrm{BW}}(\omega)$ for the backward scattering as:

$$S_{\mathrm{FW}}(\omega; S_{2\omega}) = \left(\frac{\omega}{2\omega_0}\right)^2 \left(3 - \frac{|\omega|}{\omega_0}\right)\left[S_{2\omega} + 4K_{\mathrm{BW}}(S_{2\omega})\left(\frac{|4\omega|}{\omega_0}\right)^2\right], \quad \text{(C.36)}$$

where

$$K_{\mathrm{BW}}(S_{2\omega}) = \frac{10\pi\delta^2}{27\omega_0} - \frac{5S_{2\omega}}{8}. \quad \text{(C.37)}$$

C.6 Estimation of $S(\omega)$ for generated realizations

To verify whether the generated realizations describe the target structure factor, we calculate the estimation of the structure factor based on the ergodicity in the correlation functions:

$$C^{(\mathrm{est})}(0 \leq \Delta t \leq T; N_{\mathrm{ens}}) = \frac{1}{N_{\mathrm{ens}}} \sum_{i=1}^{N_{\mathrm{ens}}} \frac{1}{T - \Delta t} \int_0^{T - \Delta t} dt' \Delta\alpha_i^*(t' + \Delta t)\Delta\alpha_i(t'),$$

$$S^{(\mathrm{est})}(\omega; N_{\mathrm{ens}}) = \int_0^T d(\Delta t) C^{(\mathrm{est})}(t; N_{\mathrm{ens}})\left(e^{i\omega\Delta t} + e^{-i\omega\Delta t}\right) \quad \text{(C.38)}$$

where $S^{(\mathrm{est})}(\Delta t; N_{\mathrm{ens}})$ is the estimation of the ensemble-averaged correlation function for total N_{ens} different realizations of $\Delta\alpha_i(t)$ ($i = 1, 2, \cdots, N_{\mathrm{ens}}$), and $S^{(\mathrm{est})}(\omega; N_{\mathrm{ens}})$ is the Fourier transform for the symmetric correlation function $C(-\Delta t) = C(\Delta t)$. In Fig. C.4, several examples of target structure factors in Eqs. (C.34) and (C.36) and their statistical estimations are displayed. As N_{ens} increases, the estimated structure factors approach the corresponding target structure factors. Notably, the order of $N_{\mathrm{ens}} = 10^4$ leads to almost precise coincidence between the target and estimated structure factors. Therefore, we choose $N_{\mathrm{ens}} = 10^4$ as the realization number per ensemble for statistical analysis in our study.
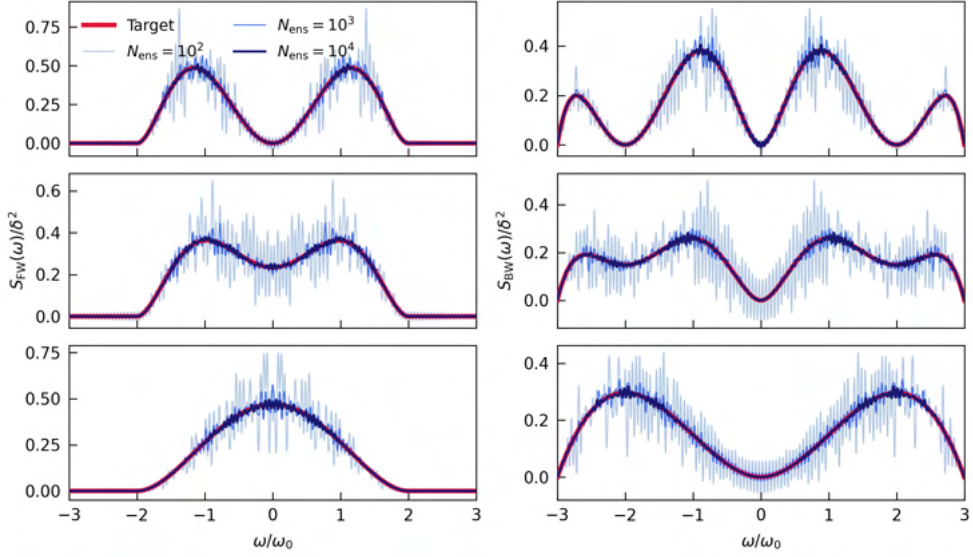
Figure C.4: Estimation of the structure factors. (left) $S_{\text{FW}}^{(\text{est})}(\omega)$ and (right) $S_{\text{BW}}^{(\text{est})}(\omega)$ compared to the corresponding target structure factors $S_{\text{FW,BW}}(\omega)$ for different values of design parameters, $S_{0,2\omega} = 0$ (top), max/2 (middle), and max (bottom).

C.7   Details of $S_{\text{C}}(\omega)$ and $S_{\text{P}}(\omega)$

We first introduce the function $B(x)$:

$$B(x) = \begin{cases} (x^2 - 1)^2, & |x| \leq 1 \\ 0, & \text{otherwise} \end{cases}, \tag{C.39}$$

which is continuous and of the C^1 class, thereby continuously differentiable. We utilize this function to describe both sharp Bragg peaks and near-Poisson broad bumps with different bandwidths.

First, the structure factor $S_{\text{P}}(\omega)$ for the near-Poisson structure factor is expressed with a modified width,

$$S_{\text{P}}(\omega) \sim B\left(\frac{\omega}{\Delta\omega}\right) \tag{C.40}$$

where $\Delta\omega = 2\omega_0$ is the standard bandwidth of the broadband bump.

Next, the structure factor $S_{\mathrm{C}}(\omega)$ for the crystal is expressed as:

$$S_{\mathrm{C}}(\omega) \sim \mathrm{sech}\left(\frac{\omega}{\Delta\omega/4}\right)\sum_{\omega_{\mathrm{c}}} B\left(\frac{\omega - \omega_{\mathrm{c}}}{\Delta\omega/40}\right), \tag{C.41}$$

where ω_{c} is the summation index over

$$[\pm 0.5\omega_0, \pm\omega_0, \pm 1.5\omega_0, \pm 2.5\omega_0, \pm 3\omega_0, \pm 3.5\omega_0, \pm 4\omega_0] \tag{C.42}$$

for the centre frequencies of Bragg peaks with reduced bandwidth $(\Delta\omega/4)$ compared to $S_{\mathrm{P}}(\omega)$, and the sech function represents the envelope function for different heights of the Bragg peaks. We note that both $S_{\mathrm{P}}(\omega)$ and $S_{\mathrm{C}}(\omega)$ are numerically normalized so that:

$$\int_{-4\omega_0}^{4\omega_0} \frac{d\omega}{2\pi} S_{\mathrm{C,P}}(\omega) = C_{\mathrm{C,P}}(\Delta t = 0) = \delta^2. \tag{C.43}$$

In this setting, the structure factor of Eq. (5.7) in the main text can possess the same onsite correlation equal to δ^2 regardless of ξ.

Appendix D

Numerical Methods

D.1 Plane-wave expansion method

Plane-wave expansion method (PWEM) is the most basic method for the calculation of photonic band structures, based on the reciprocal-space representation of the eigenvalue problem. Consider the two-dimensional Helmholtz equation:

$$\left[\nabla^2 + k_0^2 \epsilon(\mathbf{r})\right]\psi(\mathbf{r}) = 0, \tag{D.1}$$

where $\mathbf{r} = (x, y)$, $\epsilon(\mathbf{r})$ is the relative permittivity function as an optical potential, $\omega = ck_0$ is the harmonic frequency, and TE polarization is assumed: $\mathbf{E}(\mathbf{r}; t) = \hat{\mathbf{z}}\psi(\mathbf{r})e^{-i\omega t}$. Then, Eq. (D.1) is modified to the eigen-equation

$$\left[-\frac{1}{\epsilon(\mathbf{r})}\nabla^2\right]\psi = \frac{\omega^2}{c^2}\psi. \tag{D.2}$$

As described previously, a periodic potential $\epsilon(\mathbf{r}) = \epsilon(\mathbf{r} + \mathbf{R})$ for lattice vectors $\mathbf{R}$ leads to the Bloch wave function:

$$\psi(\mathbf{r}) = u_{\mathbf{k}}(\mathbf{r})e^{i\mathbf{k}\cdot\mathbf{r}}, \tag{D.3}$$

where u has the same periodicity with $\epsilon(\mathbf{r})$. Using the Fourier transforms of $u(\mathbf{r})$ and the reciprocal of $\epsilon(\mathbf{r})$:

$$\psi(\mathbf{r}) = \sum_{\mathbf{G}} \tilde{u}_{\mathbf{G}} e^{i(\mathbf{G}+\mathbf{k})\cdot\mathbf{r}}, \tag{D.4}$$

$$\frac{1}{\epsilon(\mathbf{r})} = \sum_{\mathbf{G}} \tilde{\alpha}_{\mathbf{G}} e^{i\mathbf{G}\cdot\mathbf{r}}, \tag{D.5}$$

where $\mathbf{G}$ is the reciprocal lattice vectors satisfying $e^{i\mathbf{G}\cdot\mathbf{R}} = 1$ for all $\mathbf{R}$, Eq. (D.3) leads to

$$\sum_{\mathbf{G},\mathbf{G}'} \tilde{\alpha}_{\mathbf{G}} \tilde{u}_{\mathbf{G}'} \left|\mathbf{G}' + \mathbf{k}\right|^2 e^{i(\mathbf{G}+\mathbf{G}'+\mathbf{k})\cdot\mathbf{r}} = \frac{\omega^2}{c^2} \sum_{\mathbf{G}} \tilde{u}_{\mathbf{G}} e^{i(\mathbf{G}+\mathbf{k})\cdot\mathbf{r}}, \tag{D.6}$$

which is further simplified to

$$\sum_{\mathbf{G}',\mathbf{G}''} \tilde{\alpha}_{\mathbf{G}''-\mathbf{G}'} \tilde{u}_{\mathbf{G}'} \left|\mathbf{G}' + \mathbf{k}\right|^2 e^{i\mathbf{G}''\cdot\mathbf{r}} = \frac{\omega^2}{c^2} \sum_{\mathbf{G}} \tilde{u}_{\mathbf{G}} e^{i\mathbf{G}\cdot\mathbf{r}}. \tag{D.7}$$

From the fact that each Fourier component of the left and the right-hand side of Eq. (D.7) should equal, it is reduced for all $\mathbf{G}$ that,

$$\sum_{\mathbf{G}'} \tilde{\alpha}_{\mathbf{G}-\mathbf{G}'} \tilde{u}_{\mathbf{G}'} \left|\mathbf{G}' + \mathbf{k}\right|^2 = \frac{\omega^2}{c^2} \tilde{u}_{\mathbf{G}}. \tag{D.8}$$

For simplicity, let's consider a one-dimensional crystal, with $\mathbf{R} = \hat{\mathbf{x}} n a$ and $\mathbf{G} = \hat{\mathbf{x}} 2\pi m/a$ for $n, m \in \mathbb{Z}$. Under this assumption, Eq. (D.8) is expressed in the following matrix form:

$$P(Q + kI)^2 \tilde{\mathbf{u}} = \frac{\omega^2}{c^2} \tilde{\mathbf{u}}, \tag{D.9}$$

where

$$P = \begin{bmatrix} \ddots & & & \\ & \tilde{\alpha}_0 & \tilde{\alpha}_{-1} & \tilde{\alpha}_{-2} \\ & \tilde{\alpha}_1 & \tilde{\alpha}_0 & \tilde{\alpha}_{-1} \\ & \tilde{\alpha}_2 & \tilde{\alpha}_1 & \tilde{\alpha}_0 \\ & & & & \ddots \end{bmatrix}, \ Q = \begin{bmatrix} \ddots & & & \\ & -\frac{2\pi}{a} & & \\ & & 0 & \\ & & & \frac{2\pi}{a} \\ & & & & \ddots \end{bmatrix}, \quad \text{(D.10)}$$

$k = |\mathbf{k}|$, and $\tilde{\mathbf{u}} = [\cdots, \tilde{u}_{-1}, \tilde{u}_0, \tilde{u}_1, \cdots]^T$. Now, Eq. (D.9) can be easily solved through a numerical eigenvalue problem, which enables obtaining the eigenfrequency as a function of Bloch wavevector: $\omega(\mathbf{k})$.

D.2 Finite element method

In this section, I introduce the finite element method (FEM), a space-discretization-based approximation technique, which is one of the most powerful solvers in various wave and diffusion mechanics including photonics, acoustics, thermal, and structural dynamics. In contrast to the finite difference method, another discretization-based method of modeling physical systems, by which the *values* at sampling points are solved, the significance of FEM is on analyzing the *elements* of the function to be solved, defined on *meshes*.

First, a strong form means an original partial differential equation to be solved. For example, consider the following n-dimensional heat diffusion equation:

$$\boldsymbol{\nabla} \cdot (-k\boldsymbol{\nabla}u) = f, \ \ \mathbf{r} \in \Omega \quad \text{(D.11)}$$

where u, $\mathbf{q} = -k\boldsymbol{\nabla}u$, k, and f are the temperature, heat flux, thermal conductivity,

and heat source, respectively. Boundary conditions at $\partial\Omega$ are given as

$$u = u_0 \qquad\qquad \text{Dirichlet (essential) BC}, \qquad\qquad \text{(D.12)}$$

$$\hat{\mathbf{n}} \cdot k\boldsymbol{\nabla} u = q_0 \qquad\qquad \text{Neumann (natural) BC}. \qquad\qquad \text{(D.13)}$$

On the other hand, the *weak form* is the integral equation with a test function $v(\mathbf{r})$. For an arbitrary function v defined on Ω,

$$\int_{\Omega} [v\boldsymbol{\nabla} \cdot (-k\boldsymbol{\nabla} u)]\mathrm{d}^n\mathbf{r} = \int_{\Omega} fv\mathrm{d}^n\mathbf{r}, \qquad\qquad \text{(D.14)}$$

which is modified to

$$\int_{\Omega} fv\mathrm{d}^n\mathbf{r} = \int_{\Omega} (k\boldsymbol{\nabla} u \cdot \boldsymbol{\nabla} v)\mathrm{d}^n\mathbf{r} - \oint_{\partial\Omega} kv\boldsymbol{\nabla} u \cdot \hat{\mathbf{n}}\mathrm{d}S, \qquad\qquad \text{(D.15)}$$

using the chain rule: $\boldsymbol{\nabla} \cdot (-kv\boldsymbol{\nabla} u) = v\boldsymbol{\nabla} \cdot (-k\boldsymbol{\nabla} u) - k\boldsymbol{\nabla} u \cdot \boldsymbol{\nabla} v$ and the divergence theorem. When incorporating the BCs, for example, isolation with zero heat flux: $-k\boldsymbol{\nabla} u \cdot \hat{\mathbf{n}} = 0$,

$$\therefore \int_{\Omega} fv\mathrm{d}^n\mathbf{r} = \int_{\Omega} (k\boldsymbol{\nabla} u \cdot \boldsymbol{\nabla} v)\mathrm{d}^n\mathbf{r}. \qquad\qquad \text{(D.16)}$$

Equations with a test function such as Eq. (D.16) is called the *weak form*.

For simplicity, suppose one-dimensional case, and $\Omega = (0, 1)$:

$$\int_0^1 f(x)v(x)\mathrm{d}x = \int_0^1 k(x)\frac{\mathrm{d}u}{\mathrm{d}x}\frac{\mathrm{d}v}{\mathrm{d}x}\mathrm{d}x \qquad\qquad \text{(D.17)}$$

FEM with Galerkin's approach demonstrates that a trial function $u(x)$, which is believed to be ground truth, can be approximated using a "finite" number of basis functions on each of meshes,

$$u(x) = \sum_{i=0}^{N} u_i\phi_i(x), \qquad\qquad \text{(D.18)}$$

and under the same basis, it is noted that Eq.(D.17) should hold for any $v(x)$. Therefore,
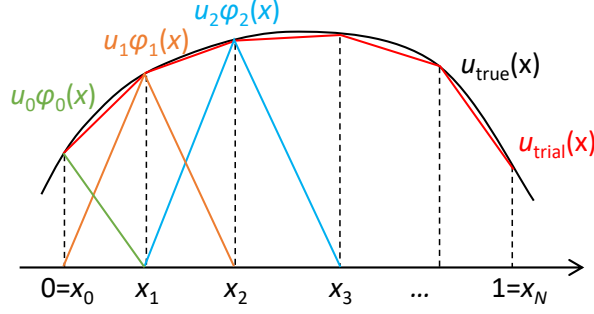
Figure D.1: Illustration of linear basis functions for FEM. The solution $u_{\text{true}}(x)$ is approximated by a trial function $u_{\text{trial}}(x) = \sum_i u_i \phi_i(x)$, where $\phi_i(x)$ is triangular function defined on a mesh component.

cases $v(x) = \phi_j(x)$, $\forall j$ are tested, that is,

$$\int_0^1 f(x)\phi_j(x)\mathrm{d}x = \sum_i u_i \int_0^1 k(x)\frac{\mathrm{d}\phi_i}{\mathrm{d}x}\frac{\mathrm{d}\phi_j}{\mathrm{d}x}\mathrm{d}x, \ \ \forall j. \tag{D.19}$$

Finally the linear equation $A\mathbf{u} = \mathbf{b}$ for $\mathbf{u} = [u_0, u_1, \cdots]$ is solved, where

$$A_{j,i} = \int_0^1 k(x)\frac{\mathrm{d}\phi_i}{\mathrm{d}x}\frac{\mathrm{d}\phi_j}{\mathrm{d}x}\mathrm{d}x, \ \ b_j = \int_0^1 f(x)\phi_j(x)\mathrm{d}x. \tag{D.20}$$

Now, let's move on to our original target system: a photonic crystal [186]. Considering z-polarization in two-dimensional photonic crystal with $\epsilon(x, y)$, the governing equation to be solved is expressed from Eqs. (D.1) and (D.3) as

$$\nabla^2 u + 2i\mathbf{k} \cdot \boldsymbol{\nabla}u - k^2 u + \frac{\omega^2 \epsilon}{c^2}u = 0. \tag{D.21}$$

Applying the following chain-rule relations:

$$v\nabla^2 u = \boldsymbol{\nabla} \cdot (v\boldsymbol{\nabla}u) - \boldsymbol{\nabla}u \cdot \boldsymbol{\nabla}v \tag{D.22}$$

$$v\boldsymbol{\nabla} \cdot (\mathbf{k}u) = \boldsymbol{\nabla} \cdot (\mathbf{k}uv) - \mathbf{k}u \cdot \boldsymbol{\nabla}v \tag{D.23}$$

for arbitrary test function $v(\mathbf{r})$, Eq. (D.21) multiplied by v is modified to:

$$\boldsymbol{\nabla} \cdot (v\boldsymbol{\nabla} u) - \boldsymbol{\nabla} u \cdot \boldsymbol{\nabla} v + 2i[\boldsymbol{\nabla} \cdot (\mathbf{k}uv) - \mathbf{k}u \cdot \boldsymbol{\nabla} v] - k^2 uv + \frac{\omega^2 \epsilon}{c^2} uv = 0. \quad \text{(D.24)}$$

When the obtained weak form [Eq.(D.24)] is integrated over a unit cell Γ, the following integral equation is obtained:

$$\int_\Gamma d^2\mathbf{r}(\boldsymbol{\nabla} u \cdot \boldsymbol{\nabla} v) + 2i\mathbf{k} \cdot \int_\Gamma d^2\mathbf{r}(u\boldsymbol{\nabla} v) + k^2 \int_\Gamma d^2\mathbf{r}(uv) = \frac{\omega^2}{c^2} \int_\Gamma d^2\mathbf{r}(\epsilon uv), \quad \text{(D.25)}$$

since the line integral terms originating from the divergence theorem vanish in the periodic structure. Finally, the second-order eigenvalue problem with parameter $\mathbf{k}$ can be input to a commercial tool such as COMSOL Multiphysics [65], resulting in the band structure $\omega(\mathbf{k})$ as an eigenvalue output.

D.3 Transfer matrix method

Suppose a multilayer system in x-direction composed of L layers, of which each layer has thickness d_l, relative permittivity ϵ_l, and permeability μ_l for $l = 0, 1, \cdots, L-1$, as shown in Fig. D.2. The ambient permittivity and permeability are given as ϵ_{ext} and μ_{ext}. Then, the refractive indices and relative wave impedances for each layer are expressed as $n_l = \sqrt{\epsilon_l \mu_l}$ and $Z_l = \sqrt{\mu_l/\epsilon_l}$, as well as the ambient ones $n_{\text{ext}} = \sqrt{\epsilon_{\text{ext}}\mu_{\text{ext}}}$ and $Z_{\text{ext}} = \sqrt{\mu_{\text{ext}}/\epsilon_{\text{ext}}}$.

Now, we assume that the TE-polarization (nonzero E_z field) wave is incident at angle θ in the xy-plane. For this incident angle, the parallel wave vector is fixed as $k^{\parallel} = k_0 n_{\text{ext}} \sin\theta$ due to the continuous translational symmetry in y-direction, where $k_0 = 2\pi/\lambda_0$ is the wave number in vacuum. On the other hand, the normal wave vectors in each layer are given as

$$k_l^{\perp} = k_0 \sqrt{n_l^2 - n_{\text{ext}}^2 \sin^2\theta}, \quad \text{(D.26)}$$

which can be complex in general depending on the value of refractive index and the incident angle. The wave vector in each layer is then expressed as a function of incident angle: $\mathbf{k}_l^{(\pm)}(\theta) = \pm\hat{\mathbf{x}}k_l^{\perp}(\theta) + \hat{\mathbf{y}}k^{\|}$, where signs $\pm$ denote the forward and backward propagation of wave, respectively.

The boundary condition that the waves at two adjacent l-th ($E_l^{(z,\pm)}$, $H_l^{(y,\pm)}$) and $(l+1)$-th layers ($E_{l+1}^{(z,\pm)}$, $H_{l+1}^{(y,\pm)}$), then becomes the continuity of electric and magnetic fields, as expressed by

$$E_l^{(z,+)} + E_l^{(z,-)} = E_{l+1}^{(z,+)} + E_{l+1}^{(z,-)}, \tag{D.27}$$

$$H_l^{(y,+)} + H_l^{(y,-)} = H_{l+1}^{(y,+)} + H_{l+1}^{(y,-)}, \tag{D.28}$$

which are modified into

$$A_l \begin{bmatrix} E_l^{(z,+)} \\ E_l^{(z,-)} \end{bmatrix} = A_{l+1} \begin{bmatrix} E_{l+1}^{(z,+)} \\ E_{l+1}^{(z,-)} \end{bmatrix} \tag{D.29}$$

where

$$A_l \equiv \begin{bmatrix} 1 & 1 \\ \cos\theta_l/Z_l & -\cos\theta_l/Z_l \end{bmatrix} \text{ and } A_{\text{ext}} \equiv \begin{bmatrix} 1 & 1 \\ \cos\theta/Z_{\text{ext}} & -\cos\theta/Z_{\text{ext}} \end{bmatrix}. \tag{D.30}$$

Here, $\theta_l \equiv \arccos\left(k_l^{\perp}/n_l k_0\right)$ is either the angle of propagation in each layer if given as real-valued number or its complex extension, and the factor of $1/Z_l$ is multiplied for the continuity of magnetic field. On the other hand, the forward and backward waves $[E_l^{(z,+)}, E_l^{(z,-)}]^T$ acquire intra-layer propagation phase from left to right end of l-th layer as

$$B_l = \begin{bmatrix} \exp\left(ik_l^{\perp}d_l\right) & 0 \\ 0 & \exp\left(-ik_l^{\perp}d_l\right) \end{bmatrix}. \tag{D.31}$$

Using these two kinds of matrices, the *transfer matrix* from left ($l = 0$) to right
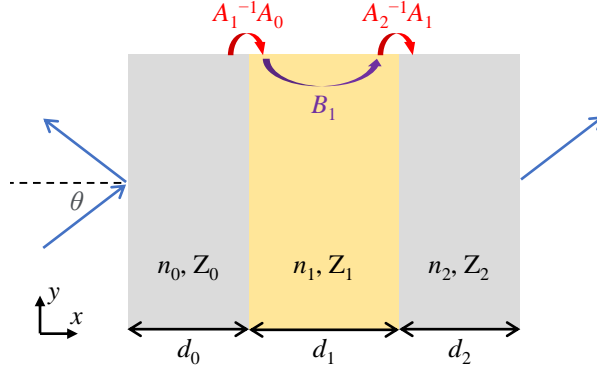
Figure D.2: Schematics of the wave incidence on a multilayer structure.

$(l = L - 1)$ side is obtained through the sequential matrix multiplications:

$$M \equiv A_{\text{ext}}^{-1} \cdot \prod_{p=1}^{L}(A_{L-p}B_{L-p}A_{L-p}^{-1}) \cdot A_{\text{ext}}, \tag{D.32}$$

which relates the reflection ($R = |r|^2$) and transmission ($T = |t|^2$) coefficients as

$$M \begin{bmatrix} 1 \\ r \end{bmatrix} = \begin{bmatrix} t \\ 0 \end{bmatrix}. \tag{D.33}$$

It is noted that, for TM polarization, the electromagnetic duality leads to the change of basis vector from $[E^{(z,+)}, E^{(z,-)}]^T$ to $[H^{(z,+)}, H^{(z,-)}]^T$, which is equivalent to the replacement of permittivity ϵ and permeability μ by each other. Resultingly, the propagation matrix B_l stays unchanged, while the matrix for the boundary condition A_l is modified into

$$A_l^{(\text{TM})} = \begin{bmatrix} 1 & 1 \\ Z_l \cos\theta_l & -Z_l \cos\theta_l \end{bmatrix}. \tag{D.34}$$

Bibliography

[1] J. D. Joannopoulos, S. G. Johnson, J. N. Winn, and R. D. Meade, *Photonic crystals*. Princeton, NJ: Princeton University Press, 2 ed., Feb. 2008.

[2] X. Huang, Y. Lai, Z. H. Hang, H. Zheng, and C. T. Chan, "Dirac cones induced by accidental degeneracy in photonic crystals and zero-refractive-index materials," *Nat. Mater.*, vol. 10, p. 582, May 2011.

[3] S. Yu, C.-W. Qiu, Y. Chong, S. Torquato, and N. Park, "Engineered disorder in photonics," *Nat. Rev. Mater.*, vol. 6, pp. 226–243, Mar. 2021.

[4] S. Torquato, "Hyperuniform states of matter," *Phys. Rep.*, vol. 745, pp. 1–95, June 2018.

[5] W. Man, M. Florescu, E. P. Williamson, Y. He, S. R. Hashemizad, B. Y. C. Leung, D. R. Liner, S. Torquato, P. M. Chaikin, and P. J. Steinhardt, "Isotropic band gaps and freeform waveguides observed in hyperuniform disordered photonic solids," *Proc. Natl. Acad. Sci. U.S.A.*, vol. 110, pp. 15886–15891, Sept. 2013.

[6] E. Galiffi, R. Tirole, S. Yin, H. Li, S. Vezzoli, P. A. Huidobro, M. G. Silveirinha, R. Sapienza, A. Alù, and J. B. Pendry, "Photonics of time-varying media," *Adv. Photonics*, vol. 4, no. 1, p. 014002, 2022.

[7] I. H. Malitson, "Interspecimen comparison of the refractive index of fused silica[*,†]," *J. Opt. Soc. Am.*, vol. 55, p. 1205, Oct. 1965.

[8] J. Kischkat, S. Peters, B. Gruska, M. Semtsiv, M. Chashnikova, M. Klinkmüller, O. Fedosenko, S. Machulik, A. Aleksandrova, G. Monastyrskyi, Y. Flores, and W. T. Masselink, "Mid-infrared optical properties of thin films of aluminum oxide, titanium dioxide, silicon dioxide, aluminum nitride, and silicon nitride," *Appl. Opt.*, vol. 51, p. 6789, Sept. 2012.

[9] T. Cao, C. Wei, R. E. Simpson, L. Zhang, and M. J. Cryan, "Fast tuning of double fano resonance using a phase-change metamaterial under low power intensity," *Sci. Rep.*, vol. 4, Mar. 2014.

[10] H. J. Caulfield and S. Dolev, "Why future supercomputing requires optics," *Nat. Photonics*, vol. 4, pp. 261–263, May 2010.

[11] B. J. Shastri, A. N. Tait, T. F. de Lima, W. H. P. Pernice, H. Bhaskaran, C. D. Wright, and P. R. Prucnal, "Photonics for artificial intelligence and neuromorphic computing," *Nat. Photonics*, vol. 15, pp. 102–114, Jan. 2021.

[12] S. Choi, **J. Kim**, J. Kwak, N. Park, and S. Yu, "Topologically protected all-optical memory," *Adv. Electon. Mater.*, vol. 8, p. 2200579, June 2022.

[13] P. W. Anderson, "Absence of diffusion in certain random lattices," *Phys. Rev.*, vol. 109, pp. 1492–1505, Mar. 1958.

[14] P. W. Anderson, "More is different," *Science*, vol. 177, no. 4047, pp. 393–396, 1972.

[15] **J. Kim**, S. Yu, and N. Park, "Universal design platform for an extended class of photonic Dirac cones," *Phys. Rev. Appl.*, vol. 13, p. 044015, Apr. 2020.

[16] **J. Kim**, S. Park, S. Yu, and N. Park, "Machine-engineered active disorder for digital photonics," *Adv. Opt. Mater.*, vol. 10, p. 2102642, Feb. 2022.

[17] **J. Kim**, D. Lee, S. Yu, and N. Park, "Unidirectional scattering with spatial homogeneity using correlated photonic time disorder," *Nat. Phys.*, 2023. (preprint: arXiv:2208.11884).

[18] N. W. Ashcroft and N. Mermin, *Solid State Physics*. Florence, KY: Brooks/Cole, Jan. 1976.

[19] K. Sakoda, "Proof of the universality of mode symmetries in creating photonic Dirac cones," *Opt. Express*, vol. 20, pp. 25181–25194, Oct. 2012.

[20] J. J. Sakurai and J. Napolitano, *Modern Quantum Mechanics*. Cambridge, England: Cambridge University Press, 3 ed., Sept. 2020.

[21] R. A. DiStasio, G. Zhang, F. H. Stillinger, and S. Torquato, "Rational design of stealthy hyperuniform two-phase media with tunable order," *Phys. Rev. E*, vol. 97, p. 023311, Feb. 2018.

[22] S. Oh, **J. Kim**, X. Piao, S. Kim, K. Kim, S. Yu, and N. Park, "Control of localization and optical properties with deep-subwavelength engineered disorder," *Opt. Express*, vol. 30, p. 28301, July 2022.

[23] B. W. Plansinis, W. R. Donaldson, and G. P. Agrawal, "What is the temporal analog of reflection and refraction of optical beams?," *Phys. Rev. Lett.*, vol. 115, no. 18, p. 183901, 2015.

[24] D. M. Solís and N. Engheta, "Functional analysis of the polarization response in linear time-varying media: A generalization of the kramers-kronig relations," *Phys. Rev. B*, vol. 103, p. 144303, Apr. 2021.

[25] J. Zhang, W. Donaldson, and G. P. Agrawal, "Temporal reflection of an optical pulse from a short soliton: impact of raman scattering," *J. Opt. Soc. Am. B*, vol. 39, p. 1950, June 2022.

[26] K. S. Novoselov, A. K. Geim, S. V. Morozov, D. Jiang, M. I. Katsnelson, I. V. Grigorieva, S. V. Dubonos, and A. A. Firsov, "Two-dimensional gas of massless Dirac fermions in graphene," *Nature*, vol. 438, p. 197, Nov. 2005.

[27] J.-H. Chen, C. Jang, S. Xiao, M. Ishigami, and M. S. Fuhrer, "Intrinsic and extrinsic performance limits of graphene devices on SiO2," *Nat. Nanotechnol.*, vol. 3, pp. 206–209, Mar. 2008.

[28] K. Bolotin, K. Sikes, Z. Jiang, M. Klima, G. Fudenberg, J. Hone, P. Kim, and H. Stormer, "Ultrahigh electron mobility in suspended graphene," *Solid State Commun.*, vol. 146, pp. 351–355, June 2008.

[29] N. Tombros, C. Jozsa, M. Popinciuc, H. T. Jonkman, and B. J. van Wees, "Electronic spin transport and spin precession in single graphene layers at room temperature," *Nature*, vol. 448, pp. 571–574, July 2007.

[30] B. Dlubak, M.-B. Martin, C. Deranlot, B. Servet, S. Xavier, R. Mattana, M. Sprinkle, C. Berger, W. A. D. Heer, F. Petroff, A. Anane, P. Seneor, and A. Fert, "Highly efficient spin transport in epitaxial graphene on SiC," *Nat. Phys.*, vol. 8, pp. 557–561, June 2012.

[31] O. Peleg, G. Bartal, B. Freedman, O. Manela, M. Segev, and D. N. Christodoulides, "Conical diffraction and gap solitons in honeycomb photonic lattices," *Phys. Rev. Lett.*, vol. 98, p. 103901, Mar. 2007.

[32] P. Moitra, Y. Yang, Z. Anderson, I. I. Kravchenko, D. P. Briggs, and J. Valentine, "Realization of an all-dielectric zero-index optical metamaterial," *Nat. Photonics*, vol. 7, pp. 791–795, Aug. 2013.

[33] J.-W. Dong, M.-L. Chang, X.-Q. Huang, Z. H. Hang, Z.-C. Zhong, W.-J. Chen, Z.-Y. Huang, and C. T. Chan, "Conical dispersion and effective zero refractive index in photonic quasicrystals," *Phys. Rev. Lett.*, vol. 114, p. 163901, Apr. 2015.

[34] J. Mei, Y. Wu, C. T. Chan, and Z.-Q. Zhang, "First-principles study of Dirac and Dirac-like cones in phononic and photonic crystals," *Phys. Rev. B*, vol. 86, p. 035141, July 2012.

[35] J. Lu, C. Qiu, S. Xu, Y. Ye, M. Ke, and Z. Liu, "Dirac cones in two-dimensional artificial crystals for classical waves," *Phys. Rev. B*, vol. 89, Apr. 2014.

[36] J. Ningyuan, C. Owens, A. Sommer, D. Schuster, and J. Simon, "Time- and site-resolved dynamics in a topological circuit," *Phys. Rev. X*, vol. 5, p. 021031, June 2015.

[37] W. Zhu, S. Hou, Y. Long, H. Chen, and J. Ren, "Simulating quantum spin Hall effect in the topological Lieb lattice of a linear circuit network," *Phys. Rev. B*, vol. 97, p. 075310, Feb. 2018.

[38] F. D. M. Haldane, "Model for a quantum hall effect without landau levels: Condensed-matter realization of the "parity anomaly"," *Phys. Rev. Lett.*, vol. 61, pp. 2015–2018, Oct. 1988.

[39] M. C. Rechtsman, J. M. Zeuner, A. Tünnermann, S. Nolte, M. Segev, and A. Szameit, "Strain-induced pseudomagnetic field and photonic landau levels in dielectric structures," *Nat. Photonics*, vol. 7, pp. 153–158, Dec. 2012.

[40] L.-H. Wu and X. Hu, "Scheme for achieving a topological photonic crystal by using dielectric material," *Phys. Rev. Lett.*, vol. 114, p. 223901, June 2015.

[41] J. Mei, Z. Chen, and Y. Wu, "Pseudo-time-reversal symmetry and topological edge states in two-dimensional acoustic crystals," *Sci. Rep.*, vol. 6, p. 32752, Sept. 2016. Article.

[42] X. Wen, C. Qiu, Y. Qi, L. Ye, M. Ke, F. Zhang, and Z. Liu, "Acoustic landau quantization and quantum-hall-like edge states," *Nat. Phys.*, vol. 15, pp. 352–356, Mar. 2019.

[43] A. A. Soluyanov, D. Gresch, Z. Wang, Q. Wu, M. Troyer, X. Dai, and B. A. Bernevig, "Type-II Weyl semimetals," *Nature*, vol. 527, p. 495, Nov. 2015.

[44] M. Milićević, G. Montambaux, T. Ozawa, O. Jamadi, B. Real, I. Sagnes, A. Lemaître, L. Le Gratiet, A. Harouri, J. Bloch, and A. Amo, "Type-III and tilted Dirac cones emerging from flat bands in photonic orbital graphene," *Phys. Rev. X*, vol. 9, p. 031010, July 2019.

[45] T. Kawarabayashi, Y. Hatsugai, T. Morimoto, and H. Aoki, "Generalized chiral symmetry and stability of zero modes for tilted dirac cones," *Phys. Rev. B*, vol. 83, p. 153414, Apr. 2011.

[46] M. Trescher, B. Sbierski, P. W. Brouwer, and E. J. Bergholtz, "Quantum transport in dirac materials: Signatures of tilted and anisotropic dirac and weyl cones," *Phys. Rev. B*, vol. 91, p. 115135, Mar. 2015.

[47] Y. D. Chong, X.-G. Wen, and M. Soljačić, "Effective theory of quadratic degeneracies," *Phys. Rev. B*, vol. 77, p. 235125, June 2008.

[48] W.-Y. He and C. T. Chan, "The emergence of dirac points in photonic crystals with mirror symmetry," *Sci. Rep.*, vol. 5, Feb. 2015.

[49] H. Huang, S. Zhou, and W. Duan, "Type-II Dirac fermions in the $ptse_2$ class of transition metal dichalcogenides," *Phys. Rev. B*, vol. 94, p. 121117(R), Sept. 2016.

[50] G. G. Pyrialakos, N. S. Nye, N. V. Kantartzis, and D. N. Christodoulides, "Emergence of type-II Dirac points in graphynelike photonic lattices," *Phys. Rev. Lett.*, vol. 119, p. 113901, Sept. 2017.

[51] H.-X. Wang, Y. Chen, Z. H. Hang, H.-Y. Kee, and J.-H. Jiang, "Type-II dirac photons," *npj Quantum Mater.*, vol. 2, Sept. 2017.

[52] J. Y. Lin, N. C. Hu, Y. J. Chen, C. H. Lee, and X. Zhang, "Line nodes, Dirac points, and Lifshitz transition in two-dimensional nonsymmorphic photonic crystals," *Phys. Rev. B*, vol. 96, p. 075438, Aug. 2017.

[53] C. Hu, Z. Li, R. Tong, X. Wu, Z. Xia, L. Wang, S. Li, Y. Huang, S. Wang, B. Hou, C. T. Chan, and W. Wen, "Type-II Dirac photons at metasurfaces," *Phys. Rev. Lett.*, vol. 121, p. 024301, July 2018.

[54] Z. Yang and B. Zhang, "Acoustic type-II weyl nodes from stacking dimerized chains," *Phys. Rev. Lett.*, vol. 117, p. 224301, Nov. 2016.

[55] X. Wu, X. Li, R.-Y. Zhang, X. Xiang, J. Tian, Y. Huang, S. Wang, B. Hou, C. T. Chan, and W. Wen, "Deterministic scheme for two-dimensional type-ii dirac points and experimental realization in acoustics," *Phys. Rev. Lett.*, vol. 124, p. 075501, Feb. 2020.

[56] B. Xie, H. Liu, H. Cheng, Z. Liu, S. Chen, and J. Tian, "Experimental realization of type-ii weyl points and fermi arcs in phononic crystal," *Phys. Rev. Lett.*, vol. 122, p. 104302, Mar. 2019.

[57] M. S. Dresselhaus, G. Dresselhaus, and A. Jorio, *Group theory*. Berlin, Germany: Springer, 2008 ed., Mar. 2007.

[58] B. Zhen, C. W. Hsu, Y. Igarashi, L. Lu, I. Kaminer, A. Pick, S.-L. Chua, J. D. Joannopoulos, and M. Soljačić, "Spawning rings of exceptional points out of Dirac cones," *Nature*, vol. 525, p. 354, Sept. 2015.

[59] H. Zhou, C. Peng, Y. Yoon, C. W. Hsu, K. A. Nelson, L. Fu, J. D. Joannopoulos, M. Soljačić, and B. Zhen, "Observation of bulk Fermi arc and polarization half charge from paired exceptional points," *Science*, vol. 359, no. 6379, pp. 1009–1012, 2018.

[60] X.-T. He, Y.-N. Zhong, Y. Zhou, Z.-C. Zhong, and J.-W. Dong, "Dirac directional emission in anisotropic zero refractive index photonic crystals," *Sci. Rep.*, vol. 5, p. 13085, Aug. 2015.

[61] D. R. Smith, S. Schultz, P. Markoš, and C. M. Soukoulis, "Determination of effective permittivity and permeability of metamaterials from reflection and transmission coefficients," *Phys. Rev. B*, vol. 65, p. 195104, Apr. 2002.

[62] S. Yu, X. Piao, J. Hong, and N. Park, "Metadisorder for designer light in random systems," *Sci. Adv.*, vol. 2, p. e1501851, Oct. 2016.

[63] S. Yu, X. Piao, and N. Park, "Bohmian photonics for independent control of the phase and amplitude of waves," *Phys. Rev. Lett.*, vol. 120, p. 193902, May 2018.

[64] X. Piao, S. Yu, and N. Park, "Design of transverse spinning of light with globally unique handedness," *Phys. Rev. Lett.*, vol. 120, p. 203901, May 2018.

[65] "COMSOL Multiphysics v5.3."

[66] D. Bertsekas, *Nonlinear programming*. Athena Scientific, Sept. 2016.

[67] H. N. S. Krishnamoorthy, Z. Jacob, E. Narimanov, I. Kretzschmar, and V. M. Menon, "Topological transitions in metamaterials," *Science*, vol. 336, pp. 205–209, Apr. 2012.

[68] J. S. Gomez-Diaz, M. Tymchenko, and A. Alù, "Hyperbolic plasmons and topological transitions over uniaxial metasurfaces," *Phys. Rev. Lett.*, vol. 114, June 2015.

[69] D. Xiao, W. Yao, and Q. Niu, "Valley-contrasting physics in graphene: Magnetic moment and topological transport," *Phys. Rev. Lett.*, vol. 99, p. 236809, Dec. 2007.

[70] T. Ma and G. Shvets, "All-si valley-hall photonic topological insulator," *New J. Phys.*, vol. 18, p. 025012, Feb. 2016.

[71] J. B. Oostinga, H. B. Heersche, X. Liu, A. F. Morpurgo, and L. M. K. Vander-sypen, "Gate-induced insulating state in bilayer graphene devices," *Nat. Mater.*, vol. 7, pp. 151–157, Dec. 2007.

[72] J. P. Dowling, M. Scalora, M. J. Bloemer, and C. M. Bowden, "The photonic band edge laser: A new approach to gain enhancement," *J. Appl. Phys.*, vol. 75, no. 4, pp. 1896–1899, 1994.

[73] F. Zangeneh-Nejad and R. Fleury, "Topological analog signal processing," *Nat. Commun.*, vol. 10, p. 2058, May 2019.

[74] D. Ielmini and H.-S. P. Wong, "In-memory computing with resistive switching devices," *Nat. Electron.*, vol. 1, pp. 333–343, June 2018.

[75] J. Gao, Y.-Y. Liu, R. M. D'Souza, and A.-L. Barabási, "Target control of complex networks," *Nat. Commun.*, vol. 5, p. 5415, Nov. 2014.

[76] X. Yang and Z. Cai, "Dynamical transitions and critical behavior between discrete time crystal phases," *Phys. Rev. Lett.*, vol. 126, p. 020602, Jan. 2021.

[77] A. Tikan, J. Riemensberger, K. Komagata, S. Hönl, M. Churaev, C. Skehan, H. Guo, R. N. Wang, J. Liu, P. Seidler, and T. J. Kippenberg, "Emergent nonlinear phenomena in a driven dissipative photonic dimer," *Nat. Phys.*, vol. 17, pp. 604–610, Feb. 2021.

[78] H. Cao and J. Wiersig, "Dielectric microcavities: Model systems for wave chaos and non-hermitian physics," *Rev. Mod. Phys.*, vol. 87, pp. 61–111, Jan. 2015.

[79] S. Stützer, Y. Plotnik, Y. Lumer, P. Titum, N. H. Lindner, M. Segev, M. C. Rechtsman, and A. Szameit, "Photonic topological anderson insulators," *Nature*, vol. 560, pp. 461–465, Aug. 2018.

[80] W. C. Chew, *Waves and fields in inhomogenous media*. IEEE Press Series on Electromagnetic Wave Theory, Piscataway, NJ: IEEE Publications, Jan. 1999.

[81] M. Filoche and S. Mayboroda, "Universal mechanism for anderson and weak localization," *Proc. Natl. Acad. Sci. U.S.A.*, vol. 109, pp. 14761–14766, Aug. 2012.

[82] G. Lefebvre, A. Gondel, M. Dubois, M. Atlan, F. Feppon, A. Labbé, C. Gillot, A. Garelli, M. Ernoult, S. Mayboroda, M. Filoche, and P. Sebbah, "One single static measurement predicts wave localization in complex structures," *Phys. Rev. Lett.*, vol. 117, p. 074301, Aug. 2016.

[83] A. Graves, N. Jaitly, and A.-r. Mohamed, "Hybrid speech recognition with deep bidirectional LSTM," in *2013 IEEE Workshop on Automatic Speech Recognition and Understanding*, pp. 273–278, 2013.

[84] A. Krizhevsky, I. Sutskever, and G. E. Hinton, "ImageNet classification with deep convolutional neural networks," *Communications of the ACM*, vol. 60, pp. 84–90, May 2017.

[85] X. Han, X. Wang, and K. Zhou, "Develop machine learning-based regression predictive models for engineering protein solubility," *Bioinformatics*, vol. 35, pp. 4640–4646, Apr. 2019.

[86] M. Lutter, C. Ritter, and J. Peters, "Deep lagrangian networks: Using physics as model prior for deep learning," 2019.

[87] S. Ha and H. Jeong, "Discovering invariants via machine learning," *Phys. Rev. Res.*, vol. 3, p. L042035, Dec. 2021.

[88] P. Zhang, H. Shen, and H. Zhai, "Machine learning topological invariants with neural networks," *Phys. Rev. Lett.*, vol. 120, p. 066401, Feb. 2018.

[89] J. F. Rodriguez-Nieva and M. S. Scheurer, "Identifying topological order through unsupervised machine learning," *Nat. Phys.*, vol. 15, pp. 790–795, May 2019.

[90] S. Yu, X. Piao, and N. Park, "Machine learning identifies scale-free properties in disordered materials," *Nat. Commun.*, vol. 11, p. 4842, Sept. 2020.

[91] M. Raissi, A. Yazdani, and G. E. Karniadakis, "Hidden fluid mechanics: Learning velocity and pressure fields from flow visualizations," *Science*, vol. 367, pp. 1026–1030, Feb. 2020.

[92] W. Ma, Z. Liu, Z. A. Kudyshev, A. Boltasseva, W. Cai, and Y. Liu, "Deep learning for the design of photonic structures," *Nat. Photonics*, vol. 15, pp. 77–90, Oct. 2021.

[93] J. Jiang, M. Chen, and J. A. Fan, "Deep neural networks for the evaluation and design of photonic devices," *Nat. Rev. Mater.*, vol. 6, pp. 679–700, Dec. 2021.

[94] Y. Xu, X. Zhang, Y. Fu, and Y. Liu, "Interfacing photonics with artificial intelligence: an innovative design strategy for photonic structures and devices based on artificial neural networks," *Photonics Res.*, vol. 9, p. B135, Mar. 2021.

[95] P. R. Wiecha and O. L. Muskens, "Deep learning meets nanophotonics: A generalized accurate predictor for near fields and far fields of arbitrary 3d nanostructures," *Nano Lett.*, vol. 20, pp. 329–338, Dec. 2019.

[96] D. Liu, Y. Tan, E. Khoram, and Z. Yu, "Training deep neural networks for the inverse design of nanophotonic structures," *ACS Photonics*, vol. 5, pp. 1365–1369, Feb. 2018.

[97] W. Ma, F. Cheng, and Y. Liu, "Deep-learning-enabled on-demand design of chiral metamaterials," *ACS Nano*, vol. 12, pp. 6326–6334, June 2018.

[98] S. So, J. Mun, and J. Rho, "Simultaneous inverse design of materials and structures via deep learning: Demonstration of dipole resonance engineering using core–shell nanoparticles," *ACS Appl. Mater. Interfaces*, vol. 11, pp. 24264–24268, June 2019.

[99] W. Ma, F. Cheng, Y. Xu, Q. Wen, and Y. Liu, "Probabilistic representation and inverse design of metamaterials based on a deep generative model with semi-supervised learning strategy," *Adv. Mater.*, vol. 31, p. 1901111, July 2019.

[100] Z. Liu, D. Zhu, K.-T. Lee, A. S. Kim, L. Raju, and W. Cai, "Compounding meta-atoms into metamolecules with hybrid artificial intelligence techniques," *Adv. Mater.*, vol. 32, p. 1904790, Dec. 2020.

[101] W. Ma and Y. Liu, "A data-efficient self-supervised deep learning model for design and characterization of nanophotonic structures," *Sci. China Phys. Mech. Astron.*, vol. 63, June 2020.

[102] H. Ren, W. Shao, Y. Li, F. Salim, and M. Gu, "Three-dimensional vectorial holography based on machine learning inverse design," *Sci. Adv.*, vol. 6, p. eaaz4261, Apr. 2020.

[103] Z. Liu, D. Zhu, S. P. Rodrigues, K.-T. Lee, and W. Cai, "Generative model for the inverse design of metasurfaces," *Nano Lett.*, vol. 18, pp. 6570–6576, Sept. 2018.

[104] S. So and J. Rho, "Designing nanophotonic structures using conditional deep convolutional generative adversarial networks," *Nanophotonics*, vol. 8, pp. 1255–1261, June 2019.

[105] R. Unni, K. Yao, and Y. Zheng, "Deep convolutional mixture density network for inverse design of layered photonic structures," *ACS Photonics*, vol. 7, pp. 2703–2712, Sept. 2020.

[106] R. Unni, K. Yao, X. Han, M. Zhou, and Y. Zheng, "A mixture-density-based tandem optimization network for on-demand inverse design of thin-film high reflectors," *Nanophotonics*, vol. 10, pp. 4057–4065, Oct. 2021.

[107] J. Peurifoy, Y. Shen, L. Jing, Y. Yang, F. Cano-Renteria, B. G. DeLacy, J. D. Joannopoulos, M. Tegmark, and M. Soljačić, "Nanophotonic particle simulation and inverse design using artificial neural networks," *Sci. Adv.*, vol. 4, p. eaar4206, June 2018.

[108] C. Zhang, J. Jin, W. Na, Q.-J. Zhang, and M. Yu, "Multivalued neural network inverse modeling and applications to microwave filters," *IEEE Trans. Microw. Theory and Techn.*, vol. 66, no. 8, pp. 3781–3797, 2018.

[109] H. H. Sheinfux, I. Kaminer, A. Z. Genack, and M. Segev, "Interplay between evanescence and disorder in deep subwavelength photonic structures," *Nat. Commun.*, vol. 7, p. 12927, Oct. 2016.

[110] C. W. Hsu, B. Zhen, W. Qiu, O. Shapira, B. G. DeLacy, J. D. Joannopoulos, and M. Soljačić, "Transparent displays enabled by resonant nanoparticle scattering," *Nat. Commun.*, vol. 5, p. 3152, Jan. 2014.

[111] N. Aizawa, Y.-J. Pu, M. Watanabe, T. Chiba, K. Ideta, N. Toyota, M. Igarashi, Y. Suzuri, H. Sasabe, and J. Kido, "Solution-processed multilayer small-molecule light-emitting devices with high-efficiency white-light emission," *Nat. Commun.*, vol. 5, p. 5756, Dec. 2014.

[112] W. L. Chan, H.-T. Chen, A. J. Taylor, I. Brener, M. J. Cich, and D. M. Mittleman, "A spatial light modulator for terahertz beams," *Appl. Phys. Lett.*, vol. 94, p. 213511, May 2009.

[113] Y. LeCun, Y. Bengio, and G. Hinton, "Deep learning," *Nature*, vol. 521, pp. 436–444, May 2015.

[114] D. Lencer, M. Salinga, B. Grabowski, T. Hickel, J. Neugebauer, and M. Wuttig, "A map for phase-change materials," *Nat. Mater.*, vol. 7, pp. 972–977, Nov. 2008.

[115] M. F. Yanik, S. Fan, M. Soljačić, and J. D. Joannopoulos, "All-optical transistor action with bistable switching in a photonic crystal cross-waveguide geometry," *Opt. Lett.*, vol. 28, p. 2506, Dec. 2003.

[116] X. Piao, S. Yu, and N. Park, "Control of fano asymmetry in plasmon induced transparency and its application to plasmonic waveguide modulator," *Opt. Express*, vol. 20, p. 18994, Aug. 2012.

[117] A. Komar, R. Paniagua-Domínguez, A. Miroshnichenko, Y. F. Yu, Y. S. Kivshar, A. I. Kuznetsov, and D. Neshev, "Dynamic beam switching by liquid crystal tunable dielectric metasurfaces," *ACS Photonics*, vol. 5, pp. 1742–1748, Feb. 2018.

[118] A. M. Shaltout, V. M. Shalaev, and M. L. Brongersma, "Spatiotemporal light control with active metasurfaces," *Science*, vol. 364, May 2019.

[119] K. Chung, S. Yu, C.-J. Heo, J. W. Shim, S.-M. Yang, M. G. Han, H.-S. Lee, Y. Jin, S. Y. Lee, N. Park, and J. H. Shin, "Flexible, angle-independent, structural color reflectors inspired by morpho butterfly wings," *Adv. Mater.*, vol. 24, pp. 2375–2379, Apr. 2012.

[120] A.-L. Barabasi, *Network Science*. Cambridge, England: Cambridge University Press, July 2016.

[121] W. R. Bandy and A. J. Glick, "Tight-binding green's-function calculations of electron tunneling. ii. diagonal disorder in the one-dimensional two-band model," *Phys. Rev. B*, vol. 16, pp. 2346–2349, Sept. 1977.

[122] J. B. Pendry, "Off-diagonal disorder and 1d localisation," *J. Phys. C: Solid State Phys.*, vol. 15, pp. 5773–5778, Oct. 1982.

[123] H. Herzig Sheinfux, I. Kaminer, Y. Plotnik, G. Bartal, and M. Segev, "Sub-wavelength multilayer dielectrics: Ultrasensitive transmission and breakdown of effective-medium theory," *Phys. Rev. Lett.*, vol. 113, p. 243901, Dec. 2014.

[124] S. Havlin, R. B. Selinger, M. Schwartz, H. E. Stanley, and A. Bunde, "Random multiplicative processes and transport in structures with correlated spatial disorder," *Phys. Rev. Lett.*, vol. 61, pp. 1438–1441, Sept. 1988.

[125] F. A. B. F. de Moura and M. L. Lyra, "Delocalization in the 1d anderson model with long-range correlated disorder," *Phys. Rev. Lett.*, vol. 81, pp. 3735–3738, Oct. 1998.

[126] G. K. Shirmanesh, R. Sokhoyan, R. A. Pala, and H. A. Atwater, "Dual-gated active metasurface at 1550 nm with wide ($> 300°$) phase tunability," *Nano Lett.*, vol. 18, pp. 2957–2963, Mar. 2018.

[127] S. An, C. Fowler, B. Zheng, M. Y. Shalaginov, H. Tang, H. Li, L. Zhou, J. Ding, A. M. Agarwal, C. Rivero-Baleine, K. A. Richardson, T. Gu, J. Hu, and H. Zhang, "A deep learning approach for objective-driven all-dielectric metasurface design," *ACS Photonics*, vol. 6, pp. 3196–3207, Nov. 2019.

[128] J. Tian, H. Luo, Y. Yang, F. Ding, Y. Qu, D. Zhao, M. Qiu, and S. I. Bozhevolnyi, "Active control of anapole states by structuring the phase-change alloy $Ge_2Sb_2Te_5$," *Nat. Commun.*, vol. 10, p. 386, Jan. 2019.

[129] S. Abdollahramezani, O. Hemmatyar, M. Taghinejad, H. Taghinejad, Y. Kiarashinejad, M. Zandehshahvar, T. Fan, S. Deshmukh, A. A. Eftekhar, W. Cai, E. Pop, M. A. El-Sayed, and A. Adibi, "Dynamic hybrid metasurfaces," *Nano Lett.*, vol. 21, pp. 1238–1245, Jan. 2021.

[130] Y. Sharabi, E. Lustig, and M. Segev, "Disordered photonic time crystals," *Phys. Rev. Lett.*, vol. 126, p. 163902, Apr. 2021.

[131] S. Longhi, "Quantum-optical analogies using photonic structures," *Laser Photonics Rev.*, vol. 3, no. 3, pp. 243–261, 2009.

[132] L. Feng, R. El-Ganainy, and L. Ge, "Non-hermitian photonics based on parity-time symmetry," *Nat. Photonics*, vol. 11, no. 12, pp. 752–762, 2017.

[133] L. Lu, J. D. Joannopoulos, and M. Soljačić, "Topological photonics," *Nat. Photonics*, vol. 8, no. 11, pp. 821–829, 2014.

[134] T. Ozawa, H. M. Price, A. Amo, N. Goldman, M. Hafezi, L. Lu, M. C. Rechtsman, D. Schuster, J. Simon, O. Zilberberg, and I. Carusotto, "Topological photonics," *Rev. Mod. Phys.*, vol. 91, no. 1, p. 015006, 2019.

[135] M.-A. Miri, M. Heinrich, R. El-Ganainy, and D. N. Christodoulides, "Supersymmetric optical structures," *Phys. Rev. Lett.*, vol. 110, no. 23, p. 233902, 2013.

[136] S. Yu, X. Piao, J. Hong, and N. Park, "Bloch-like waves in random-walk potentials based on supersymmetry," *Nat. Commun.*, vol. 6, p. 8269, Sept. 2015.

[137] J. Carolan, C. Harrold, C. Sparrow, E. Martin-Lopez, N. J. Russell, J. W. Silverstone, P. J. Shadbolt, N. Matsuda, M. Oguma, M. Itoh, G. D. Marshall, M. G. Thompson, J. C. F. Matthews, T. Hashimoto, J. L. O'Brien, and A. Laing, "Universal linear optics," *Science*, vol. 349, no. 6249, pp. 711–716, 2015.

[138] N. Engheta, "Metamaterials with high degrees of freedom: space, time, and more," *Nanophotonics*, vol. 10, no. 1, pp. 639–642, 2021.

[139] W. Nie, "Optical nonlinearity - phenomena, applications, and materials," *Adv. Mater.*, vol. 5, no. 7-8, pp. 520–545, 1993.

[140] J. Leuthol, C. Koos, and W. Freude, "Nonlinear silicon photonics," *Nat. Photonics*, vol. 4, no. 8, pp. 535–544, 2010.

[141] M. Spagnolo, J. Morris, S. Piacentini, M. Antesberger, F. Massa, A. Crespi, F. Ceccarelli, R. Osellame, and P. Walther, "Experimental photonic quantum memristor," *Nat. Photonics*, vol. 16, no. 4, pp. 318–+, 2022.

[142] J. R. Zurita-Sánchez, P. Halevi, and J. C. Cervantes-González, "Reflection and transmission of a wave incident on a slab with a time-periodic dielectric function $\epsilon(t)$," *Phys. Rev. A*, vol. 79, May 2009.

[143] E. Lustig, Y. Sharabi, and M. Segev, "Topological aspects of photonic time crystals," *Optica*, vol. 5, no. 11, pp. 1390–1395, 2018.

[144] R. Carminati, H. Chen, R. Pierrat, and B. Shapiro, "Universal statistics of waves in a random time-varying medium," *Phys. Rev. Lett.*, vol. 127, no. 9, p. 094101, 2021.

[145] J. Park, H. Cho, S. Lee, K. Lee, K. Lee, H. C. Park, J.-W. Ryu, N. Park, S. Jeon, and B. Min, "Revealing non-hermitian band structure of photonic floquet media," *Sci. Adv.*, vol. 8, p. eabo6220, Oct. 2022.

[146] M. Lyubarov, Y. Lumer, A. Dikopoltsev, E. Lustig, Y. Sharabi, and M. Segev, "Amplified emission and lasing in photonic time crystals," *Science*, vol. 377, pp. 425–428, 2022.

[147] V. Pacheco-Peña and N. Engheta, "Effective medium concept in temporal meta-materials," *Nanophotonics*, vol. 9, no. 2, pp. 379–391, 2020.

[148] K. Lee, J. Park, S. Lee, S. Baek, J. Park, F. Rotermund, and B. Min, "Resonance-enhanced spectral funneling in fabry-perot resonators with a temporal boundary mirror," *Nanophotonics*, vol. 11, no. 9, pp. 2045–2055, 2022.

[149] C. García-Meca, A. M. Ortiz, and R. L. Sáez, "Supersymmetry in the time domain and its applications in optics," *Nat. Commun,*, vol. 11, no. 1, p. 813, 2020.

[150] H. Li, S. Yin, E. Galiffi, and A. Alù, "Temporal parity-time symmetry for extreme energy transformations," *Phys. Rev. Lett.*, vol. 127, no. 15, 2021.

[151] H. Li, S. Yin, and A. Alù, "Nonreciprocity and faraday rotation at time interfaces," *Phys. Rev. Lett.*, vol. 128, p. 173901, 2022.

[152] J. M. Lukens, D. E. Leaird, and A. M. Weiner, "A temporal cloak at telecommunication data rate," *Nature*, vol. 498, no. 7453, pp. 205–208, 2013.

[153] V. Pacheco-Peña and N. Engheta, "Temporal aiming," *Light Sci. Appl.*, vol. 9, no. 1, p. 129, 2020.

[154] V. Pacheco-Peña and N. Engheta, "Antireflection temporal coatings," *Optica*, vol. 7, no. 4, pp. 323–331, 2020.

[155] G. Castaldi, V. Pacheco-Peña, M. Moccia, N. Engheta, and V. Galdi, "Exploiting space-time duality in the synthesis of impedance transformers via temporal metamaterials," *Nanophotonics*, vol. 10, no. 14, pp. 3687–3699, 2021.

[156] J. Park and B. Min, "Spatiotemporal plane wave expansion method for arbitrary space-time periodic photonic media," *Opt. Lett.*, vol. 46, no. 3, pp. 484–487, 2021.

[157] V. Twersky, "Multiple scattering of waves and optical phenomena*," *J. Opt. Soc. Am.*, vol. 52, p. 145, Feb. 1962.

[158] M. E. Peskin and D. V. Schroeder, *An introduction to quantum field theory*. Philadelphia, PA: Westview Press, Sept. 1995.

[159] S. Torquato, *Random heterogeneous materials*. Interdisciplinary Applied Mathematics, New York, NY: Springer, 1 ed., Oct. 2005.

[160] S. Torquato and F. H. Stillinger, "Local density fluctuations, hyperuniformity, and order metrics," *Phys. Rev. E*, vol. 68, p. 041113, Oct. 2003.

[161] S. Torquato, G. Zhang, and F. Stillinger, "Ensemble theory for stealthy hyper-uniform disordered ground states," *Phys. Rev. X*, vol. 5, no. 2, p. 021020, 2015.

[162] R. D. Batten, F. H. Stillinger, and S. Torquato, "Classical disordered ground states: Super-ideal gases and stealth and equi-luminous materials," *J. Appl. Phys.*, vol. 104, p. 033504, Aug. 2008.

[163] M. Florescu, S. Torquato, and P. J. Steinhardt, "Designer disordered materials with large, complete photonic band gaps," *Proc. Natl. Acad. Sci. U.S.A.*, vol. 106, pp. 20658–20663, Dec. 2009.

[164] M. Florescu, P. J. Steinhardt, and S. Torquato, "Optical cavities and waveguides in hyperuniform disordered photonic solids," *Phys. Rev. B*, vol. 87, p. 165116, Apr. 2013.

[165] R. Garcia-Millan, G. Pruessner, L. Pickering, and K. Christensen, "Correlations and hyperuniformity in the avalanche size of the oslo model," *EPL*, vol. 122, p. 50003, July 2018.

[166] A. Yariv and P. Yeh, *Optical waves in crystals*. Wiley Series in Pure and Applied Optics, Nashville, TN: John Wiley & Sons, Nov. 2002.

[167] H. A. Macleod, *Thin-film optical filters*. Series in optics and optoelectronics, Boca Raton, FL: CRC Press/Taylor & Francis, 4th ed., 2010.

[168] K. J. Vahala, "Optical microcavities," *Nature*, vol. 424, no. 6950, pp. 839–846, 2003.

[169] M. S. Green, "Markoff random processes and the statistical mechanics of time-dependent phenomena," *J. Chem. Phys.*, vol. 20, no. 8, pp. 1281–1295, 1952.

[170] R. Kubo, "Statistical-mechanical theory of irreversible processes .1. general theory and simple applications to magnetic and conduction problems," *J. Phys. Soc. Jpn.*, vol. 12, no. 6, pp. 570–586, 1957.

[171] D. Alfè and M. J. Gillan, "First-principles calculation of transport coefficients," *Phys. Rev. Lett.*, vol. 81, no. 23, pp. 5161–5164, 1998.

[172] C. Carbogno, R. Ramprasad, and M. Scheffler, "Ab initio green-kubo approach for the thermal conductivity of solids," *Phys. Rev. Lett.*, vol. 118, no. 17, p. 175901, 2017.

[173] K. A. Lurie and V. V. Yakovlev, "Energy accumulation in waves propagating in space- and time-varying transmission lines," *IEEE Antennas Wirel. Propag. Lett.*, vol. 15, pp. 1681–1684, 2016.

[174] S. Taravati, N. Chamanara, and C. Caloz, "Nonreciprocal electromagnetic scattering from a periodically space-time modulated slab and application to a quasisonic isolator," *Phys. Rev. B*, vol. 96, no. 16, p. 165144, 2017.

[175] A. Shlivinski and Y. Hadad, "Beyond the bode-fano bound: Wideband impedance matching for short pulses using temporal switching of transmission-line parameters," *Phys. Rev. Lett.*, vol. 121, no. 20, p. 204301, 2018.

[176] Y. Hadad and A. Shlivinski, "Soft temporal switching of transmission line parameters: Wave-field, energy balance, and applications," *IEEE Trans. Antennas Propag.*, vol. 68, no. 3, pp. 1643–1654, 2020.

[177] Z. Hayran, J. B. Khurgin, and F. Monticone, "$\hbar\omega$ versus $\hbar k$: dispersion and energy constraints on time-varying photonic materials and time crystals [invited]," *Opt. Mater. Express*, vol. 12, p. 3904, Sept. 2022.

[178] J. Kuttruff, D. Garoli, J. Allerbeck, R. Krahne, A. D. Luca, D. Brida, V. Caligiuri, and N. Maccaferri, "Ultrafast all-optical switching enabled by epsilon-near-zero-tailored absorption in metal-insulator nanocavities," *Commun. Phys.*, vol. 3, June 2020.

[179] M. Taghinejad, H. Taghinejad, Z. Xu, Y. Liu, S. P. Rodrigues, K.-T. Lee, T. Lian, A. Adibi, and W. Cai, "Hot-electron-assisted femtosecond all-optical modulation in plasmonics," *Adv. Mater.*, vol. 30, p. 1704915, Jan. 2018.

[180] J. Bohn, T. S. Luk, C. Tollerton, S. W. Hutchings, I. Brener, S. Horsley, W. L. Barnes, and E. Hendry, "All-optical switching of an epsilon-near-zero plasmon resonance in indium tin oxide," *Nat. Commun.*, vol. 12, p. 1017, Feb. 2021.

[181] Z. Yu and S. Fan, "Complete optical isolation created by indirect interband photonic transitions," *Nat. Photonics*, vol. 3, pp. 91–94, Jan. 2009.

[182] D. Jalas, A. Petrov, M. Eich, W. Freude, S. Fan, Z. Yu, R. Baets, M. Popović, A. Melloni, J. D. Joannopoulos, M. Vanwolleghem, C. R. Doerr, and H. Renner, "What is — and what is not — an optical isolator," *Nat. Photonics*, vol. 7, pp. 579–582, July 2013.

[183] S. Ioffe and C. Szegedy, "Batch normalization: Accelerating deep network training by reducing internal covariate shift," in *Proceedings of the 32nd International Conference on Machine Learning* (F. Bach and D. Blei, eds.), vol. 37 of *Proceedings of Machine Learning Research*, (Lille, France), pp. 448–456, PMLR, 07–09 Jul 2015.

[184] D. Hendrycks and K. Gimpel, "Gaussian error linear units (GELUs)," 2016.

[185] Y. Liu, J. Li, S. Sun, and B. Yu, "Advances in gaussian random field generation: a review," *Comput. Geosci.*, vol. 23, pp. 1011–1047, Aug. 2019.

[186] M. Davanço, Y. Urzhumov, and G. Shvets, "The complex bloch bands of a 2d plasmonic crystal displaying isotropic negative refraction," *Opt. Express*, vol. 15, pp. 9681–9691, July 2007.

초 록

광스위칭 (photonic switching) 소자는 일반 전자소자 기반 컴퓨터 내부 트랜지스터 의 동작 원리와 같이, 외부의 변조에 따라 광 응답 (optical response)을 조절할 수 있는 소자로서 광 기억소자 및 광 신호처리 장치의 기본이 된다. 이러한 스위칭 소자를 설계함에 있어, 소자의 동작과 관련된 공간 및 시간적인 복잡도는 매우 중요한 요인이다. 예를 들어, 스핀 및 궤도 각운동량, 파수벡터 등 빛의 공간적인 특성과 함께, 동작 주파수 및 대역, 에너지 보존 등 빛의 시간적인 특성은 관련된 매질 또는 구조의 특성과 연결하여 고려되어야 한다. 이러한 관점에서, 스위칭 소자를 설계할 때는 그 기능적 다양성 및 복잡성으로부터 기인하는 높은 설계 자유도가 요구되지만, 일반적으로 소자의 구조가 가지는 물리적인 대칭성으로부터 그러한 자유도에 통합적으로 접근하는 것은 극히 제한된다. 따라서, 대칭성이 주는 해석의 용이성 및 간결함, 적은 계산 비용에도 불구하고, 의도적인 대칭성 파괴를 통해 폭넓은 시공간적 자유도에 접근하는 것은 최근 연구의 트렌드가 되고 있다.

따라서, 이 논문에서는 스위칭 소자를 설계함에 있어 시공간적 복잡도를 해결하기 위한 수치적, 이론적, 및 데이터 기반의 여러 관련된 방법론들을 소개한다. 특히, 광결정에서의 C_{4v}-대칭성 및 거울 대칭성 붕괴에 기반한 기울어진 디락 (Dirac) 분산관계 및 갭 분리, 시공간적 무질서계에서의 병진 대칭성을 파괴에 의한 빛의 산란특성 제어에 대해 이론적 배경과 함께 심도있게 다루도록 한다.